Review

AIE-featured tetraphenylethylene nanoarchitectures in biomedical application: Bioimaging, drug delivery and disease treatment

Kothanahally S. Sharath Kumar [a,1,*], Yarabahally R. Girish [b,1], Milad Ashrafizadeh [c,d,1], Sepideh Mirzaei [e], Kadalipura P. Rakesh [f], Mohammad Hossein Gholami [g], Amirhossein Zabolian [h], Kiavash Hushmandi [i], Gorka Orive [j,k,l,m,*], Firoz Babu Kadumudi [n], Alireza Dolatshahi-Pirouz [o], Vijay Kumar Thakur [p,q], Ali Zarrabi [d], Pooyan Makvandi [r], Kanchugarakoppal S. Rangappa [s,*]

[a] Department of Studies in Chemistry, Manasagangotri, University of Mysore, Mysuru 570006 India
[b] Centre for Research and Innovations, School of Natural Sciences, BGSIT, Adichunchanagiri University, B. G. Nagara, Mandya 571448, India
[c] Faculty of Engineering and Natural Sciences, Sabanci University, Orta Mahalle, Üniversite Caddesi No. 27, Orhanlı, Tuzla, 34956 Istanbul, Turkey
[d] Sabanci University Nanotechnology Research and Application Center (SUNUM), Tuzla, 34956 Istanbul, Turkey
[e] Department of Biology, Faculty of Science, Islamic Azad University, Science and Research Branch, Tehran, Iran
[f] School of Material Science and Engineering, Gwangju Institute of Science and Technology, Gwangju 61005, Republic of Korea
[g] Faculty of Veterinary Medicine, Kazerun Branch, Islamic Azad University, Kazerun, Iran
[h] Young Researchers and Elite Club, Tehran Medical Sciences, Islamic Azad University, Tehran, Iran
[i] Department of Food Hygiene and Quality Control, Division of Epidemiology, Faculty of Veterinary Medicine, University of Tehran, Tehran, Iran
[j] NanoBioCel Research Group, School of Pharmacy, University of the Basque Country (UPV/EHU), Vitoria-Gasteiz, Spain
[k] University Institute for Regenerative Medicine and Oral Implantology - UIRMI (UPV/EHU-Fundación Eduardo Anitua), Vitoria-Gasteiz, Spain
[l] Bioaraba, NanoBioCel Research Group, Vitoria-Gasteiz, Spain
[m] Singapore Eye Research Institute, The Academia, 20 College Road, Discovery Tower, Singapore
[n] Department of Health Technology, Technical University of Denmark, 2800 Kgs. Lyngby, Denmark
[o] Department of Health Technology, Technical University of Denmark, Center for Intestinal Absorption and Transport of Biopharmaceuticals, 2800 Kgs. Lyngby, Denmark
[p] Biorefining and Advanced Materials Research Center, Scotland's Rural College (SRUC), Kings Buildings, Edinburgh EH9 3JG, UK
[q] Department of Mechanical Engineering, School of Engineering, Shiv Nadar University, Uttar Pradesh 201314, India
[r] Istituto Italiano di Tecnologia, Centre for Materials Interfaces, Viale Rinaldo Piaggio 34, 56025 Pontedera, Pisa, Italy
[s] Institution of Excellence, Vijnana Bhavan, University of Mysore, Manasagangotri, Mysuru 570006, India

ARTICLE INFO

ABSTRACT

The development of aggregation-induced emission (AIE) has received extreme considerations from basic and clinical researches. To date, various luminogens with AIE property (AIEgens) have been broadly utilized in optoelectronic devices, fluorescent bio-probes, drug delivery, anticancer and chemosensors and many more. Scientists have likewise dedicated to investigating the possibilities of AIEgens in the biomedical field. Among the various AIE luminophores studied, tetraphenylethylene (TPE) derivatives have demonstrated as most promising AIEgen, owing to their capacity in self-organization and conjugation with aggregation-caused quenching (ACQ) fluorophores to form larger multi-component assemblies.

Abbreviations: ACQ, aggregation-caused quenching; AIE, aggregation-induced emission; TPE, tetraphenylethene; AIEE, AIE enhancement; OLEDs, organic light-emitting diodes; PDT, photodynamic therapy; ALP, alkaline phosphatase; GSH, glutathione; COF, covalent organic framework; HOF, hydrogen-bonded organic framework; MOF, metal organic framework; Cys, cysteine; Hcy, homocysteine; Gal, D,galactose; LAP, leucine aminopeptidase; PNPs, polymeric nanoparticles; ROMP, ring opening metatheses polymerization; DEDA, N-,N-diethylehtlenediamine; SDS, sodium dodecyl sulfonate; ROS, reactive oxygen species; ICT, intramolecular charge transfer; DCM, dichloromethane; OPEF, one-photon excited fluorescence; TREF, two-photon excited fluorescence; Ser, serine; Asp, aspartic acid; PTPA, poly(N,N-diphenyl 1-4-(4-(1,2,2-triphenylvinyl)styryl)aniline); MHNS, mesoporous silica hollow nanospheres; anti-EpCAM, anti-epithelial cellular adhesion molecule; GTMS, γ-glycidoxypropyltrimethox ysilane; PTZ, phenothiazine; TICT, twisted intramolecular charge transfer; MDR, multidrug resistant; AMO, amoxicillin; EDA, 1,2-ethane diamine; PGEDA, polyglycerol methacrylate; LTA, lipoteichoic acid; PSs, photosensitizers; NIR, near-infrared; DC, dicyanovinyl; FR, far red; DCFDA, dichlorofluorescenceindiaacetate; Cbl, chlorambucil; PDI, photodynamic inactivation; EPR, enhanced permeability and retention; MMC, mitomycin C; BSO, buthionine sulfoximine; PTX, paclitaxel; PEG, polyethylene glycol; DA, dimethylmaleic anhydride; GO, gene ontology; KEGC, Kyoto encyclopaedia of genes and genomics.

* Corresponding authors at: Department of Studies in Chemistry, Manasagangotri, University of Mysore, Mysuru, India (K. S. Sharath Kumar). NanoBioCel Research Group, School of Pharmacy, University of the Basque Country (UPV/EHU), Vitoria-Gasteiz, Spain (Gorka Orive). Institution of Excellence, Vijnana Bhavan, University of Mysore, Manasagangotri, Mysuru, India (K. S. Rangappa).

E-mail addresses: sharathrsh@chemistry.uni-mysore.ac.in (K.S. Sharath Kumar), gorka.orive@ehu.eus (G. Orive), rangappaks@ioe.uni-mysore.ac.in (K.S. Rangappa).
[1] Contributed equally.

AIE
Luminogens
Biomedical applications

It likewise generally utilized in different fields, like organic and therapeutic science, supramolecular chemistry, organic electronics, cancer therapy, apoptosis and inflammation, microorganism imaging therapy etc. This review encompasses the recent advances of TPE based AIE-active luminophores and their potential applications in biomolecular science.

Contents

1. Introduction

During the past few decades organic materials that emit fluorescence in the condensed and solid-state is of great attention in various fields such as in chemo-/bio-sensors, detection of cancer cells, bio-imaging, drug delivery etc [1–5], due to their high photostability and excellent fluorescent quantum yields [6,7]. Despite of the development of these luminescent materials, an infamous phenomenon emerges called aggregation-caused quenching (ACQ), which potentially restricts many applications including optoelectronics and biology [8]. ACQ is a phenomenon wherein the emission of fluorophores in solid-state or in suspension is quenched because of aggregate formation. This can be attributed to that most of the organic luminogens have rigid and planar molecular structures and strong affinity of intermolecular π-π stacking interactions in the condensed form. Thus, these luminogens follow a non-radiative relaxation pathway, resulting in emission annihilation.

Tang et al. [12] first time found a phenomenon exactly opposite to that of ACQ photophysical properties based on propeller-shaped silole organic moiety, and was named as aggregation-induced emission (AIE). After that, AIE material has become a hot topic of anti-ACQ materials where the non-luminescent materials in the molecularly solutions are made to emit strong fluorescence when it is in the condensed state or in the aggregated state [13]. The AIE mechanism is demonstrated in Fig. 1, the mechanism of AIE is amalgamated as the restriction of intramolecular rotations (RIR) in the aggregations due to various intermolecular interactions, which help to design AIE luminogen of high luminescence.

Park et al [14] further discovered one more concept named aggregation-induced emission enhancement (AIEE), where luminogens exhibit emission both in solution and solid, as well as in the aggregated state. To understand the mechanistic pathway, various research groups have proposed different mechanisms including conformational planarization, excited intermolecular proton transfer, twisted intermolecular charge transformation, and E/Z isomerization [15,16]. However, all these mechanisms were not supported by experimental evidence. Tang et al [17] in 2014 have attributed the AIE effect to the RIR of molecules effect upon aggregation due to intermolecular interactions between the AIE molecules. Further, this phenomenon is most important to address ACQ problems, as AIE luminogens show the highest fluorescence intensity, better photostability, turn on fluorescence, and larger stroke shift as illustrated in (Fig. 2) encouraging researchers to develop and to construct solid state emitters in practical applications in organic light-emitting diodes [18] and chemo/biosensors [19] for biological imaging and monitoring of biological processes.

In recent times, there are large numbers of luminogens in the literature with AIE/AIEE characteristics. These include TPE, siloles, napthalimide, anthracene derivatives, carbazoles, cyanostilbenes, phenothiazines, boron-dipyrromethene derivatives (BODIPY), diphenyldibenzofulvenes, organoboron, pyrene derivatives, pyrazine derivatives, metal complexes, etc [13,20–24]. TPE is considered as a promising building block for forming macrocycles and cages [25], and it is the most extensively studied AIEgen because of self-organisation capability and their compatibility with ACQ fluorophores [26]. Moreover, TPE derivatives have benefited as
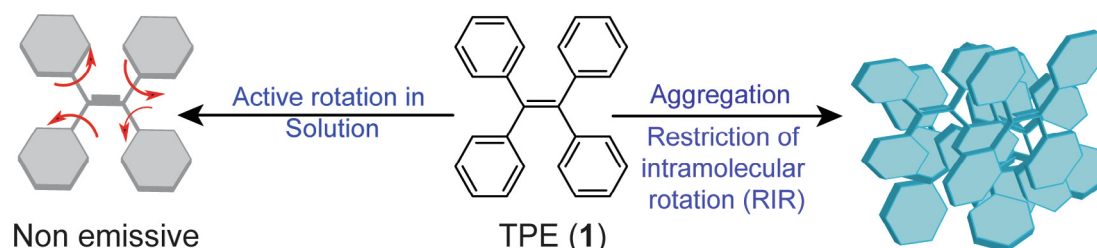

Fig. 1. Representing AIE phenomenon of propeller-shaped TPE luminogen in solution and aggregated state [9–11].
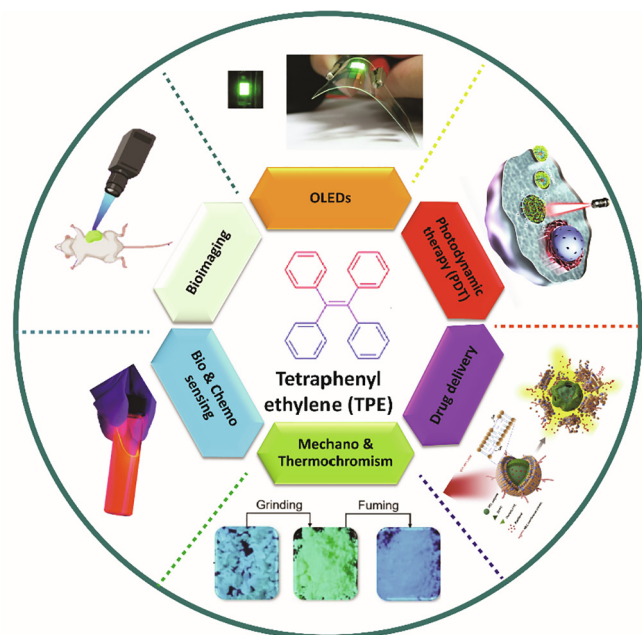
Fig. 2. Possible applications of AIE active TPE derivatives.

mechanoluminescent properties, where it can emit photons resulting from the mechanical stimuli excitation. The molecular structure of TPE is non-planar and possesses highly dynamic groups. TPE luminophores are non-emissive in solutions due to free rotation of the four phenyl rings around doubly bonded carbon atoms in the TPE molecule, causing a non-radiative relaxation process. The propeller-shaped conformation of TPE molecule restricts the

intramolecular rotation of the benzene rings upon aggregation. This shaped restriction of intramolecular rotation [27] results in prevention of non-radiative relaxation pathway and therefore TPE emits high fluorescence (Fig. 1).

To date, there have been several TPE derivatives in the literature with high fluorescence quantum yield with aid of functionalizing TPE with pyrene, anthracene, carbazole, triphenylamine, perylene, organoboron, BODIPY luminogens and used in various fields with potential applications (Fig. 2) [28–36]. Because of ease functionalization, TPE can be synthesized by various synthetic routes and are summarized in Scheme 1 [37–45]. TPE luminogens and its derivatives have been used in various applications such as mechanofluorochromic materials [46], OLEDs [47], chiral applications [48], solar cells [49], bio probes [50], biosensors [51], cell imaging [52] and drug delivery.[53]

Many efforts have been made to summarize the developments and applications of AIEgens. More recently, Xiaolei Cai and Bin Liu [54] reviewed recent advances in materials and biomedical applications of AIEgen focusing on design strategies and seldom discussed the biomedical applications. In this review, we offer a systematic summary on the fundamentals of TPE-based AIE luminogens and in-depth analysis of its applications in biomedicine. Our focus was put on the recent advances of the TPE-based probes for sensing biomolecules (alkaline phosphatase, ATP, cysteine, β-galactosidase, leucine aminopeptides, lipase etc.), ions detection (Cu^{2+}, Fe^{3+}, Hg^{2+}, Ag^{2+}, Zn^{2+} etc), bio imaging (at the cellular level), detection and inhibition of drug resistant bacteria (MRSA), cancer diagnosis (in cell lines and animal models), chemo-photodynamic therapy and imaging-guided drug delivery. In each of these sections, we brief the synthetic route of the probe, action of mechanism and its advantages. Lastly, we covered the perspective based on the understanding of overall developments, exploring the limitations and the more possible biomedical applications of TPE AIEgens.
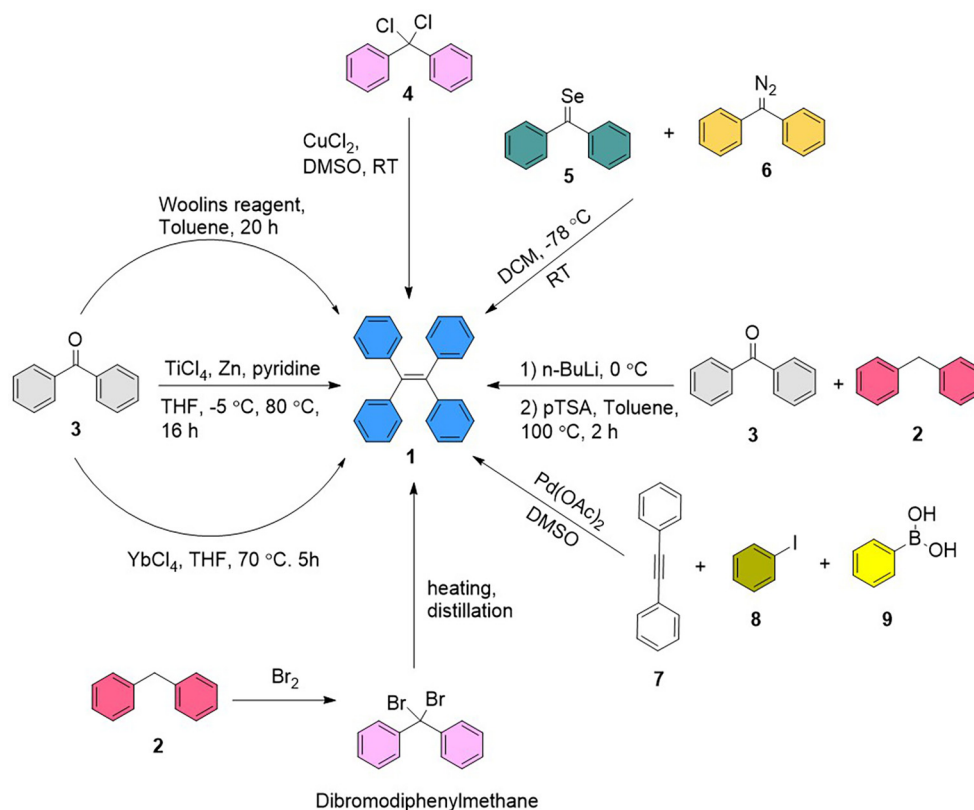
Scheme 1. Synthetic route of tetraphenylethylene (TPE **1**).

2. TPE based AIE probes for biosensing

Fluorescent sensing of biomolecules has attracted considerable attention for diagnosing several diseases including Alzheimer's disease, liver disfunction, osteoblastic bone cancer, prostate cancer, breast cancer and diabetes [55–60]. TPE-based fluorescent molecules with AIE characteristics have been recently developed as a potential method for sensing biomolecules like alkaline phosphatase (ALP), cholera toxin, glutathione (GSH), β-galactosidase, lipase and many more [61–65].

ALP is a protein enzyme and plays an important role in catalysing biochemical processes including dephosphorylation of phosphate ester, DNA, and proteins as well as in regulating cellular events of the cell cycle, growth, apoptosis, and signal transduction pathways [66,67]. So far, various methods are available for detection of ALP such as colorimetry, electrochemiluminescence, fluorometry, surface-enhanced Raman scattering, and chromatography etc [68–72]. TPE-based probe for biosensing has gained considerable attention for detection of ALP due to its high sensitivity and specificity. Wei Liu et al [61] have shown that AIE-active TPE based turn-on probes are effective for selective biosensing of ALP and pyrophosphate (PPi). Here, with diethylenetriamine-functionalized tetraphenylethylene probe **10** reaction with PPi creates an intermolecular self-assembly via hydrogen bonding between NH_2 groups of **10** and oxygen atoms of PPi and turn-on aggregation induced emission. Further introduction of ALP leads to hydrolysis of PPi to orthophosphate (Pi) turned off the fluorescence emission. This was the first example to use PPi-triggered AIE phenomenon for the ALP analysis and the detection limit was 0.09 mU mL^{-1} and 66.7 nM for ALP and PPi, respectively (Fig. 3).

Ai-Xiang Ding and colleagues [73] reported high selective and sensitive fluorescence probe to detect Cu^{2+} and ATP in water medium using a TPE amphiphile (**11**) which can generate AIE micelles in an aqueous solution (Fig. 4). A significant fluorescence quenching results from **11** and Cu^{2+} interaction, however fluorescence capacity can be immediately restored after addition of ATP from the in situ generated **11**-Cu^{2+} complex. The AIE active amphiphilic probe as hydrochloride **11** was analysed in THF/water mixture and the formation of micelles was identified by TEM. Both **11** and **11**-Cu^{2+} complexes were able to effectively image the Cu^{2+} and ATP in living HepG2 cells due to their sensitive fluorescence response towards analyte and showed high biocompatibility. These AIE micelles showed superior activity as interfacial chemosensor and sensing specific analyte and could become a new way for the development of an artificial sensor.

Intercellular thiols like GSH, homocysteine (Hcy) and cysteine (Cys) play a crucial part in the biochemical process [74,75]. Deficiency of cystine in humans leads to several health problems including depigmentation of hair, slowed growth in children, edema, liver damage, fat and weakness [76–78]. Various available analytical methods including HPLC, UV–vis and fluorescence spectroscopy for detection of Cys suffer from one or the other disadvantages [79–82]. Therefore, there is a need for a fluorescent probe that could selectively detect Cys in high sensitivity and selectivity because of its biological importance. Guoyu Jiang et al [63] designed and synthesized 2,4-dinitrobenzenesulfonyl functionalized TPE derivative **12** for biosensing Cys in PBS over Hcy and GSH with high specificity (Fig. 5). Synthesized probe **12** exhibited a weak emission in PBS buffer, whereas upon addition of Cys, the probe came in contact with the thiol group of Cys, which promoted cleavage of the 2,4-dinitrobenzenesulfonyl group in **12**, leading to the generation of fluorescence in **13**. The authors further carried out nucleophilic substitution reaction with other biologically important amino acids including Hcy and GSH, unfortunately they
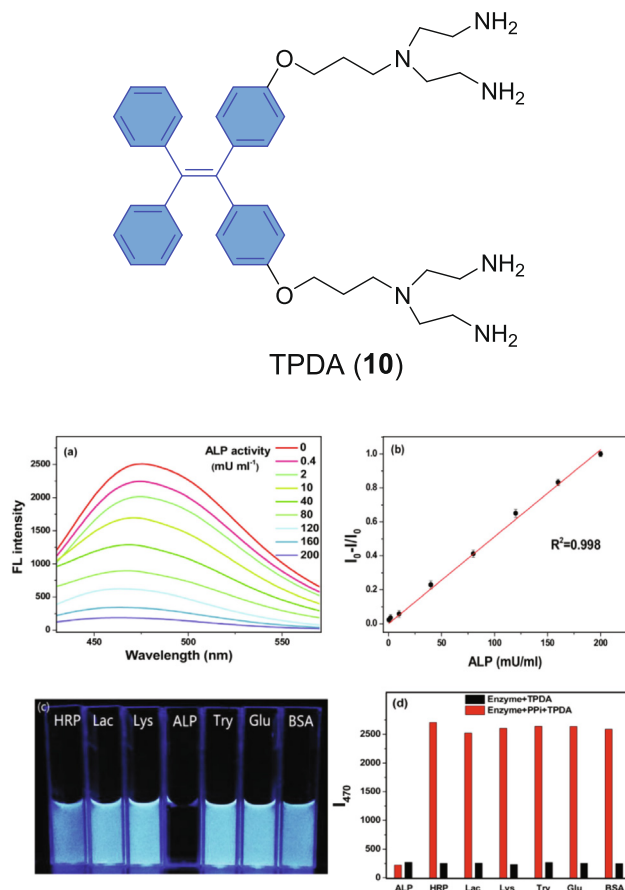

Fig. 3. Structure of **10**. (a) FL emission spectra of **10**-PPi complex (20 M) in Tris-HCl (pH 7.4) incubated with different ALP concentrations at 37 °C; (b) linear relationship of the FL intensity with ALP concentrations at 470 nm; (c) FL emission under a 365 nm lamp; (d) FL intensity of **10**-PPi complex (20 M) with various enzymes (50 mU mL^{-1}) in Tris-HCl (pH 7.4). Reproduced with permission from [61]. Copyright 2018 Elsevier.

didn't find any fluoresce enhancement. All these results suggest that 2,4-dinitrobenzenesulfonyl functionalized TPE derivative **12** is highly selective and sensitive probe for biosensing Cys over Hcy and GSH.

In 2017, Guoyu Jiang et al [64] reported that partially water soluble TPE derivative by conjugation of positively charged pyridinium pendant with D-galactose (Gal) **14** as fluorescent probe can be used for light-up imaging sensor of endogenous β-galactosidase detection in live cells (Fig. 6). β-galactosidase is an enzyme catalysing the hydrolysis of β-galactosides into monosaccharides by disrupting glycosidic linkage and its deficiency result in Morquio B syndrome. TPE-Gal (**14**) separated the β-galactopyranoside sugar moiety in the presence of an enzyme β-galactosidase resulting an intermediate phenolate to generate pyridine-substituted TPE **15** by elimination of *p*-quinone-methide. The formed derivative **15** is poorly soluble in water due to generation of aggregates and results in turn on fluorescence. This TPE-Gal (**14**) has unique features than traditional ACQ probes including high specificity, low toxicity toward β-galactosidase, and high cell permeability making them to find potential applications in cancer diagnosis.

Leucine aminopeptidase (LAP), which is a vital *exo*-pepetidase can hydrolyse *N*-terminal proteins in plants and animals. LAP has served as a biomarker for liver and pancreas related diseases. Recently, Shuailing Huang and co-workers [83] reported and synthesized TPE substituted DPA-TPE-Leu (**16**) derivative used for
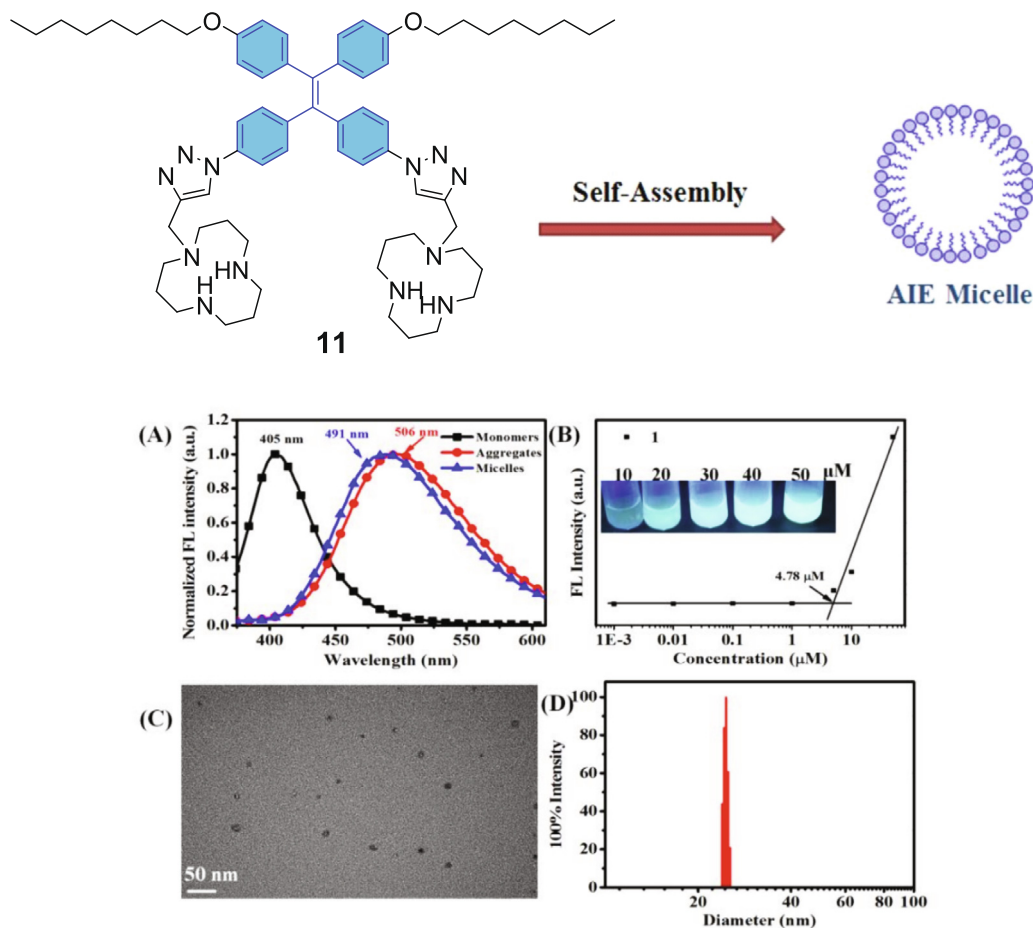
Fig. 4. Structure of **11**. (A) Fluorescence spectra of 11 in THF (monomers), aqueous solutions (micelles) and hydrochloride in THF (aggregates); (B) Plot of 491 nm versus concentration (inset displays photographs of 11 under 365 nm UV light illumination); (C, D) TEM image and size distribution of **11** in water. Reproduced with permission from [73]. Copyright 2018 Elsevier.

identifying LAP (Fig. 7). The L-leucine amide group of TPE derivative **16** is hydrophilic and undergoes cleavage by LAP, leading to the formation of hydrophobic aggregate DPE-TPE-OH (**17**). The study found that endogenous LAP has excellent photostability, low toxicity, good solubility with a detection limit of 0.16 UL^{-1}. Further, this endogenous LAP could be utilized for live-cell imaging of HepG2 xenograft tumour.

Lipase is a glycoprotein that its level in serum serves as an imperative biomarker for diagnosis of the acute pancreatitis and the disorders of pancreas. Hence, the development of probe for sensing lipase is crucial in the detection of pancreatic diseases. Recently Shi and co-worker [84] developed a fluorescent probe based on glutamate functionalized TPE **18** with turn-on AIE-activity for detection of lipase (Fig. 8). The as-synthesized glutamate functionalized TPE derivative **18** contains amino and carboxylic moieties as hydrophilic groups and in the presence of lipase, it facilitates the hydrolysis of glutamate group of TPE (**18**) at the oil–water interface resulting in aggregation of TPE-2OH derivative **19** which gives strong blue emission. Such a probe is appropriate for the lipase level up to 80 UL^{-1} in humans and lowest detection limit found as 0.13 UL^{-1}. Therefore, this probe is found to be a benefit for conducting the pathological analysis of disease involving the lipase enzyme.

Spermine is a natural polyamine biosynthesized by enzymatic decarboxylation of amino acids and exerts crucial role in cell growth and proliferation. Notably, enhanced levels of spermine are considered as risk factors for malignant tumor development. The lack of efficient probes for selective identification of spermine provoked Guoyu jiang and coworkers [85] to construct a supramolecular structure probe *via* electrostatic interactions between cationic and amphiphilic TPE AIEgen and cucurbit[7]uril (CB7) for biodetection of spermine over spermidine. Free rotation of phenyl rings in aqueous solution makes **20** to be less emissive and fluorescence is turned on upon incorporation of CB[7] to **20** due to restricted rotation (Fig. 9). Addition of spermine which competitively binds to CB[7], affects the release of **20** and gives OFF signal. Similarly other fluorescent probe **22** is fabricated in a similar approach using 1-adamantanamine (AD) [CB8]. Selectivity challenge of **21** is conducted using different polyamines, and fluorescence intensity was vastly quenched in spermine whereas no detectable variation in the intensity for other amines except that spermidine affects slight decrease than spermine. Incorporation of CB[8] into **20** induced large aggregate formation along with restricted rotation of phenyl ring which is evident by fluorescent imaging experiments (Fig. 9E).

The detection and analysis of DNA are worth aspect in diagnosing genetic diseases and to monitor biological processes. Fluorescence assays based on AIE effect are best among the label-free DNA sensors, especially when AIEgens are featured with positive charge(s) show electrostatic attraction towards DNA to form aggregates. Thus *cis*-TPE macrocycle diammoniums with two ammonium arms in *cis* (**23** and **24**) and geminal (**25** and **26**) positions
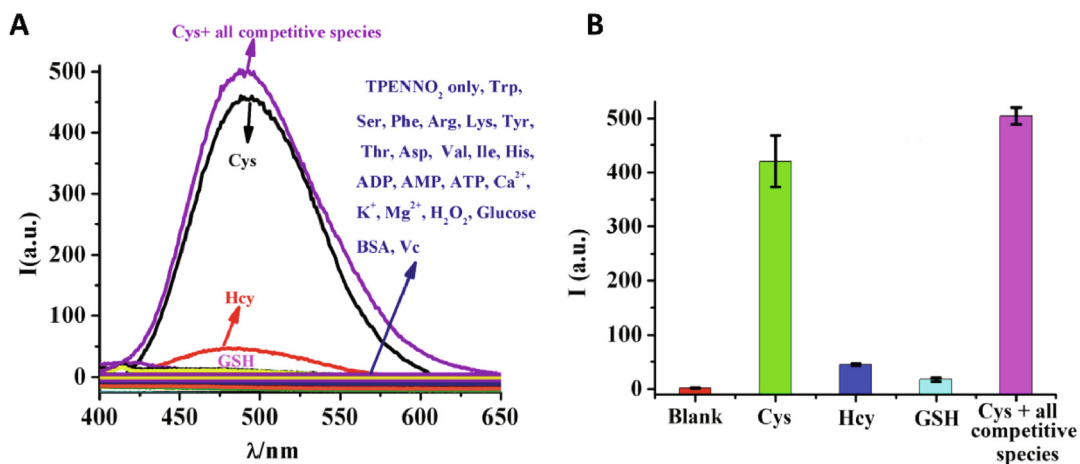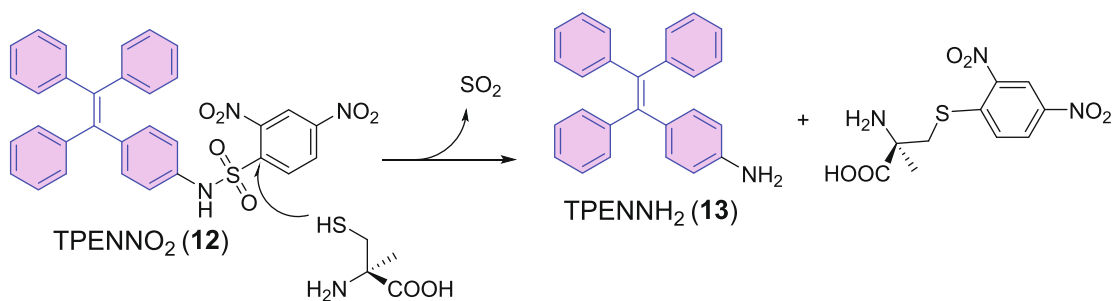
Fig. 5. Structures of **12** and **13** and schematic illustration of light-up sensing of Cysteine by **12**. (A) The fluorescence responses of **12** (25 µM) in PBS towards various biomolecules; (B) Bar graph of response of **12** (25 µM) in PBS towards Cys, Hcy, GSH, and other amino acids. Reproduced with permission from [63]. Copyright 2017 Elsevier.
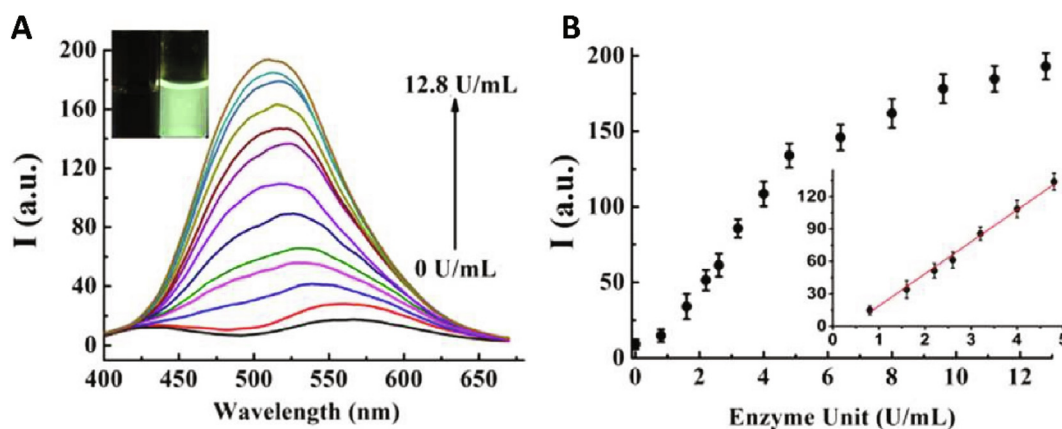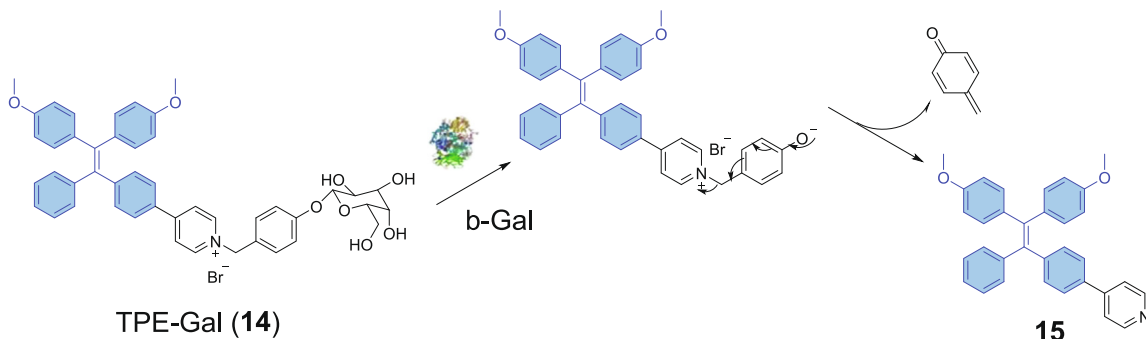

Fig. 6. Structures of **14** and **15** and revealing light-up sensing of β-galactosidase. (A) Fluorescence emission spectra of **14** (inset displays the photographs of **14** with and without β-galactosidase in 365 nm UV light); (B) Fluorescence intensity at 512 nm with various concentrations of β-galactosidase (inset displays linear plot of fluorescence vs β-galactosidase concentration at 512 nm). Reproduced with permission from [64]. Copyright 2017. The Royal Society of Chemistry.
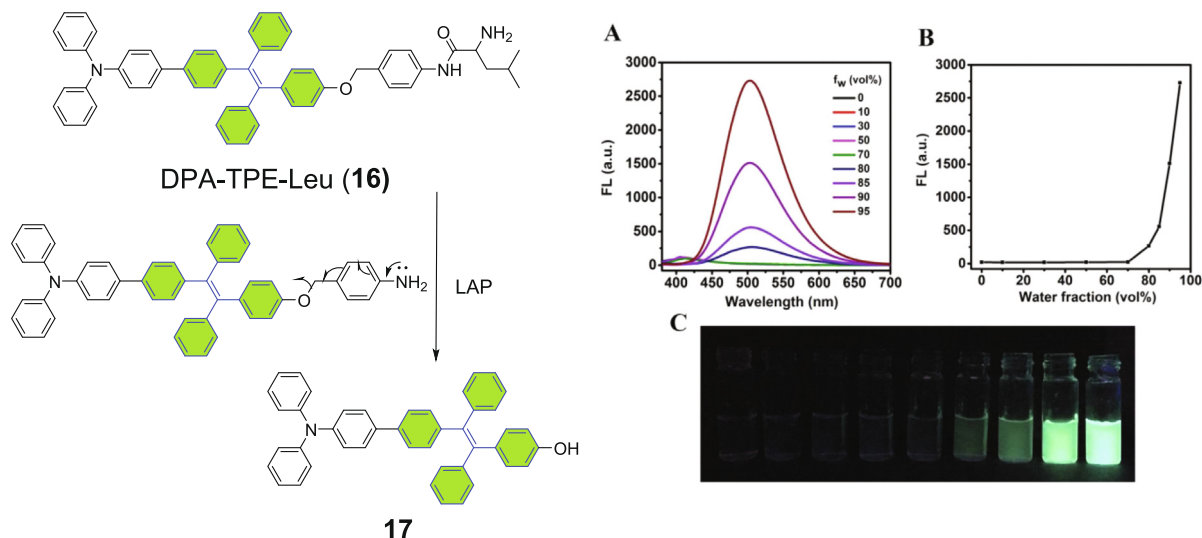
Fig. 7. Structures of **16** and **17** and schematic illustration of probe **16** (A) Fluorescence spectra of **17** in THF/water mixture; (B) fluorescence intensity of **17** at 505 nm as a function of water fraction; (C) photographs of **17** in THF/water at 365 nm. Reproduced with permission from [83]. Copyright 2018 Elsevier.
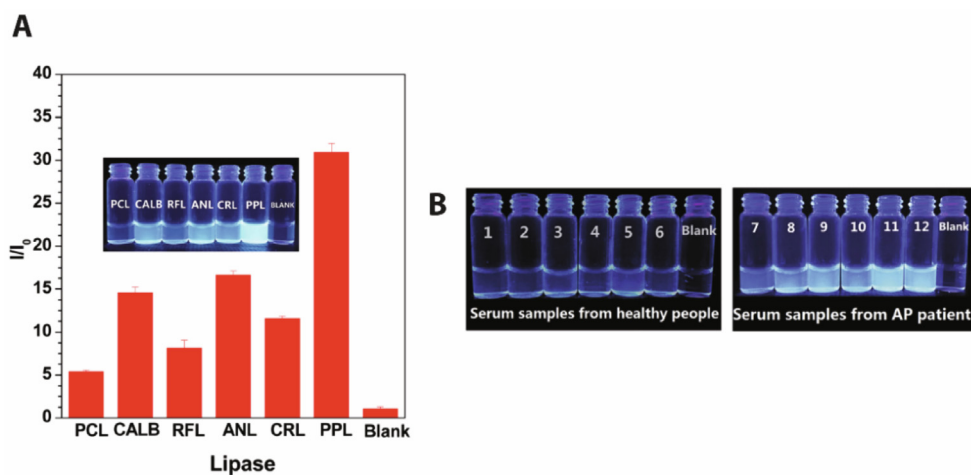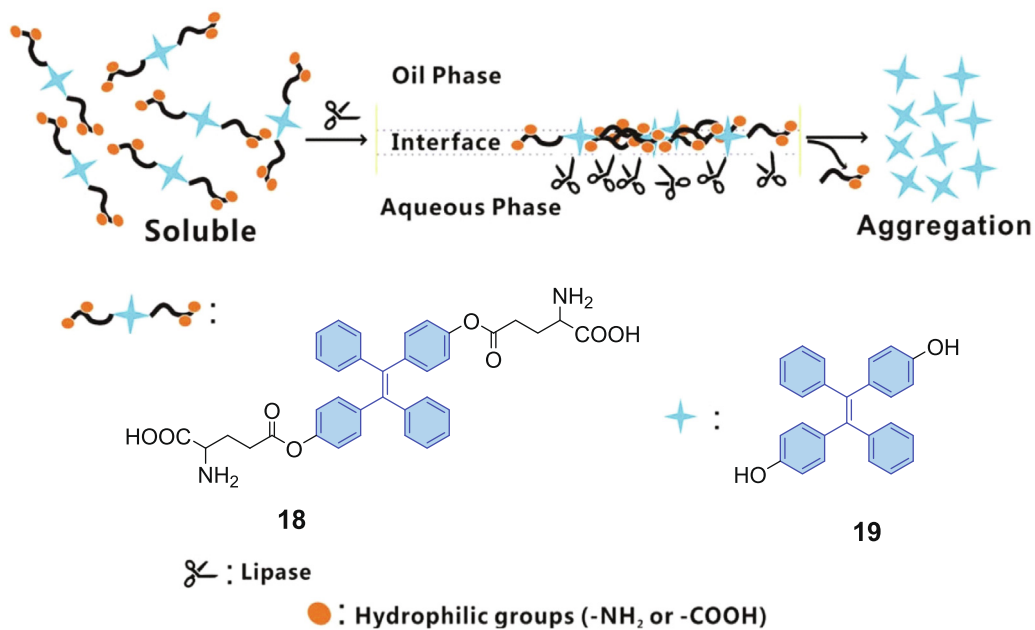

Fig. 8. Structures of **18** and **19** and schematic representation of sensing mechanisms of probe **18** in detection of lipase. (A) I/I₀ value of probe **18** vs lipase samples (fixed concentration); (B) Fluorescence photograph of probe **18** with human serum samples. Reproduced with permission from [84]. Copyright 2017. The Royal Society of Chemistry.
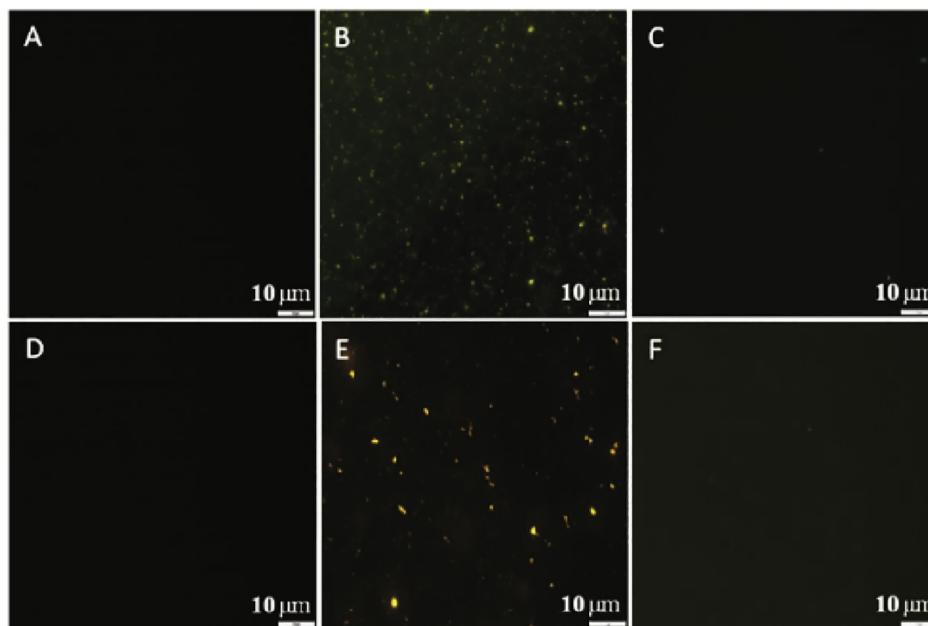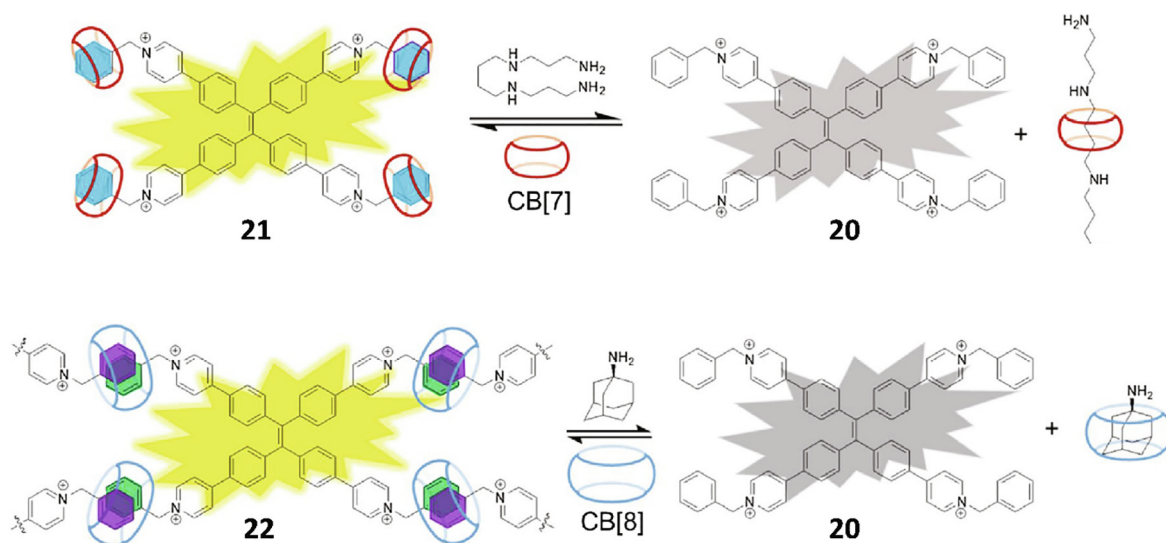
Fig. 9. Structures of 20–22. (A) Fluorescent images of 20; (B) 20 + CB[7]; (C) 20 + CB[7] + Spermine; (D) 20; (E) 20 + CB[8] and (F) 20 + CB[8] + AD (in H₂O containing 1% DMSO). The concentrations of 20, CB[7], Spermine, CB[8], AD are 5 M, 20 M, 20 M, 10 M and 20 M, respectively. Reproduced with permission from [85]. Copyright 2018 Elsevier.

(Fig. 10) were employed for DNA detection [86]. Both *cis* forms 23 and 24 displayed bisignate CD signals upon addition to calf thymus DNA (CT-DNA), indicating the robust DNA induction and the stable immobilization in propeller-like conformation of TPE (Fig. 10A). In contrast, there are no bisignate bands for geminal isomers suggesting more TPE unit flexibility than in the *cis* counterparts when they bind with DNA (Fig. 10B). In addition, TPE diammoniums used to sense DNA and interestingly *cis*-TPE ammoniums were more sensitive than geminal isomers, besides 24 displays higher sensitivity than 23 for detection of FS-DNA and CT-DNA probably due to the overlapping distance of two ammonium arms in 24 isomer with two phosphate anions in the DNA double-helical chain. This ultrasensitive DNA detection by *cis*-TPE macrocycle diammoniums is attributed to the AIE mechanism of restriction of double-bond rotation (RDBR) in the excited state.

3. TPE-based fluorescent sensors for detection of ions

Identification and assessment of metal ions play a key role in environmental and biological investigations [87,88]. For example, zinc (Zn²⁺), silver (Ag⁺), and mercury (Hg⁺) ions are involved in various pharmacological studies, such as antimicrobial, antitumor, anticancer, and other bio-molecular science therapy [89–91]. In general, TPE analogue only acts as an AIE-fluorophore [92], therefore detecting ions in the media requires a chelating/binding group in TPE derivatives. Various TPE derivatives have been studied in the literature for detecting ions such as Cu²⁺, Fe³⁺, Hg²⁺, Ag⁺, F⁻, CN⁻, NO₃⁻ etc. and utilised as an alternative to chemosensors.

In another work, Yuming Zhao et al [93] developed a pH-triggered self-assemblies of polymeric nanoparticles (PNPs) with

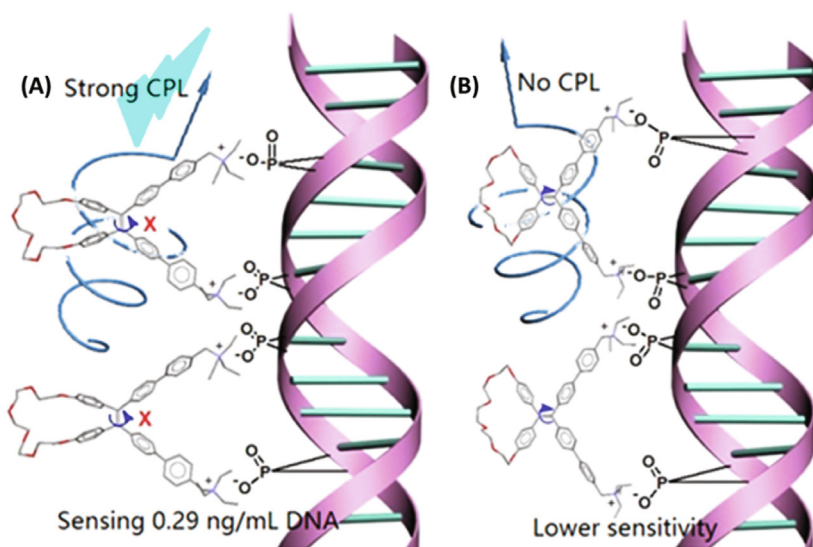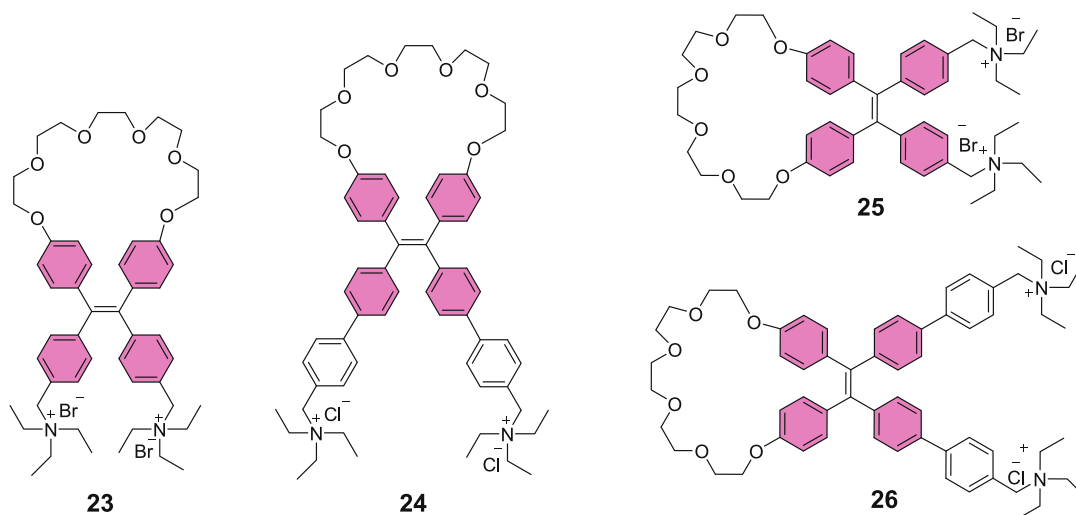**Fig. 10.** Structures of **23–26**. Computational simulations of the binding of (A) **24** and (B) **26** to a DNA strand. Reproduced with permission from [86]. Copyright 2020 American Chemical Society.
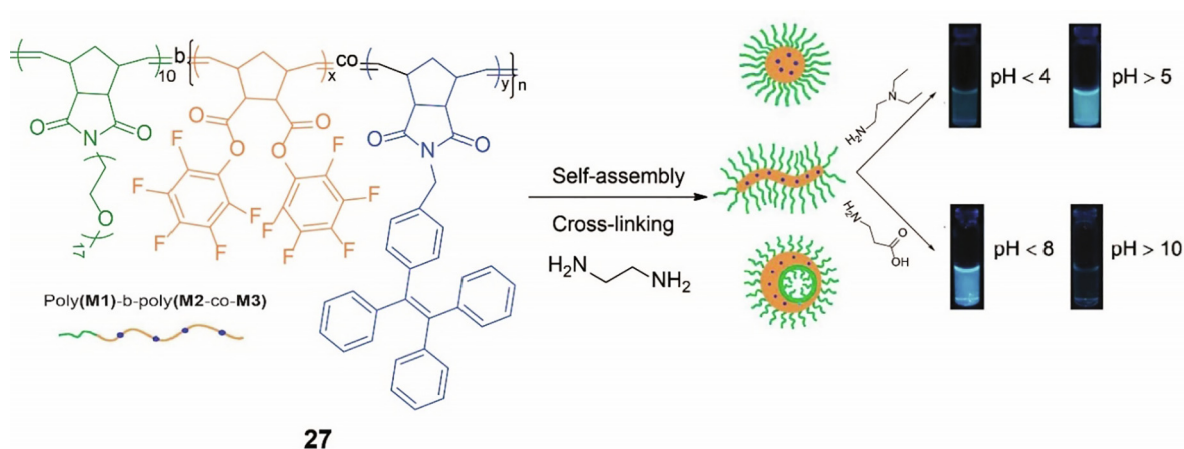
Fig. 11. Synthesis of poly(**M1**)-*b*-poly(**M2**-*co*-**M3**) block copolymer **27** with pH-response AIE activity. Reproduced with permission from [93]. Copyright 2016 The Royal Society of Chemistry.
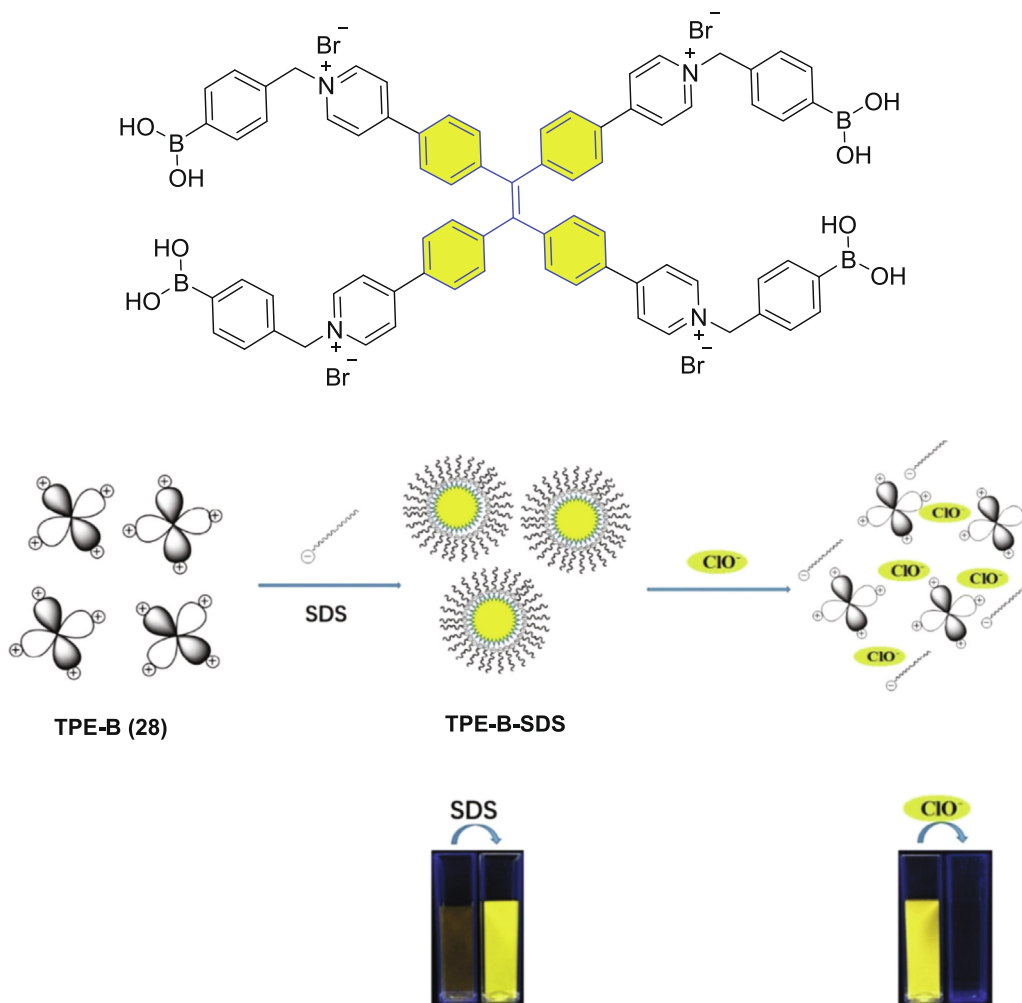
Fig. 12. Structure of **28** and representation of fluorescence nanoprobe **28** for sequential recognition of SDS and ClO⁻. Reproduced with permission from [94]. Copyright 2019 Elsevier.
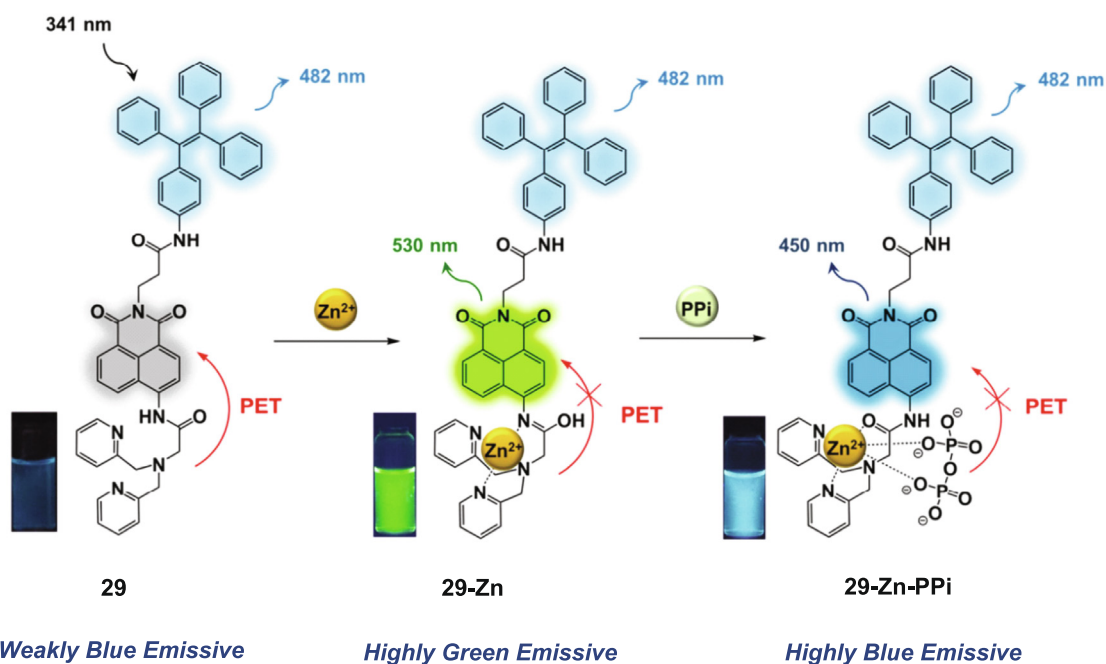
Fig. 13. Structure and sensing mechanism of **29** for detection of Zn²⁺ and PPi ions. Reproduced with permission from [95]. Copyright 2018 Elsevier.

Fig. 14. Structure of ligand **30** and self-assembled illustration of Metal-Organic Nanobelt **31**. Fluorescence responses of complex **31** in 2 mL of CH_3CN/H_2O at 298 K (v/v, 1/1; c = 7.04 × 10^{-6} M); (A) Photographs (λex = 365 nm) and (B) Relative fluorescence intensity of after and before addition of 4.0 μmol interfering species. Reproduced with permission from [96]. Copyright 2020 American Chemical Society.

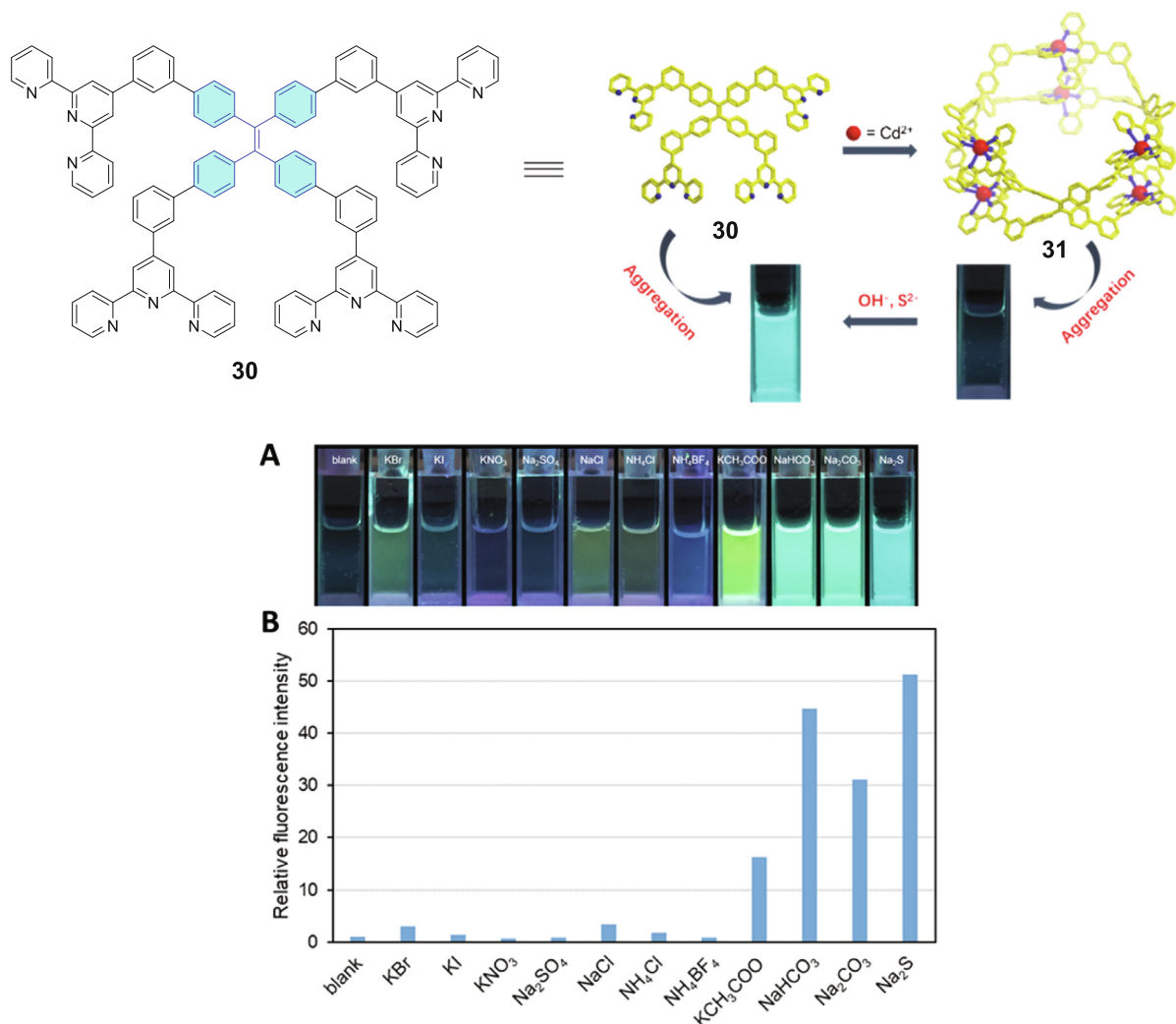AIE-activity based on amphiphilic block copolymer (Fig. 11). Towards this, they have synthesised polymer **27** by ring-opening metatheses polymerization (ROMP) technique, where hydrophilic **M1** contains a PEG side chain and reactive pentafluorophenyl and an AIE active TPE ester in hydrophobic **M2**-co-**M3**. Here, the self-assemblies were started by the aggregation of hydrophobic micro-domains of poly(**M2**-co-**M3**) blocks which is further cross-linked by reacting with diamine to produce stable PNPs. The cross-linked PNPs were further post functionalized with diethylamino or carboxylic group by reacting with *N, N*-diethylethylenediamine (DEDA) and β-alanine, resulting in pH tunable fluorophores in water with weak fluorescence above pH 10 and strong fluorescence below pH 8. Moreover, the turn on/off fluorescence property of functionalized PNPs was obtained by varying pH between 2 and 11.

The synthesis of TPE based AIE active cationic organic building block **28** as nano-probe for sodium dodecyl sulfonate (SDS) and hypochlorite (ClO$^-$) detection in water was reported by Zhan Zhou et al (Fig. 12) [94]. The luminophore **28** exhibited poor fluorescence emission in water and the emission could be enhanced six-fold by treating with SDS as a surfactant (average size of 45 nm). More importantly, a switch on–off fluorescence has been observed upon addition of ClO$^-$ and this could allow determining the accurate concentration of reactive oxygen species (ROS).

In 2018 Chang and Lee [95] reported fluorescent micellar probe for Zn^{2+} and pyrophosphate ions (PPi) detection, which contains a TPE derivative as an AIEgen and a chelating fluorophore dipicoly-lamine (DPA)-naphthalimide. The micellar probe was formed by mixing with sodium dodecyl sulfate (SDS) (Fig. 13). When exciting at 341 nm, this micellar probe **29** displays a very weak blue fluorescence at 482 nm which is attributed to the AIEgen property of the TPE, where the chelating fluorophore was inactive due to photo-induced electron transfer (PET) from DPA to naphthalimide. However, the probe **29-Zn** exhibits a strong green fluoresce at 530 nm in presence of Zn^{2+} due to suppression of PET impact indicating the chelation of Zn^{2+} with DPA. Moreover, after chelation with Zn^{2+} the probe showed a strong affinity to PPi that affects the change in fluorescence intensity from 530 to 474 nm due to the possible rearrangement of Zn^{2+} ions with PPi. The detection limit found to be 46 and 88 nM for Zn^{2+} and PPi ions, respectively in the 5–10 pH range. Thus, TPE linked fluorescent micellar probe demonstrated as promising agents for imaging Zn^{2+}/PPi related physiological responses.

Metal-organic supramolecular nanobelt bearing AIE active TPE core as a turn-on fluorescence sensing probe for sulfide ion (S^{2-}) was designed by Kaixiu Li et al (Fig. 14) [96]. An AIE active TPE based tetrapodal ligand was synthesized, which formed a self-
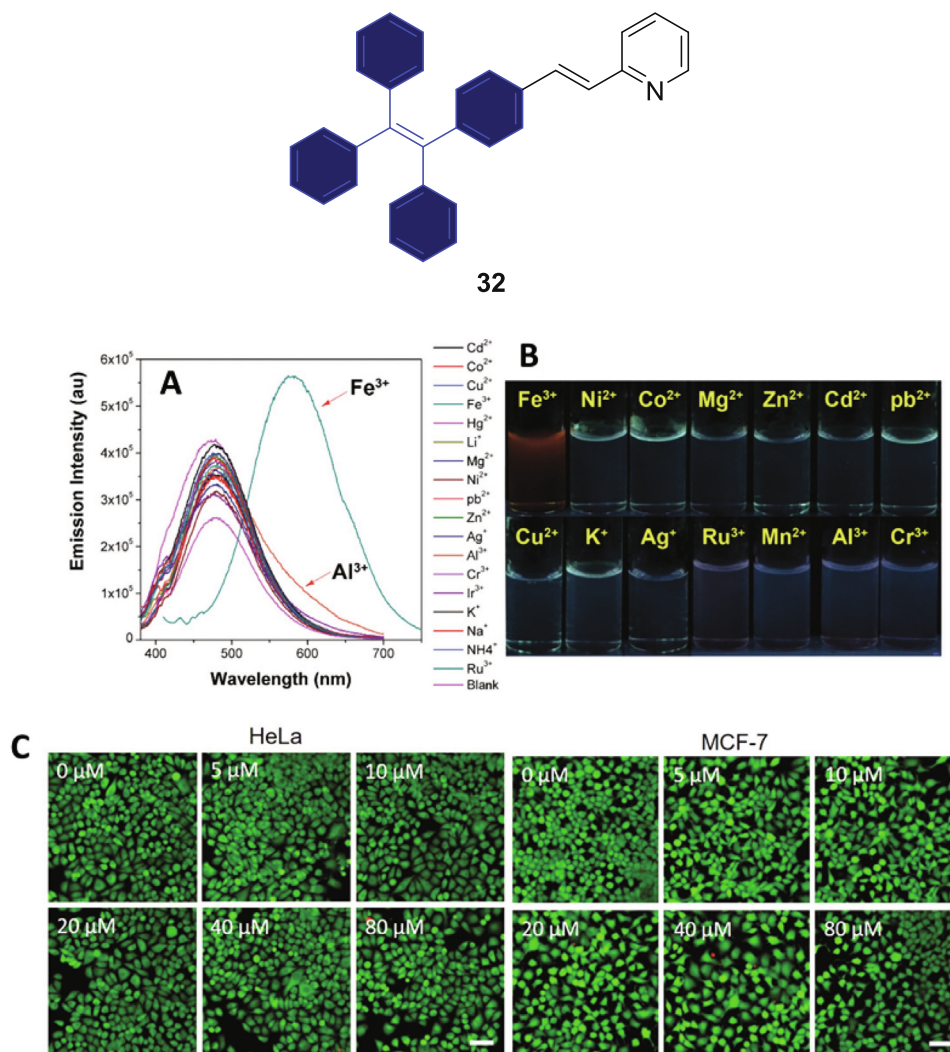
32

Fig. 15. Structure of **32**. (A) PL spectra of **32** in presence of metal ions with 1.67×10^{-4} M concentration in THF and THF/water system (f_w = 70%); (B) Photographs of the mixtures of **32** (10×10^{-6} M) with different metal cations at 365 nm; (C) Fluorescence images of HeLa and MCF-7 cells. Reproduced with permission from [97]. Copyright 2018 WILEY-VCH Verlag GmbH & Co.

assembled nanobelt by complexing with Cd^{2+}. The presence of TPE moiety in the terpyridine ligand **30** makes strong emission in the aggregated state, but emission was turned-off in both aggregation and solution states after formation of the nanobelt **31**. Interestingly, the complex **31** underwent structural transformation to **30** and turned on its fluorescence property in alkaline solution or in presence of S^{2-}. This reversible transformation is due to the cadmium salt formation, therefore the metal–organic nanobelt **31** can be utilised as a turn-on sensor to detect S^{2-} ions. Moreover, the complex **31** tested with the addition of various metal salts in CH_3CN/H_2O mixture, the complex shows a specific emission enhancement with Na_2S, indicating that the complex **31** possesses a stimuli responsive emission specifically to S^{2-} ions.

In 2018 Xing Feng et al [97] designed a pyridinyl-functionalized TPE derivative for specific detection of Fe^{3+} ions in THF/water mixture (Fig. 15). This turn-on fluorescence probe can identify only Fe^{3+} ions in presence of various cations even at concentrations of up to 1.67×10^{-4} M, leading to fluorescence emission changes to strong red from weak blue in Fe^{3+} ions. Further, only hydrolysed Fe^{3+} among different metal ions with pK_a (3.20) was lower than **32** pK_a (≈ 3.27) and can induce protonation of **32** in water, owing

to different solubility products of the other metal ions, it is improbable to decrease the pK_a to 3.27 and protonate **32** in aqueous solution. The pH-dependent sensitivity and selectivity of **32** to detect Fe^{3+} is observed *in vitro* cellular imaging of HeLa and MCF-7 cancer cells. HeLa cells which are incubated with **32** and without Fe^{3+} emitted deep blue fluorescence, and blue and red fluorescence emitted simultaneously in the presence of Fe^{3+}. Increased red fluorescence intensity was observed with elevated Fe^{3+} concentration suggesting a potential utility of **32** as ratiometric fluorescence probe for detection of Fe^{3+} in live cells.

Porous materials have potential impact in chemical sensing, introduction of AIEgens into various porous crystalline materials including covalent organic framework (COF), hydrogen-bonded organic framework (HOF), metal organic framework (MOF) etc. providing a new fluorescence materials with enhanced sensing properties. Yingting Zheng and co-workers [98] have fabricated 1,3,5-triazine containing porous tetraphenylene-based organic polymer (PTOP) **33** (Fig. 16) possessing large chelating areas for metal ions, in which TPE AIEgen synergise the porous structure for sensing Fe(III). The fluorescence of **33** is completely quenched in presence of Fe^{3+} (Fig. 16a), this selective fluores-
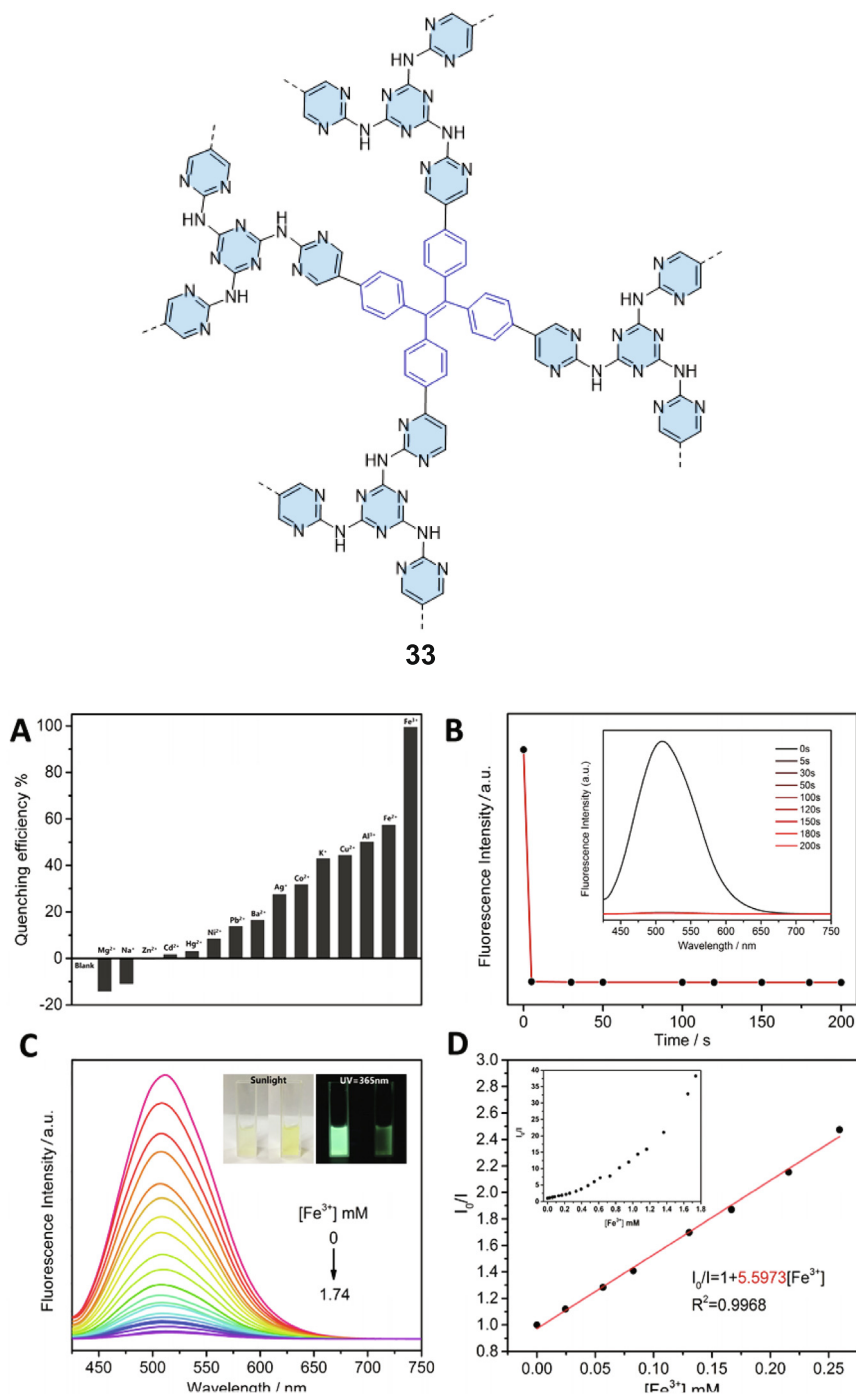
33

Fig. 16. Structure of **33**. (A) Quenching efficiency of **33**; (B) Time-dependent emission intensity of 33 immersed in a MeOH solution of Fe^{3+} ion; (C) Emission spectra by the gradual addition of a Fe^{3+} methanol solution; (D) Ksv curve of **33** immersed in MeOH solutions of Fe^{3+} ion with different concentrations. Reproduced with permission from [98]. Copyright 2020 Elsevier.

cence sensing attributed to synergistic impact of *d* orbit and paramagnetism. Quenching sensitivity experiment gives K_{SV} of 5.6 mM^{-1} (K_{SV}: the quenching constant) for **33** (Fig. 16d) with limited detection concentration of 4.5 μM for Fe^{3+} fluorescence sensing based on $3\sigma/K_{SV}$ equation (σ: standard deviation). The quenching mechanism of **33** by Fe^{3+} is through the insertion of Fe^{3+} within the pores of **33**.

Detection of Al^{3+} ions is of great importance as its accumulation induces many disorders. Fluorescence chemosensors got much attention for the detection of various analytes including Al^{3+} than conventional detection techniques. COF-based on the tetrakis-(4-aminophenyl)ethane and 2,5-dihydroxyterephthaladehyde (COF-DHTA) **34** (Fig. 17) was employed by Jian Xiu and co-workers [99] to selectively detect Al^{3+} ions. COF-DHTA **34** dispersed uniformly in most of the solvents and exhibited stronger fluorescence
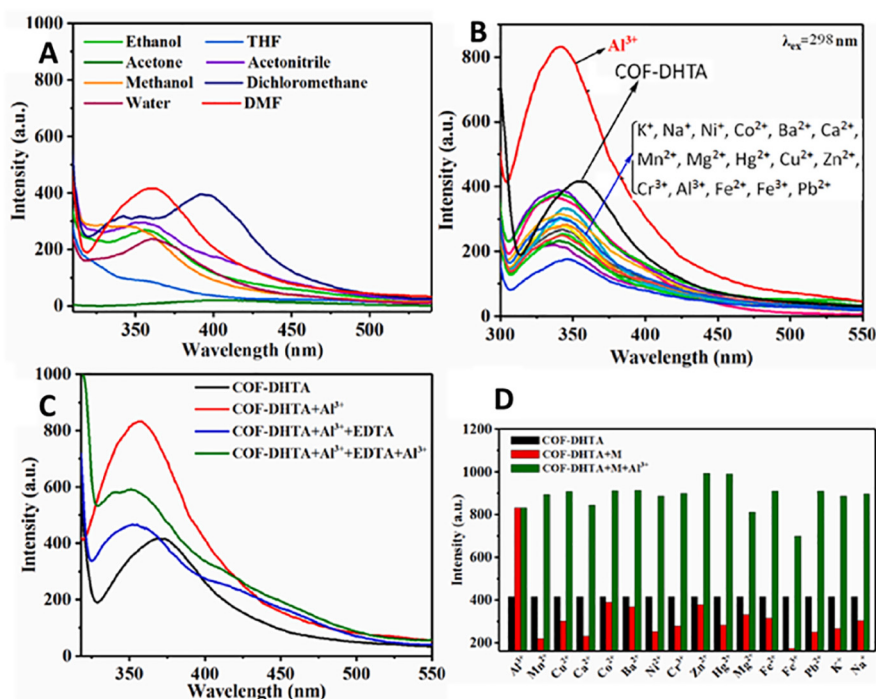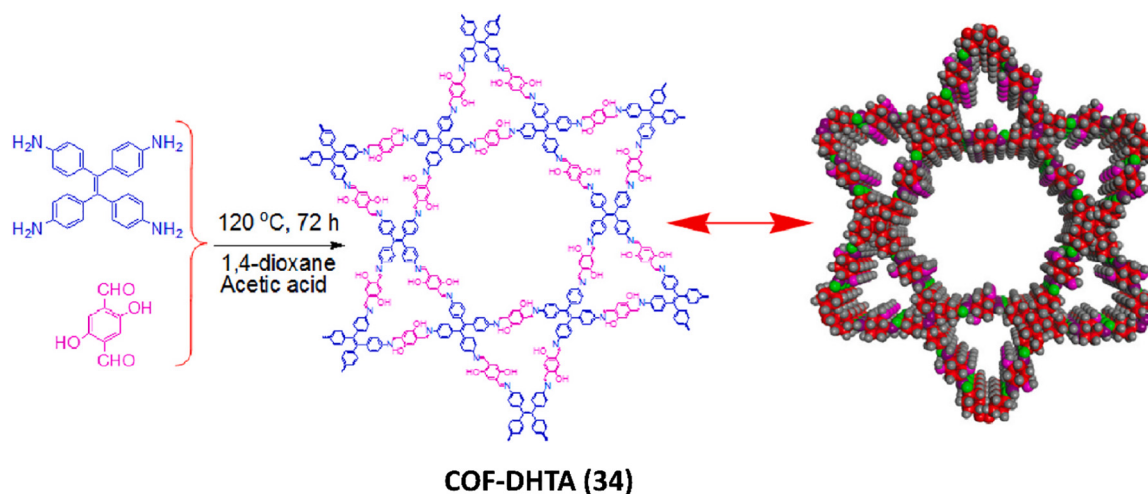
13

COF-DHTA (34)

Fig. 17. Schematic illustration of **34** (COF-DHTA). (A) The fluorescence spectra of **34** in different solvents; (B) The fluorescence spectra of **34** in different metal ions (40 µmol/L); (C) The fluorescence spectra of **34** in the presence and absence of Al^{3+} ions and EDTA; (D) Competitive experiments of **34** in DMF in the presence of Al^{3+} ions and the various metal ions (40 µmol/L), respectively. Reproduced with permission from [99]. Copyright 2021 Elsevier.

emission (Fig. 17a) in DMF. The fluorescence intensity greatly enhanced upon addition of Al^{3+}ions than any other metal ions (Fig. 17b), attributed to the synergetic impact of COF pore and the coordination of nitrogen and oxygen on the **34** with Al^{3+} ion. The complexing process of **34** with Al^{3+} ions found to be coordination process and reversible (Fig. 17c). The sensitivity of **34** towards Al^{3+} doesn't affected in presence of other metal ions (Fig. 17d).

4. TPE based AIE luminogens for bioimaging

Fluorescence imaging of cells has been extensively used for biomedical applications today because of its unique feature to visualize biological process inside the cell [100]. So far, various bio-imaging techniques including molecular imaging, photon emission computing tomography and MRI techniques are utilized for visualization of live cells, tissues, and molecules in living organisms [101–105]. Among various bioimaging techniques, fluorescent imaging is the most common approach that has gained considerable attention because of its photostability, low cytotoxicity, and biocompatibility. During last few decades, a range of fluorescent probes including carbon dots [106], semiconducting polymer nanoparticles, 2D-nanomaterials, metal nanoclusters, organic dyes, supramolecular (assembled) organic substances, semiconducting quantum dots etc [107–111] have been successfully developed and utilized for biomedical applications [19]. Recently, AIE turn-on fluorescent probes have gained much attention and successfully utilized for real-time imaging [112], long term cell tracking [113], organelles [114], tracing cell process [115], roles of biomolecules in living system [116–118],

35
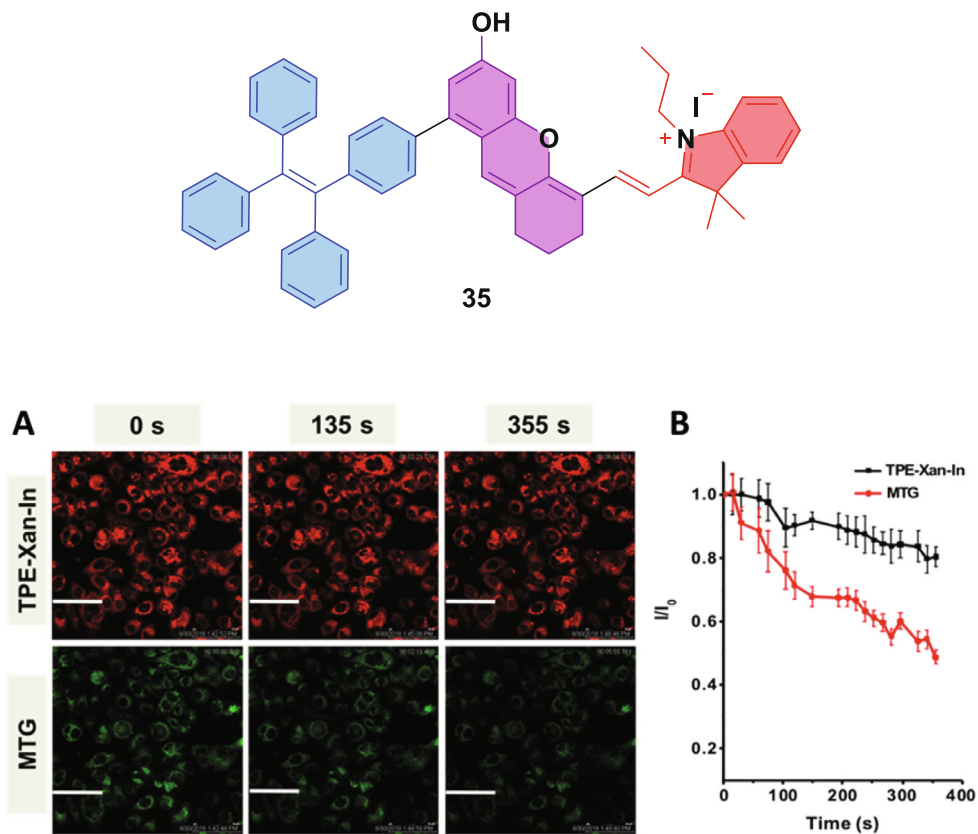
Fig. 18. Structure of **35**. (A) Fluorescence images of HeLa cells stained with **35** and MTG; (B) I/Io plot value of HeLa cells stained with **35** and MTG. Reproduced with permission from [122]. Copyright 2019 American Chemical Society.

36

37
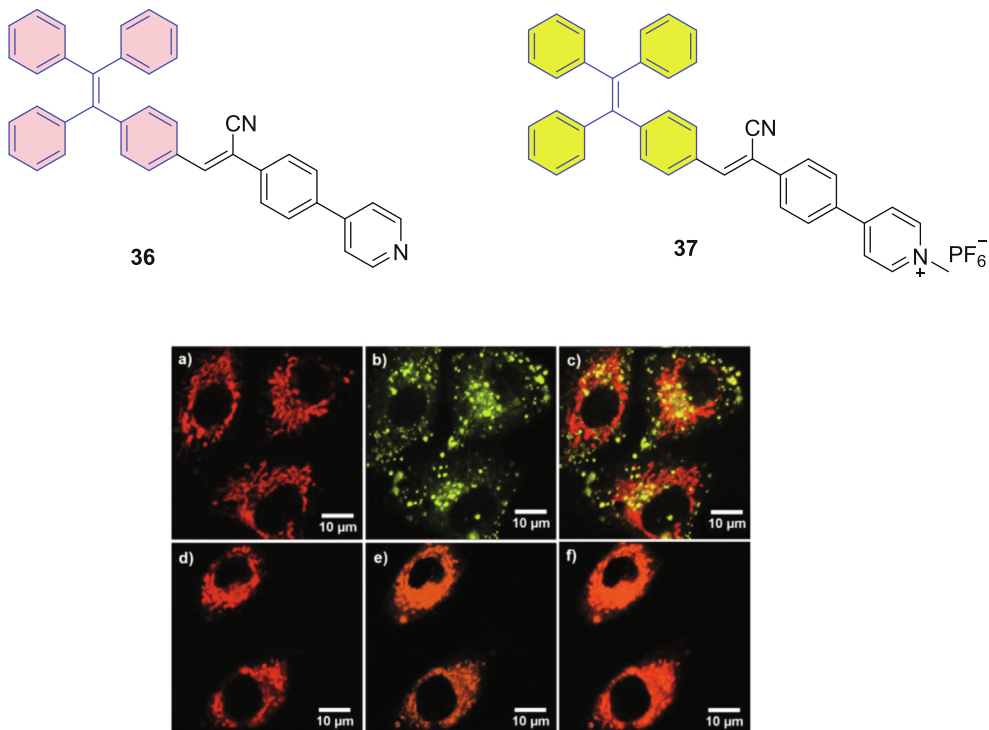
Fig. 19. Structure of **36** and **37**. (a–c) CLSM images of MitoTracker Deep Red FM with **36** and **37**; (d–f) in A549 cancer cells; (a, d) Mito Tracker stained mitochondrial fluorescent image; (b, e) Fluorescent image of mitochondria stained by **36** & **37**; (c) An overlay image of (a) & (b); (f) an overlay image of (d) & (e). Reproduced with permission from [123]. Copyright 2020 The Royal Society of Chemistry.

Fig. 20. Schematic mechanism of detection of GlcNAc-TPE (**38**) and Py-TPE (**15**). (A) LysoTracker Green DND-26; (B) GlcNAc-TPE (**38**); (C) A and B merged images; (D) Fluorescence intensity profiles along the white lin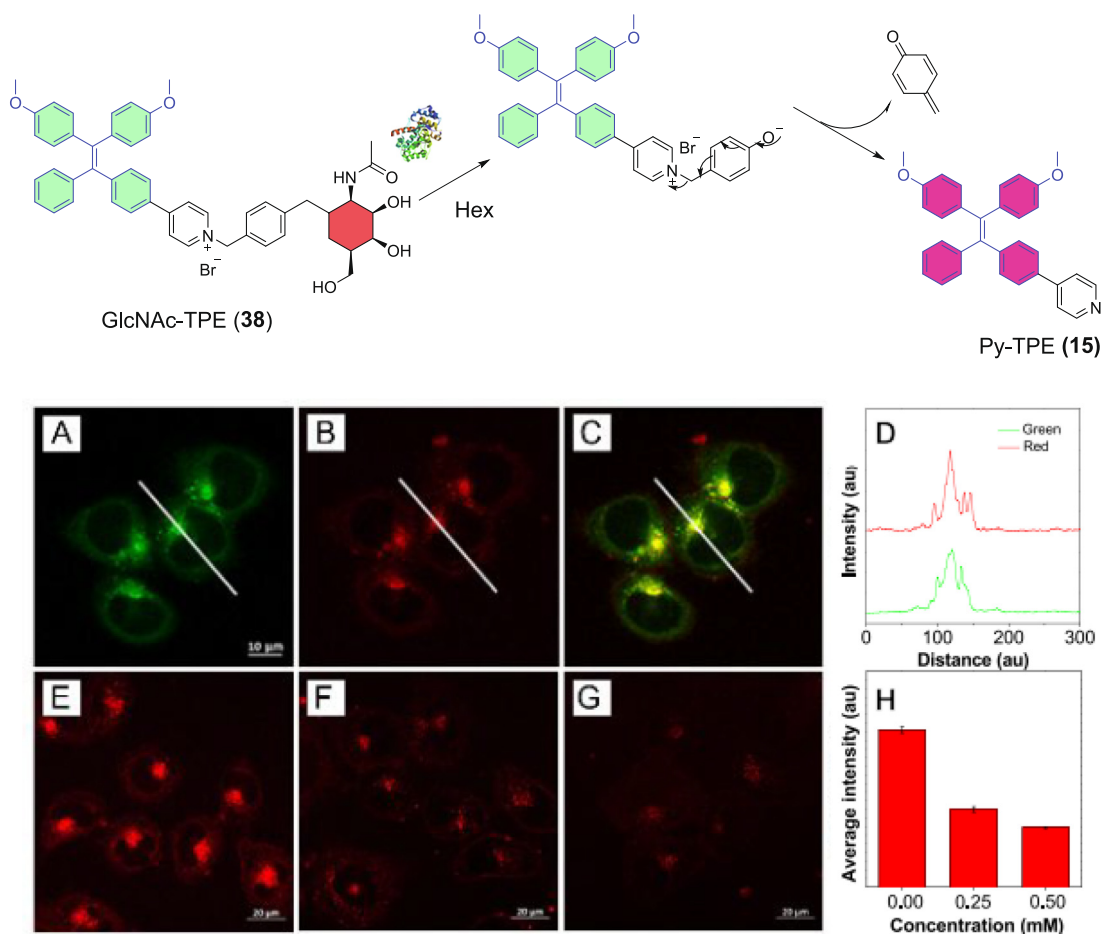e; (E-G) CLSM images of cells stained with **38**; (H) Average intensity of cells stained with **38** in the absence and presence of PUGNAc. Reproduced with permission from [124]. Copyright 2019 American Chemical Society.

macromolecular mapping [119,120]. Besides, these probes are biocompatible and affordable and can be utilized for detection of cancer cells [121].

Xiujie Zhao and co-workers [122] reported near-infrared TPE–Xan–In (**35**) as a turn-on AIE-active probe consisting of TPE with a NIR merocyanine unit (Xan-In) for long-term mitochondrial tracking. The as-synthesized TPE–Xan–In (**35**) is explored for AIE characteristics at different pH levels in the THF-water system. It was observed that the TPE–Xan–In (**35**) at pH < 6.0 in 70% water is non-emissive and hardly aggregates due to formation of phenolate ion, whereas at pH greater than 6.0, especially at 7.0 the probe is highly emissive and forms aggregates due to generation of phenolic form, which could be ascribed to the AIE characteristics. The authors have carried out cytotoxicity assay of HeLa cells by treating TPE–Xan–In (**35**) up to 100 μM concentration for 48 h and showed that the cells are viable. Further, authors have carried out photooxidation stability of the probe TPE–Xan–In (**35**) by scanning the stained HeLa cells for various times and monitoring the mitochondrial membrane (Fig. 18) and found suitability of probe for long-term mitochondria imaging. Moreover, the authors have also carried out the effect of pH for imaging of mitochondria using the probe TPE–Xan–In (**35**) by adjusting intercellular pH between 4.0 and 7.0 and as the pH increases the fluorescence intensity significantly increased. Therefore, TPE–Xan–In (**35**) probe is effective for tracking the morphology changes of mitochondria due to changes in intercellular pH.

In recent times, Xinzhe Yang et al [123] have developed the TPE based luminogens TCPy (**36**) and TCPyp (**37**) for imaging mitochondria and secondary AEE for long term tracking of tumour exhibiting mechanochromism and AIE characteristics. The as-synthesized pristine solid of TCPy (**36**) exhibits maximum emission at 512 nm in high Φs,o up to 0.90 in solid-state, upon grinding the peak shift to 526 nm suggesting that the luminogen **36** is highly sensitive to an external force. Whereas the solid TCPyp (**37**) in pristine solid emits highly emissive green colour with maximum emission at 527 nm and Φs,o value obtained for this luminogen is 0.52. Further, upon grinding, the colour changes to red with maximum at 617 nm, this colour can be returned to its original colour when fuming with dichloromethane vapour (Fig. 19). Further examination using single-crystal XRD analysis of solid TCPyp (**37**) reveals that the mechanochromic behaviour is due to the deterioration of intermolecular interactions among hexafluorophosphate anions present in the crystal under mechanical stimuli, resulting in the conversion of *H*-aggregates to *J*-aggregates. The mitochondria imaging and cytotoxicity assay of luminongens TCPy (**36**) and TCPyp (**37**) in A549 cancer cells suggest that these AIEgens successfully penetrate through cytomembranes, and show good biocompatibility in cells (Fig. 19). Moreover, the *in vivo* imaging studies of mice suggests that this ionic AIEgen TCPyp (**37**) can track tumor for long-term in nude mouse. From these findings, it can be suggested that the luminogen TCPyp (**37**) has potential applications in security systems, sensors, and also in the detection of cancer.
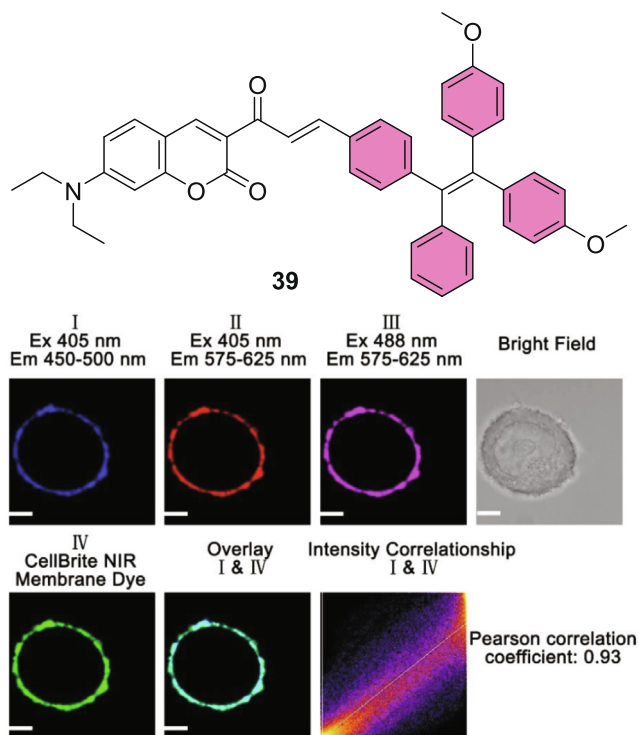
Fig. 21. Structure and fluorescence images of probe **39** (10 μM) incubated with MCF-7 cell along with NIR dye (5 μM). Reproduced with permission from [125]. Copyright 2020 American Chemical Society.

The dysfunction of β-*N*-acetylhexosaminidase (HsHex) enzyme leads to neurodegenerative lipid storage disorders and its up-regulation in lysosomes accounted for human breast and colorectal cancers. It is a good idea to target this enzyme in lysosome in situ and real-time visualization of Hex using fluorescent imaging, would be a great tool in cancer diagnosis and drug discovery. There

are very few fluorescent probes for real-time imaging of Hexs with lysosome-targeting ability, whereas GlcNAc-TPE **38** fluorescent probe (Fig. 20) found to be sensitive and selective in Hex detection in live cells [124]. Fabrication of TPE derivative with *N*-acetyl-beta-D-glucosaminide group improves the water solubility of the probe and make the probe to be non emission. Whereas, upon hydrolysis of probe **38** by Hex produces less water soluble Py-TPE probe **15** which results in aggregation induced emission. Probe **38** showed specific response to Hex with large stoke shift and good photostability for in situ visualization of HsHex in live cells. In addition, colocalization study using LysoTrackerTM Green DND-26 (Fig. 20-A-H), a commercial lysosome dye suggests that, **38** can specifically target lysosome and monitor endogenous Hex activity in live HCT116 cells.

Recently, Yibin Zhang and colleagues [125] showed a fluorescent probe **39** in order to visualise the cell-membrane structures by conjugating TPE with coumarin. The probe **39** was synthesized by introducing a coumarin organophosphorus yield into 4-[2,2-Bis (4-methoxyphenyl)-1 phenylethenyl]benzaldehyde. In pure THF, the synthesized probe **39** shows two absorptions at 300 and 457.5 nm and a single emission at 470 nm, whereas the probe **39** aggregates in the mixture of THF/H$_2$O and changes its emission behaviour with the increasing water concentration. The probe in 90% water exhibits two emissions with a new emission at 591 nm and a 12 nm red shift in the actual emission at 470 nm due to the formation of aggregates. The cytotoxicity and photostability of probe **39** were studied in HeLa cells using standard MTT assay suggest that cells are viable up to 86% and showed low cytotoxicity and good photostability. Further, the authors have carried out cellular fluorescence imaging of HeLa Cells after 15 min incubating Cell Brite cell membrane NIR dye with probe **39** suggests that it can solely stain the cell membrane of HeLa cells (Fig. 21). Moreover, the authors have also utilized probe **39** in fluorescence imaging of various cell membranes including breast cancer MCF7 cells. These results display that probe **39** specifically stains the cell membranes.

Yuanjing Cai et al. [126] in 2020 projected an AIEgen for lysosomal tracing, which is based on an acidic pH-stable piperazine-TPE **40** probe. AIEgen PIP-TPE (**40**) exhibits yellowish-green emission in
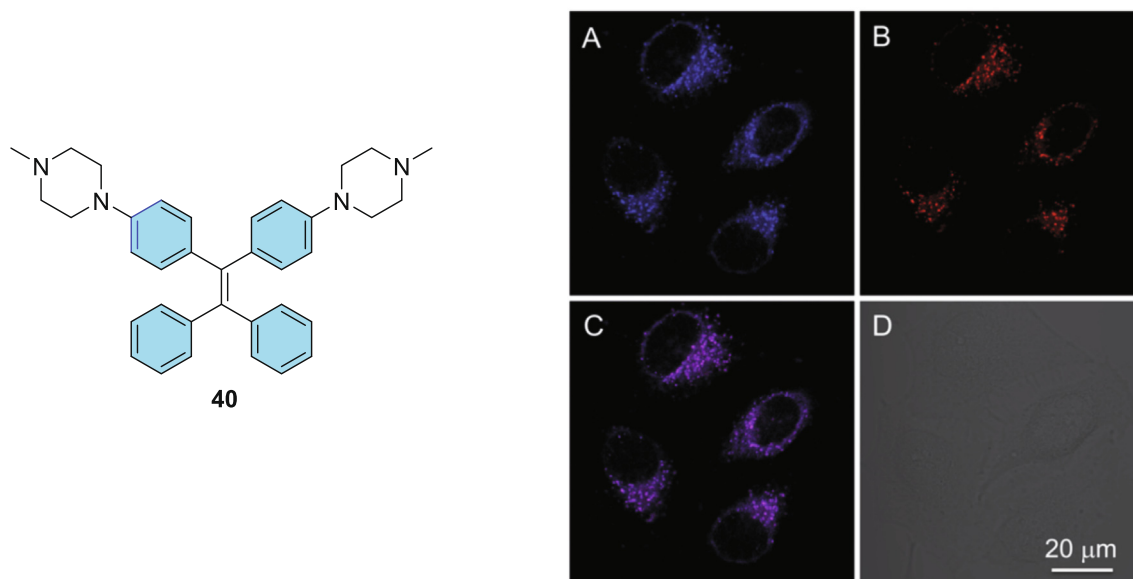

Fig. 22. Structure of **40**. (A & B) Confocal images of **40** (1 mM) and LysoTracker Red (200 nM) co-stained HeLa cells; (C) A & B merged images; (D) Bright field. Excitation wavelength. 40 (405 nm) and Lyso Tracker Red (561 nm). Reproduced with permission from [126]. Copyright 2020 The Royal Society of Chemistry.
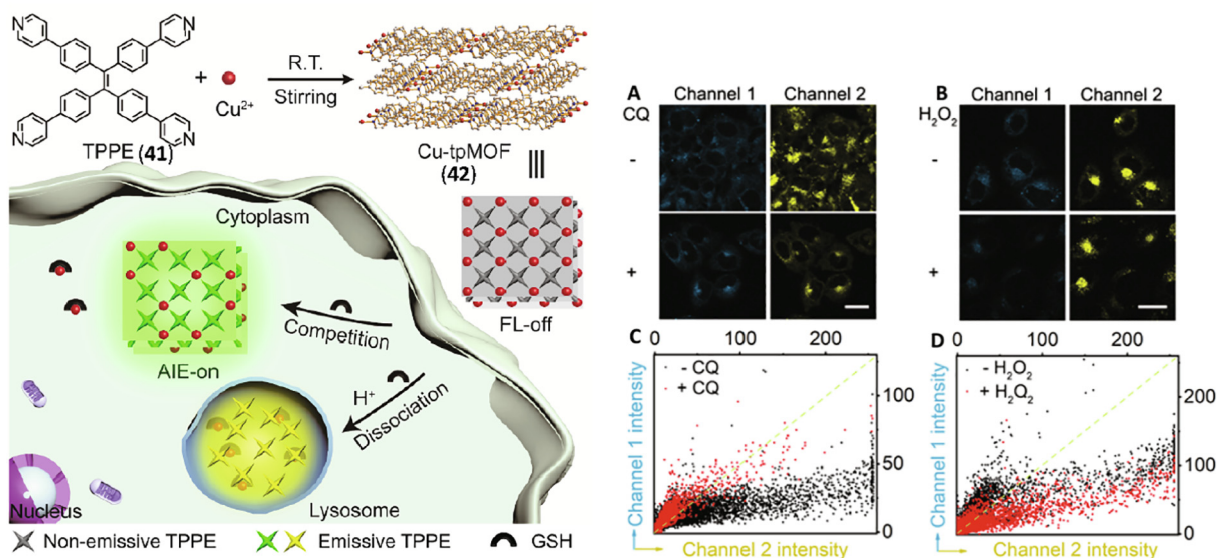
Fig. 23. Preparation route and quencher-delocalized emission strategy of **42** in living cells for profiling of subcellular GSH. Dual-channel confocal images of HepG2 cells pre-treated with and without (A) CQ or (B) hydrogen peroxide followed by incubation with **42** for 2 h. (C), (D) Fluorescence distribution of each pixel in (A) and (B) respectively. Reproduced with permission from [127]. Copyright 2019 WILEY-VCH Verlag GmbH & Co.
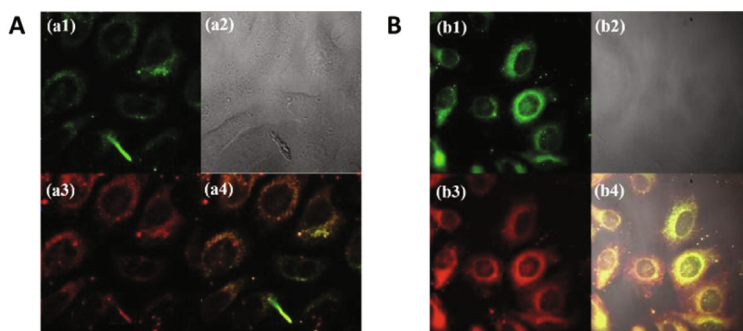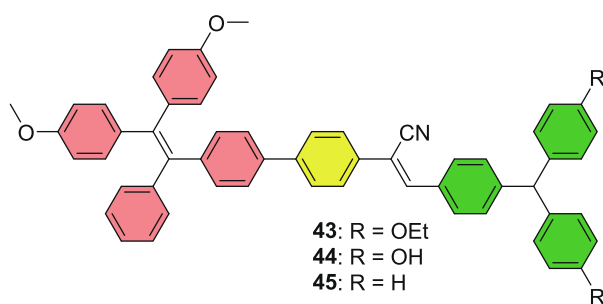

43: R = OEt
44: R = OH
45: R = H

Fig. 24. Structure of solids **43–45**. Cell imaging of (A) **43** and (B) **44**; [(a1, b1) OPEF, (a2, b2) bright-field, (a3, b3) TPEF and (a4, b4) merged images respectively]. Reproduced with permission from [128]. Copyright 2016 The Royal Society of Chemistry.

bulk, whereas in a non-aggregated state, it exhibits deep-blue emission, which could be ascribed to the AIE characteristics. Further, the probe **40** has explored for selective detection of lysosomes in cells by incubating HeLa cells under physiological condition with bio probe PIP-TPE (**40**) along with commercially available probe LysoTracker Red (Fig. 22). The imaging in HeLa cells shows blue fluorescence with the PIP-TPE (**40**) probe and red fluorescence with LysoTracker Red, while the co-staining well merged with a coefficient of 0.82, which confirms the specificity of PIP-TPE (**40**) towards lysosome in live cells. Moreover, the TPE unit in **40** is

hydrophobic, whereas piperazine units are hydrophilic, the incorporation of piperazine helps solubility in acidic medium. Furthermore, the cytotoxicity of probe PIP-TPE (**40**) was also examined through MTT assay and found that HeLa cells at a higher concentration of 5 μM do not show any cytotoxicity. From these results, it was found that the probe PIP-TPE (**40**) has good biocompatibility and high selectivity towards lysosome with a good signal-to-noise ratio.

Longyi Zhu et al [127] have employed tetra(4-pyridylphenyl) ethylene (TPPE) **41**-based metal–organic framework (MOF) with

Cu(II) as the metal node (Cu-tpMOF) **42** as signal transduction platform for in situ imaging of subcellular GSH (Fig. 23), which is key in balancing cellular redox homeostasis. First, Cu(II)-induced electron transfer phenomenon quenches the fluorescence of **42**, however a green fluorescence is resulted upon endocytosis into cytoplasm where Cu(II) was contended by GSH to partly delocalize Cu(II) in AIEgen. There was a complete dissociation of **42** when it is transported to acidic lysosomes and generates yellow fluorescence due to binding between Cu(II) and GSH along with TPPE protonation, offering quencher-delocalized emission strategy for monitoring GSH levels. AIE probe **42** showed good biocompatibility with HEPG2 cells and further investigated the subcellular GSH levels upon treatment of **42** with HEPG2 cells (Fig. 23). Inhibition of lysosome formation was observed when HEPG2 is pre-treated with Chloroquine (CQ) (Fig. 23A) and reduction of GSH was observed after treatment with CQ (Fig. 23C). Fig. 23B and 23D suggest the effective GSH depletion in cytoplasm than lysosome by H_2O_2. These outcomes indicate that **42** is suitable for monitoring subcellular GSH levels upon drug treatment.

Ding and colleagues [128] designed a novel strategy for the generation of D-A-D type structures **43–45** comprising of substituted triphenyl and TPE units which exhibit AIE properties and studied their photophysical properties. The synthesized solids **43–45** exhibit dark yellow, yellow, and green colour with a high quantum yield which is 23.2% for **43**, 11.7% for **44**, and 10.2% for **45,** respectively. Further synthesized solids are explored for solvatochromism in various solvents suggesting that all the solids **43–45** exhibit three absorption peaks, the first one appears at 300 nm, which arises from π-π^* transition of triphenylamine or TPE group, the second one appears at 350 nm and the third one appears at 400 ~ 425 nm, respectively which attributed due to ICT. Moreover, the synthesized solids are explored for AIE characteristics and found that the solid **43** in pure acetonitrile solvent was non-emissive; upon the increase of aqueous fraction the fluorescence intensity improved and gave strong yellow emission at f_w of 90%. Similarly, the solids **44** and **45** emit bright yellow and green light at f_w of 80% and f_w of 90%, respectively. The live-cell imaging and cytotoxicity of luminogens **43–45** were studied in HepG2 and U2OS cells employing standard MTT assay for 24 h suggesting that cells are viable up to 80% for solids **43** and **44** and show low toxicity with excellent biocompatibility compared to solid **45** (Fig. 24). In addition, the luminogens **43** and **44** is successfully utilized for one-photon and two-photon excited fluorescence cell imaging studies. From these results, it was found that luminogens are good candidates for bio-imaging with prominent optical properties and biocompatibility.

Nien-Tzu Chu and co-researchers [129] reported the synthesis of supramolecular hydrogels TPE-Ser (**46**) and TPEAsp (**47**) by simply conjugating TPE with serine (ser) and aspartic acid (Asp) as a side chain. The hydrogelators TPE-Ser (**46**) and TPE-Asp (**47**) form hydrogen bonding in aqueous medium and extend their network to form self-assembly. The synthesized self-assembly was further tested for hydrogelation formation at various pH conditions and found that TPE-Ser (**46**) form stable hydrogel at 2 wt% under a pH of 7.1, whereas for TPE-Asp (**47**) requires slight acidic pH of 6.0 for hydrogelation, and these hydrogels exhibit intensive fluorescence emission in gel state. Further, the authors have carried out biocompatibility of hydrogels through standard MTT assay using human mesenchymal stem cells 3A6 and found that they are non-toxic towards 3A6 cells (Fig. 25). Moreover, these hydrogelators are further explored for cell imaging applications and found that these hydrogels **46** and **47** form aggregate in the cytoplasm of 3A6 cells and emit strong blue fluorescence. These results suggest that hydrogels have good biocompatibility and potential applications in cell imaging.
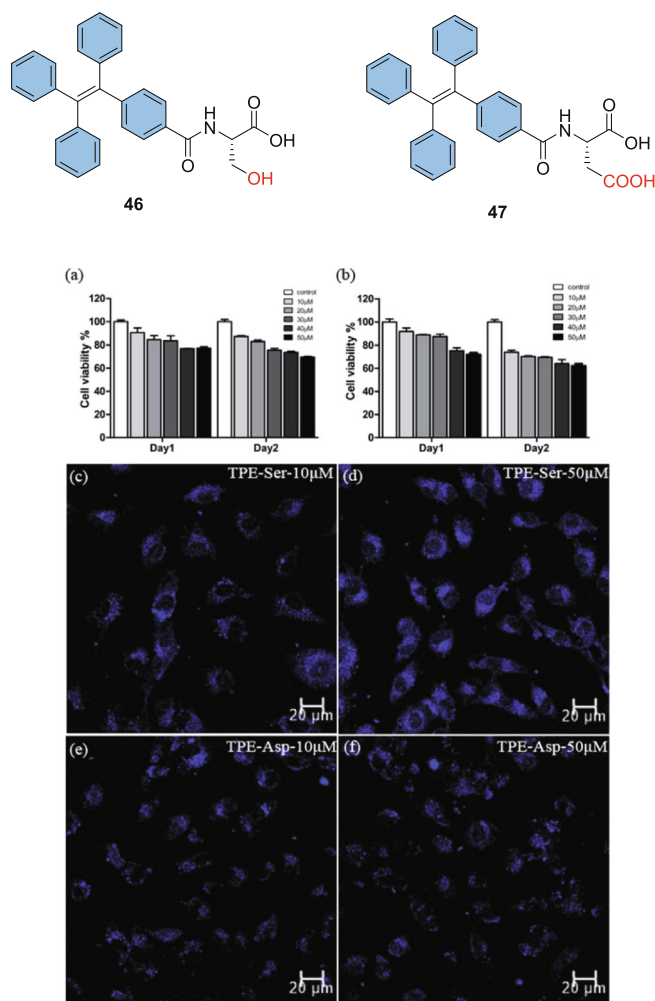

Fig. 25. Structure of hydrogels **46** & **47**. Cell viability of 3A6 cells incubated with 10–50 mM of (a) **46** and (b) **47**; (c & d) Fluorescent images of **46** (various concentrations) treated 3A6 cells; (e & f) Fluorescent images of **47** (various concentrations) treated 3A6 cells. Reproduced with permission from [129]. Copyright 2018 The Royal Society of Chemistry.

A highly emissive conjugated polymer was designed by Sengottuvelu Dineshkumar and co-workers and consists of a donor-π-acceptor structure, poly(*N,N*-diphenyl-4-(4-(1,2,2-triphenylvinyl)styryl)aniline), where triphenylamine as electron donor and TPE as acceptor [130]. In the solid-state, PTPA polymer (**48**) emits strong green emission, where as in THF solution it exhibits weak or non-emissive with small emission intensity at 515 nm. However, the emission intensity slowly increased when the f_w was increased from 0 to 90% which are attributed to AIE characteristics of TPE and TPA (**48**). Afterwards, the mesoporous silica hollow nanosphere surface was modified with PTPA *via* non-covalent bonding to make PTPA loaded MSHNs (**49**) for cellular imaging. Further functionalisation also performed with anti-EpCAM (anti-epithelial cellular adhesion molecule) aptamer via conjugation with γ-glycidoxypropyltrimethoxysilane (GTMS) to yield polymer Apt-PTPA-MSHNs (**51**) (Fig. 26). The PTPA (**48**) polymers, PTPA MSHNs (**49**), and Apt-PTPA-MSHNs (**51**) were evaluated for cytotoxicity against different cancer cells through a standard MTT assay and found that both functionalised polymers are biocompatible towards Huh-7 cells. Moreover, it revealed that aptamer-conjugated PTPA MSHNs (**51**) can efficiently internalize the cell
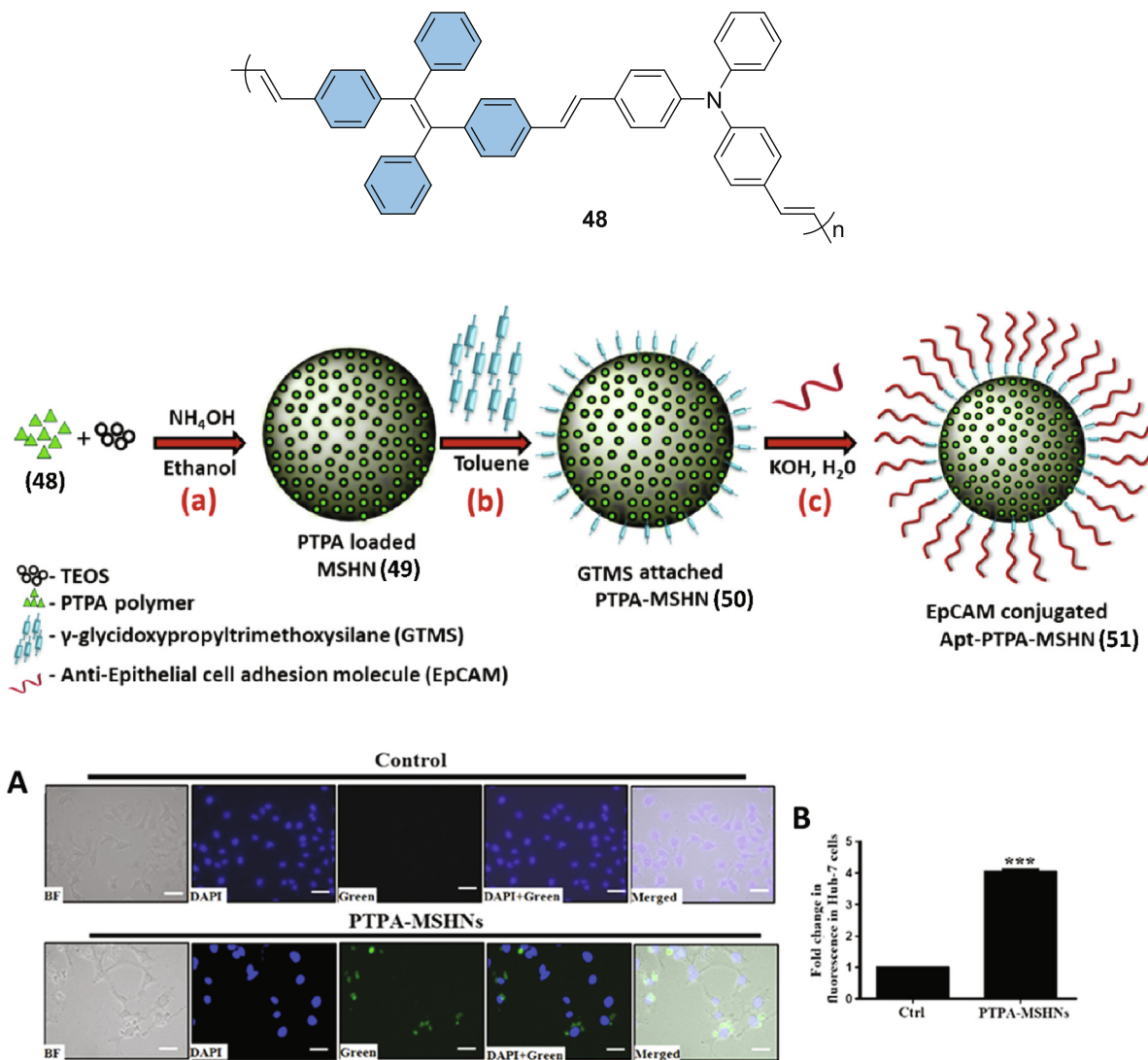
Fig. 26. Structure of PTPA polymer (**48**). (A) Fluorescent images of cells treated with **49**; (B) Fluorescence emitted by Huh-7 cells quantification after treatment with **49**. (concentration of **49** is 100 µg/mL). Reproduced with permission from [130]. Copyright 2019 American Chemical Society.

membrane of the Huh-7 cell and work as promising candidates for bio-imaging applications.

Lei Wang and colleagues [131] synthesised a D-π-A structured near-IR active AIE fluorophore TPE-PTZ-R (**52**), which consists of phenothiazine (PTZ) modified TPE as an electron donor (D) and malononitrile modified rhodanic as strong electron acceptor (A) and studied their photophysical properties. The solvatochromism of as-synthesized fluorophore TPE-PTZ-R (**52**) was investigated in different solvents and found that the emission colour changes from yellow to red in acetonitrile. Further, authors explored the AIE characteristics of the fluorophore TPE-PTZ-R (**52**) in THF/water system and observed a small red shift from 487 nm to 520 nm with increasing the water fraction due to the aggregate formation. The mixture shows a non-emissive property until f_w is 70%, while the fluorescence emission appears above 70% due to the formation of aggregates and its intensity gradually increased up to f_w 99% with a red shift of the wavelength from 640 nm to 654 nm. The above results suggest that the fluorophore TPE-PTZ-R (**52**) exhibit twisted intramolecular charge transfer (TICT) and AIE features. Moreover, to impart the water solubility, the fluorophore **52** was encapsulated with Pluronic F-127 to form TPEPTZ-R NPs (**53**) and were

evaluated for cytotoxicity against HeLa cells and found that the cells are viable (Fig. 27). The fluorophore TPEPTZ-R NPs (**53**) emits red fluorescence with the bioimaging of HeLa cells and are permeable to cell membranes to localize the cytoplasm region. These results suggest that TPEPTZ-R NPs (**53**) is a promising candidate for bioimaging applications.

Coordination cages constructed by trinuclear zirconium clusters possess high stability under different pH conditions, making them a good candidate for *in vitro* bio-imaging. Jinqiao Dong and co-workers [132] have reported two zirconium (IV)-based coordination cages NUS-100 (**54**) and NUS-101 (**55**) (Fig. 28) with AIE characteristics for bio-imaging. HeLa cells imaging in control experiment using NR-cage displayed weaker imaging than NUS100-101, highlighting the benefits of AIE molecular rotors in **54** and **55** for live-cell imaging (Fig. 28a-c).

Qing Lin Guan and co-workers [133] have reported bismuth metal organic framework (Bi-MOF) based Bi-TCBPE **56** (Fig. 29) sensor with "turn off" sensing behaviour towards Fe^{3+} and "turn on" towards cysteine. Bioimaging study of luminescent sensor **56** was performed using hUCMSCs and PC-3 cells (Fig. 29). Most cells are alive with intact morphology with evident blue fluorescence

52

TPE-PTZ-R
52

Pluronic F-127

NPs formation
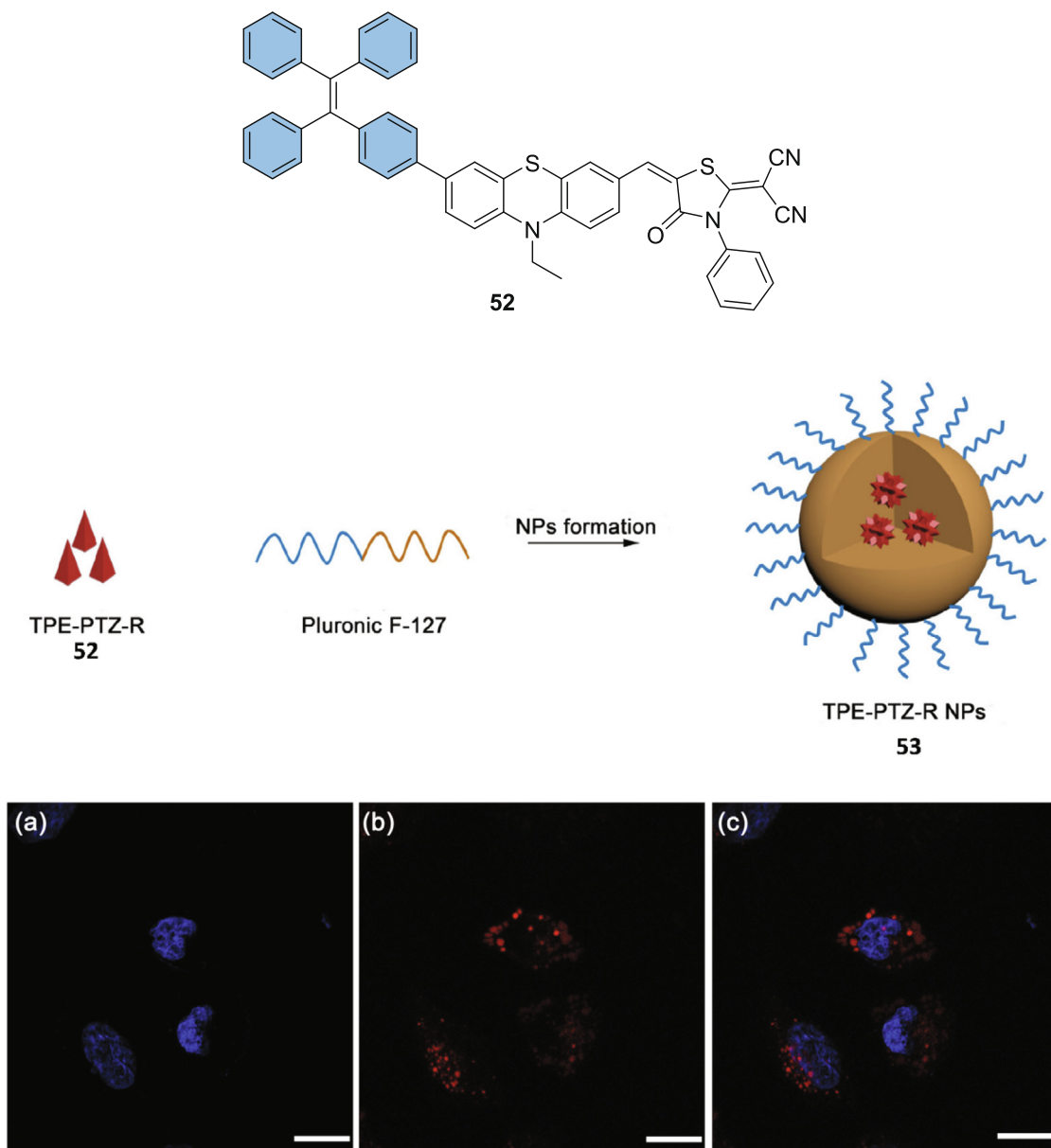
TPE-PTZ-R NPs
53

Fig. 27. Structure of luminogen **52** and fabrication of TPE-PZ-R NPs (**53**). Confocal images of HeLa cells with (a) co-stained with DAPI; (b) co-stained with NPs **53**; (c) merged image. Reproduced with permission from [131]. Copyright 2018 Elsevier.

after stained with **56**, indicating **56** sensor to be a good cell fluorescent dye.

5. TPE based fluorophore for detection and killing of pathogens

Pathogens attack different cells and tissues, and these infectious particles are responsible for various diseases [134]. Pathogens refer to a bacterium (Gram-positive or Gram-negative), virus, protozoa, prion and fungus [135]. Bacterial infection is the prime reason for many diseases, such as dermatosis, sepsis, pneumonia, inflammatory bowel disease and septic arthritis, which are progressively increasing across the world [136]. In recent years, multidrug-resistant (MDR) pathogenic infection possess a serious threat to mankind [137,138]. In view of this, it is worth to develop a new and sensitive tool for detecting and identification of pathogens and to kill bacteria. To overcome these difficulties, many strategies

have been developed for pathogen detection, among them luminogens with AIEgens feature, specifically TPE-based AIEs found to be a powerful tool for turn-on fluorescent sensing. In this section, we are listing few recent reports on a promising TPE based derivatives for identification of drug-resistant bacteria, biosensing, bioimaging of Gram-positive bacteria and as antibacterial agents.

Different strategies with advanced technologies have been used to identify microorganism, MALDI-TOF-MS is one among them. However, these methods suffer from accuracy rate and the fluorescent probe is found to be an alternative and promising tool due to its superior sensitivity. In this direction, Chengcheng Zhou and coworkers [139] have reported, few AIE-active tetraphenylethylene derivatives **57–63** (Fig. 30) to identify pathogens with fast response and superior sensitivity. These derivatives have one positively charged ammonium group along with different hydrophobic substituents to reinforce the hydrophobic and electrostatic
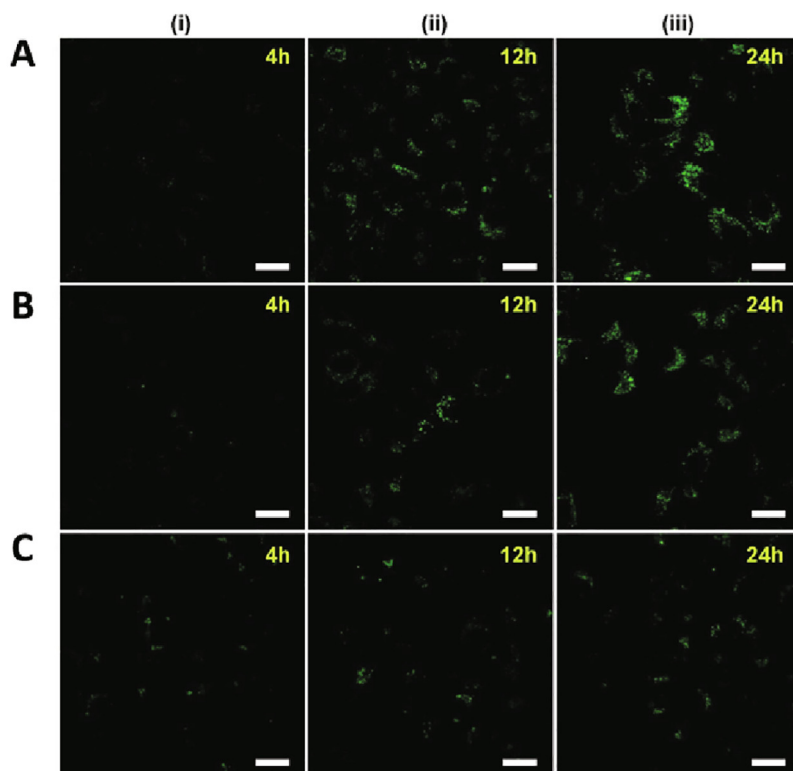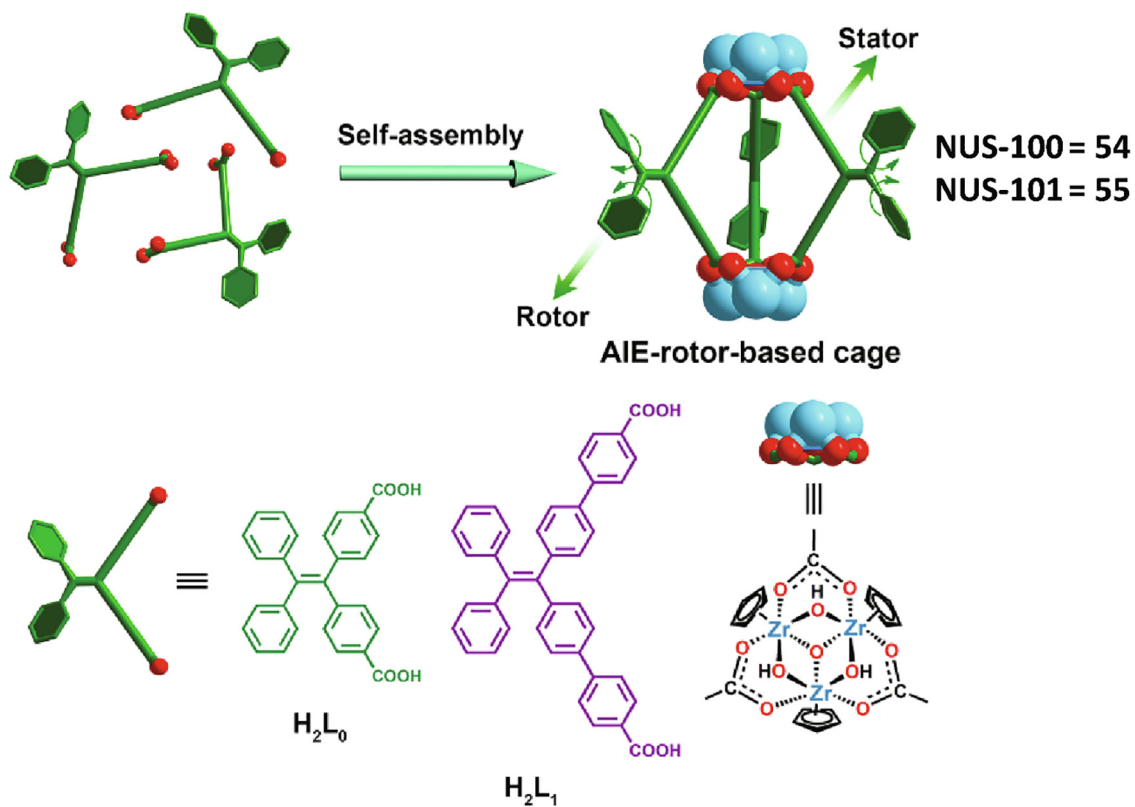
Fig. 28. Schematic representation of self-assembly of Zr based metallocages. The HeLa cell confocal microscopy imaging using (A) **54**; (B) **55** and (C) NR-cage at (i) 4, (ii) 12, and (iii) 24 h incubation. Reproduced with permission from [132]. Copyright 2019 WILEY-VCH Verlag GmbH & Co.
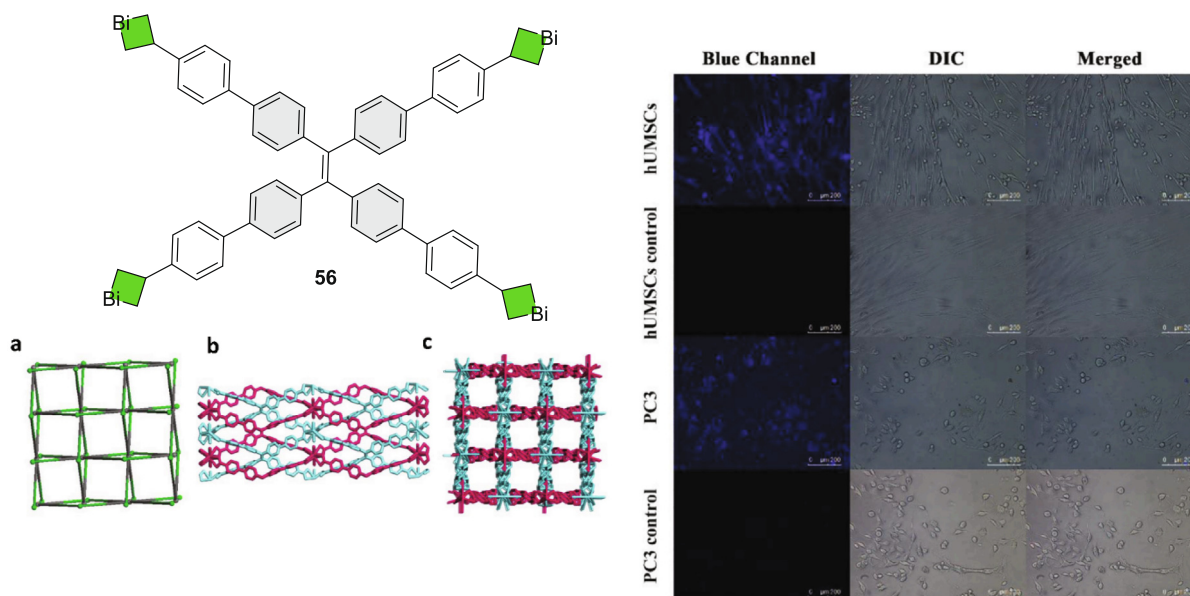
Fig. 29. Structure of **56**. (a–c) Packing framework along the layers of Bi-TCBPE (**56**). Fluorescence microscopy of hUCMSCs and PC-3 cells stained by **56**. Reproduced with permission from [133]. Copyright 2020 Elsevier.

Fig. 30. Structures of **57–63**. (A) Schematic representation of TPE-Ars **59**, **61** and **63** arrays; (B) Confocal images of pathogens with **59**, **61** and **63** (20×10^{-6} M). Reproduced with permission from [139]. Copyright 2018 WILEY-VCH Verlag GmbH & Co.

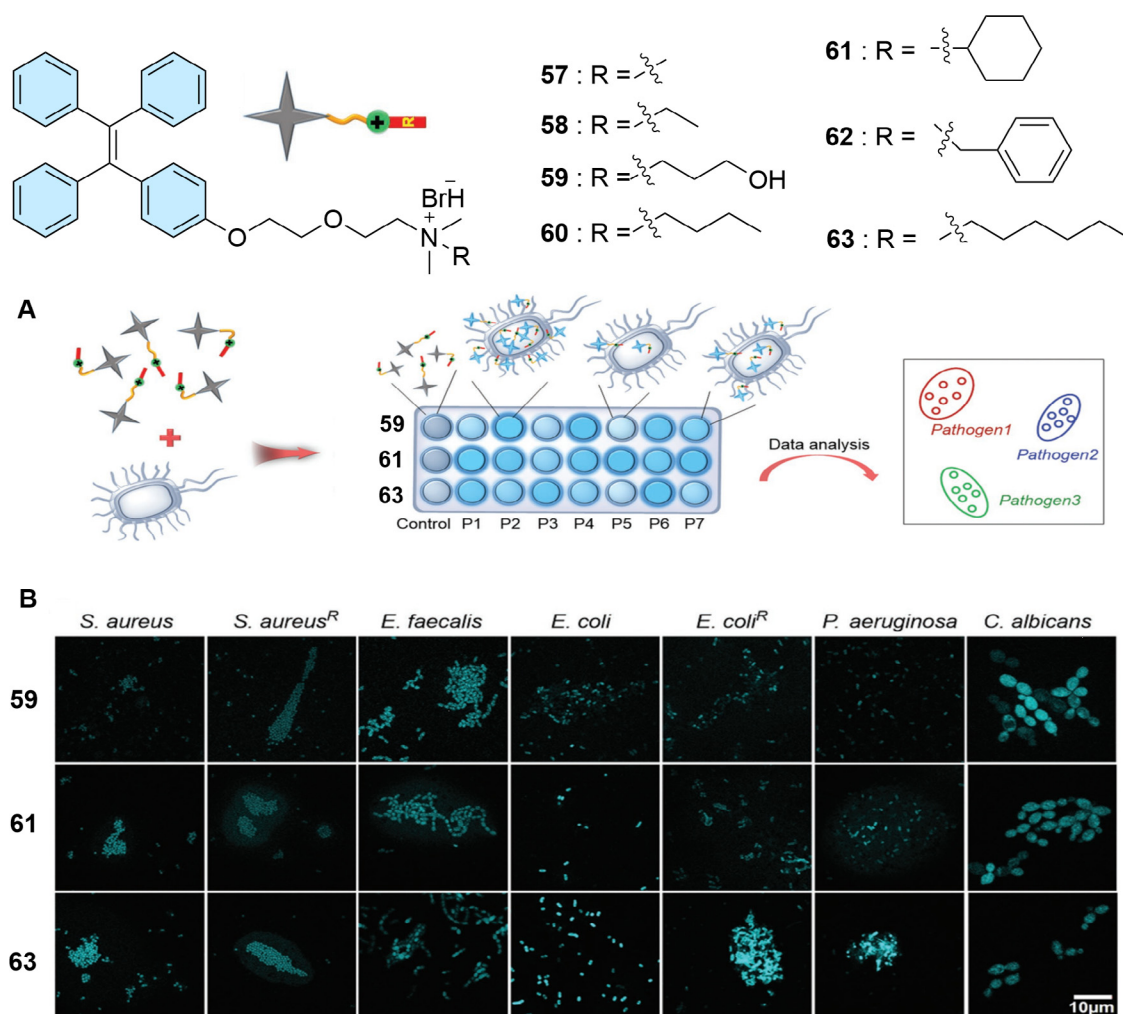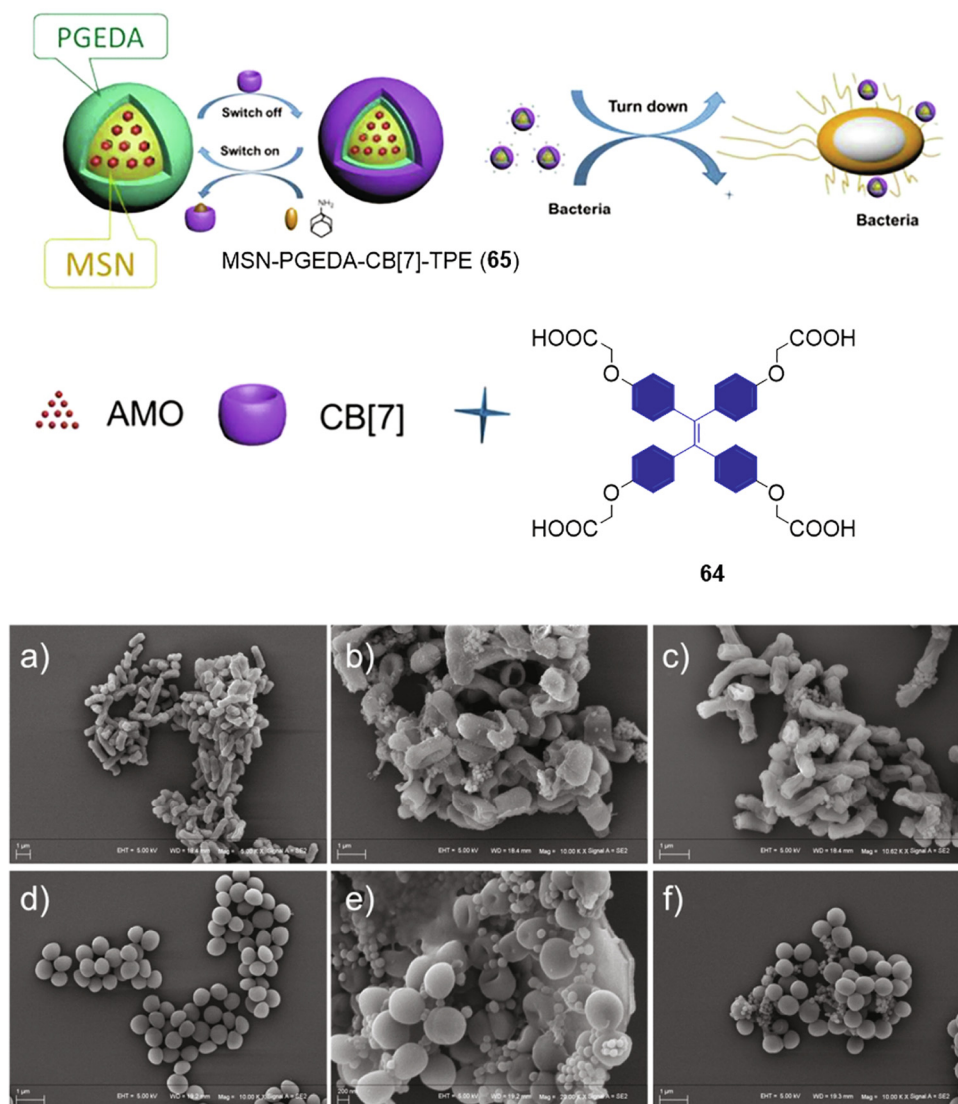**Fig. 31.** Structure of **64** and antimicrobial function of MSN-PGEDA-CB [7]-TPE (**65**) nano-assembly. SEM images of *E. coli* (a, b, and c) and *S. aureus* (d, e, and f) treated with nano-assembly with PBS (a, d) and AD (b, e) respectively; in the absence of AD (c, f). Reproduced with permission from [140]. Copyright 2017 American Chemical Society.

interactions among AIEgens and pathogens. The long alkyl chain helps to improve the hydrophilicity and flexibility of TPE-ARs. Each one of the sensor arrays among fourteen competent arrays tends to pose a different fluorescence response arrangement for different pathogens, due to unique response of TPE-ARs with the pathogens. These sensor arrays are 100% effective in identifying drug-resistant bacteria and they are suitable in multiple pathogens condition.

Detection and developing antimicrobial agents with low cytotoxicity is of prime importance in the present situation. Bisaminated polymer is known to decrease the cytotoxicity of polymers. Qiaoying Li and co-workers [140] have constructed a novel LBL supramolecular nanoassembly of MSN-PGEDA-CB[7]-TPE (**65**) using TPE-based tetracarboxylic acid (**64**) and used these assemblies for the detection of bacteria and as antibacterial agents (Fig. 31). The negative surface of bacteria firmly binds to PGEDA positive surface to form a LBL nano-assembly and losses the AIE activity of TPE, resulting in fluorescence quench. Moreover, the addition of adamantaneamine forms a stable complex by the liberation of PGEDA, which results in the release of AMO that enhances the antibacterial property of nano-assembly. Different experiments

demonstrated that the ability to kill bacteria is controlled by supramolecular dis-assembly process. The SEM images are also suggesting that the antibacterial property of nano-assembly is due to the distortion of the bacterial interacting membrane with disassociated MSN-PGEDA-CB[7]-TPE (**65**). The cytotoxicity of nano-assembly was found to be low in CCK-8 assay.

Viraj G. Naik et al [141] synthesised-TPE based AIE probe for the imaging of Gram-positive bacteria using mono-sulfonate (**66**) and di-sulfonate (**67**) functionalized TPE with long alkoxy chains (Fig. 32). The mechanism explained here is that the positive NH_3^+ group of lipoteichoic acid (LTA) present in the surface of Gram-positive bacteria interacts with SO_3^- group in the probe and turns on the fluorescence of the AIE probe. The Gram-positive bacteria were detected selectively by different fluorimetric studies, whereas the negligible increase in fluorescence intensity was observed for the Gram-negative bacteria in aqueous solution. Moreover, good aqueous solubility and negligible fluorescence make di-sulfonate functionalized TPE probe more suitable for Gram-positive bacterial imaging, helping the imaging process easier and providing more accuracy in quantification without sig-
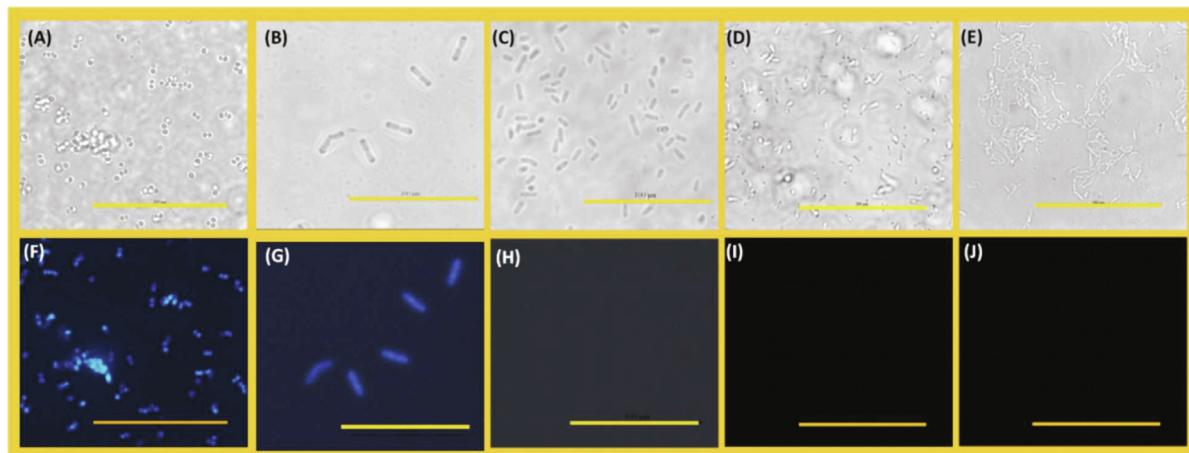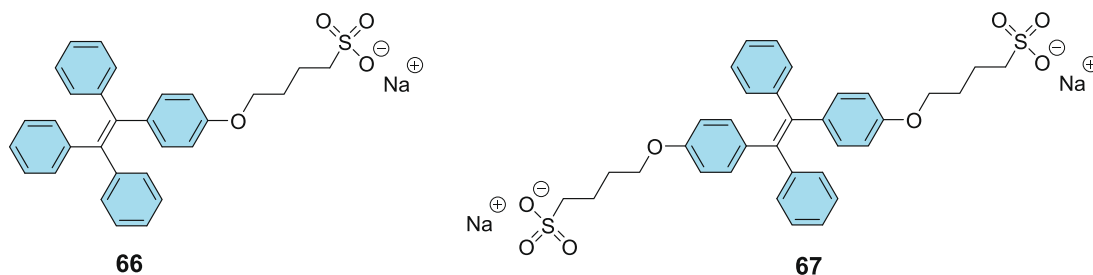
66   **67**

Fig. 32. Structures of **66** and **67**. (A–E) Phase contrast; Fluorescence images of (F) *S. aureus*; (G) *B. subtilis*; (H) *P. aeruginosa*; (I) *E. Coli*; (J) *M. smegmatis* with probe **67** (30 μM). Reproduced with permission from [141]. Copyright 2020 The Royal Society of Chemistry.

nificant loss of bacteria. Di-sulfonate functionalized TPE probe also has antibacterial property against *S. aureus* and the growth kinetics of di-sulfonate probe well matched with kanamycin antibacterial agent.

Biofilm sample detection can be done by various laboratory-based techniques, most of them lack in signal amplification, affecting the efficiency of imaging process. To find an effective solution for this problem, Junxin Aw et al. [142] reported a covalently linked cephalosporin structure (class C AmpCBla enzyme sensitive reporter molecule) with TPE moiety (**68** and **69**) which helps in detection of drug-resistant pathogens in biofilms. AIE characteristics of TPE make this molecule to be a good candidate for biosensing and bioimaging (Fig. 33), unlike the other fluorophores quench the fluorescence in the aggregation. Achievement of selective recognition towards Class C Bla is attributed to the bulky methoxy-imino group on cephalosporin ring. The selective localization of fluorescent labelling greatly helps in the monitoring of biofilm formation, providing valuable information for the better treatment against bacterial infections.

Fang Hu and colleagues [143] developed TPEPy-D-Ala (**70**) as a dual-functional probe with D-alanine and a photosensitizer based bacteria-metabolizable for turn-on fluorescence imaging of hidden intracellular bacteria and photodynamic ablation in situ. The incorporation of probe into bacterial peptidoglycan improves fluorescent signals to provide better visualization of the intracellular bacteria. On the other hand, ligations of TPEPy-D-Ala (**70**) to peptidoglycan effectively can ablate the labelled intracellular bacteria in situ, with MIC of 20 ± 0.5 μg/mL (Fig. 34). This low MIC value suggests that the TPEPy-D-Ala (**70**) is more efficient than the standard antibiotic, vancomycin.

6. TPE-based probes for cancer diagnosis

Currently, cancer is a serious threat to humans and causes severe mortalities worldwide. Among them, many reports pointing that the top threat in the world continues to be breast cancer [144]. In human cancer treatment, chemotherapy is a commonly used method and found to be an effective therapy, and most of the chemotherapeutics are based on small molecules [145,146]. These therapeutics based on small molecules exhibit several disadvantages in clinical trials due to their low solubility, less bioavailability and poor cancer specificity that restrict their application in cancer therapy. Nanomedicine is found to be a great alternative to small molecule therapeutics for cancer treatment [147]. Compared with conventional hydrophobic organic molecule-based drugs, drug-loaded nanocarriers possess better stability and specificity in biological conditions. Further, researchers continued their effort to provide better alternatives to overcome the drawbacks of chemotherapy, mainly by early diagnosis, therapy before cancer metastasis and imaging-guided drug delivery.

The advancement of fluorescence bioprobes with AIEgens serves as an excellent agent to monitor biological process [148] and disease theranostics [149], whereas commonly used nanoparticles fluorogenic experience low quantum yields due to their ACQ property. Till date only few research groups have focused on developing redox-responsive AIE bioconjugate NPs for targeted cancer therapy. Ling Yang and co-workers [150] are among them who have designed and synthesized redox-responsive AIE bioconjugate nanoparticles (**72**) consisting of disulfide bond to target the suppression of cancer cells (Fig. 35). The nanoparticle bioprobe contains chitosan polymer chain linked to a greater number of TPE
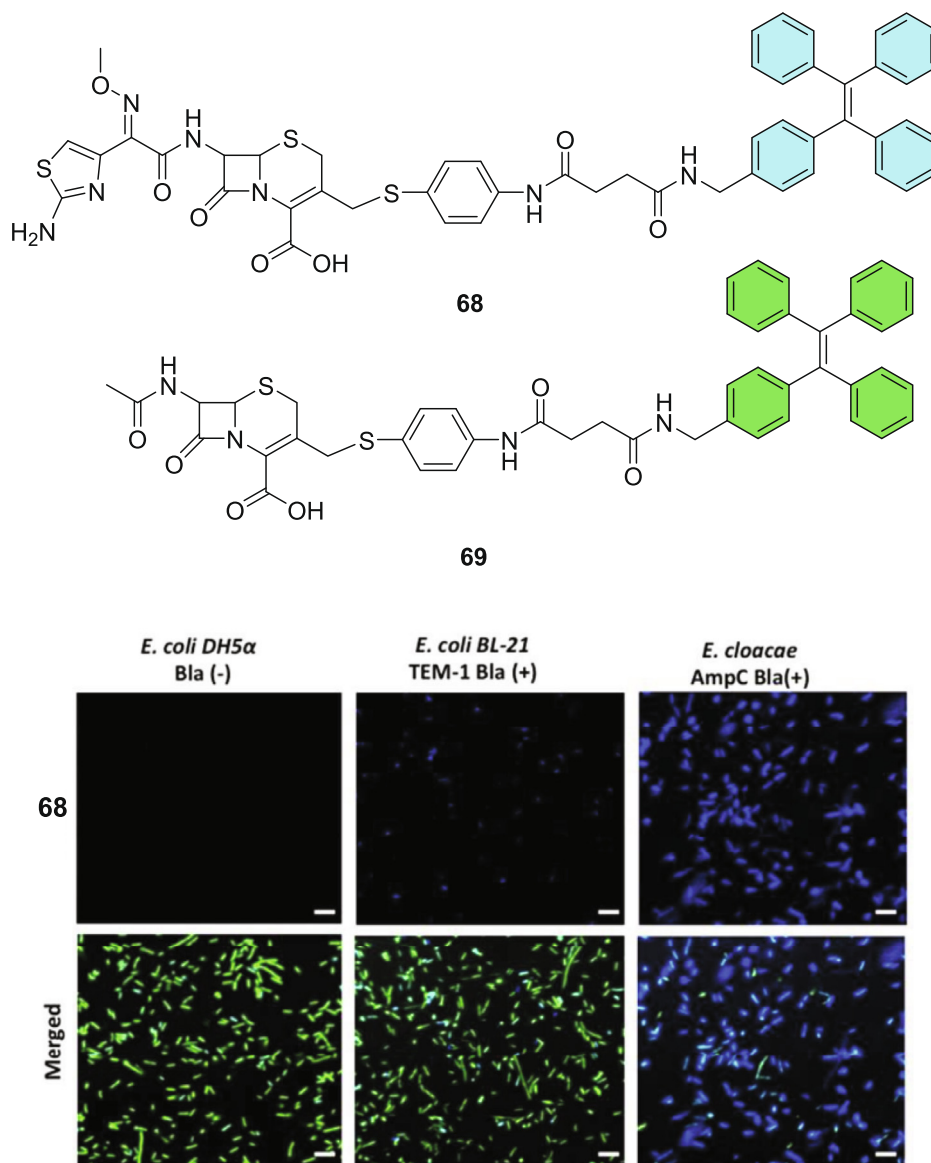
Fig. 33. Structures of **68** and **69**. Confocal imaging of different bacterial strains with 20 μM of **68** in 0.1 M PBS. Reproduced with permission from [142]. Copyright 2020 The Royal Society of Chemistry.

units and disulfide attached carboxylic acid groups (**71**). In physiological condition, these nanoparticle bioprobes exhibit excellent water dispersibility and dispersive fluorescent emission. The disulfide bond is easily cleavable and consequently losses the carboxylic group which results in the aggregation of TPE-chitosan. This aggregation increases the retention of nanoparticle intracellularly and elevates the emission brightness. The aggregation-enhanced retention process helps to trace the biological fate of the cancer cells. Flow cytometry experiment suggests that TCSC NPs (**72**) induce apoptosis of HeLa cells and result in their necrosis. It is clear that these nanoparticle bioprobes can be employed for selective inhibition of cancer cells and for targeted cancer cell imaging reinforcement. Even though it is a superior agent to monitor the biological process, its blue-emitting fluorescent system restricts *in vivo* imaging, which can be overcome by developing red-emitting AIE bioconjugates.

Tianyu Li and co-workers [151] developed selenium-comprising of AIEgen to support the combined treatment of

chemotherapy and radiotherapy to combat cancer. Since diselenide bonds are sensitive to γ-radiation, authors have included TPE into the diselenide system to achieve AIE property. Upon gamma irradiation, diselenide bonds break to seleninic acid, inducing a high level of ROS generation and subsequent cytotoxicity against cancer cells. Both compounds **73** and **74** showed anticancer activities against breast and lung cancer cells under γ-radiation explored by CCK-8 assay. Breast cancer cells itself showed a mild fluorescence, but there is an increased fluorescence intensity upon irradiation of γ-rays suggesting the production of ROS in water, which is confirmed by DCFH-DA assay and CLSM inspection (Fig. 36). Further, increased fluorescence intensity of the cells treated with compound **73** is attributed to the selenic acid formation upon γ-radiation and the flow cytometry analysis results demonstrate that the γ-radiation promoted the high ROS level in cancer cells. These results showed that the combination therapy of selenium-based nanomedicine may advance the cancer treatment efficiency.
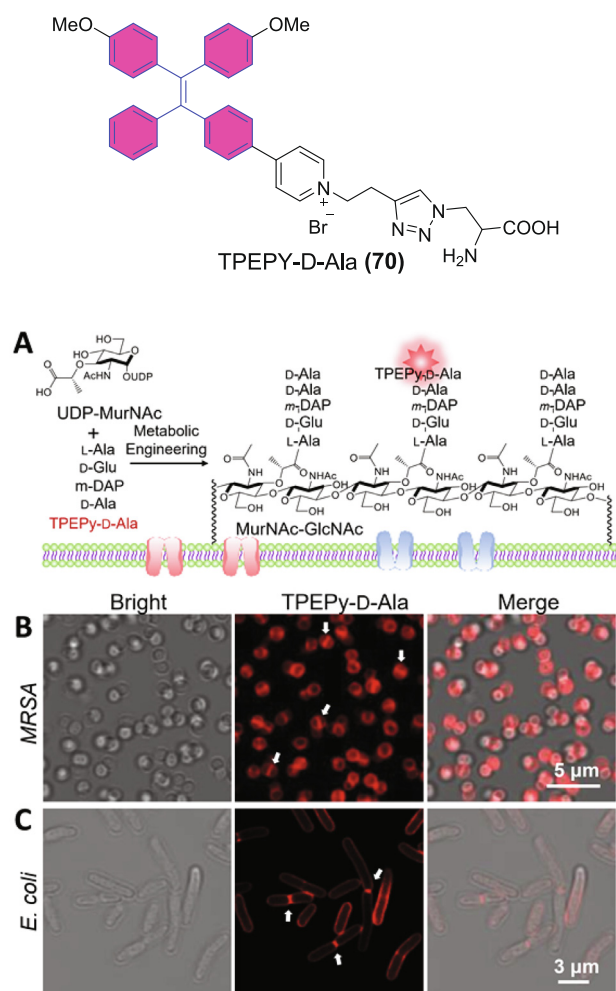
TPEPY-D-Ala (70)

Fig. 34. Structure of **70**. (A) Schematic illustration of **70** fluorescence. Confocal image of (A) MRSA and (B) *E. coli* (C) cells treated with **70** for 20 min. Reproduced with permission from [143]. Copyright 2019 WILEY-VCH Verlag GmbH & Co.

Cancer cell targeting ability can be improved through bio-orthogonal reaction with high selectivity. The reaction performed in a biological system without harming the normal physiological process with reliability and selectivity called bio-orthogonal reaction. Pengfei Zhang et al. [152] have employed this strategy to develop polyyne-bridged AIEgens, 2TPE-4E (**75**) and embedded into DBCO-PEG-lipids to create AIE dots (**76**) to target cancer *via* complementing metabolic engineering and bio-orthogonal chemical reaction. 2TPE-4E (**75**) consists of two *N, N*-diethyl substituted TPE derivatives on both the ends of polyyne having D-π-A structure. This polyyne bridge increases the conjugation, resulting in the bathochromic shift and restricts the emission quenching. The examination of cell labelling and bio-orthogonal efficiency of AIE dots were found to be fruitful in MCF-7 cancer cells *in vitro* (Fig. 37). Authors have also developed an *in vivo* metabolic labelling approach for delivering AIE dots specifically to tumor and targeting imaging. Bio-orthogonal chemical reaction considered as an important technique for bioprobes to use in biological substrate labelling in living system.

Ziyu Wang and co-authors [153] reported self-illuminating drug carriers using AIE-active probes by altering electron donor in the donor–acceptor (D-A) assembly for antitumor treatment structures. By varying the electron donor groups, the fluorescence behaviour of polymers **77**, **78** and **79** could interconvert between AIE and ACQ. Apart from its self-illuminating ability, these polymer dots along with paclitaxel (an anticancer drug) had a better biocompatibility and *in vivo* anticancer property compared to Taxol (Fig. 38). Authors have provided an effective method for producing multicoloured AIEgen drug carriers.

7. TPE-based bio probes for photodynamic therapy

Photodynamic therapy (PDT) is employed to kill cells under visible light irradiation based on photosensitizers (PSs) which can produce ROS [154,155]. So far, various photosensitizers including porphyrin, BODIPY, nanocrystals, and many more have been reported in the literature with near-infrared (NIR) emission [156–159]. However, most of the fluorophores are hydrophobic in nature quenched from ACQ effect, leading to a decrease in generation of ROS and the fluorescence intensity greatly reduced in the aggregated state due to discotic structures [160,161]. Thus, the development of AIE PSs has intensified fluorescence by absorption and emission and negligible toxicity as well as good biocompatibility in the (nano) aggregated form is highly promising.

Wenbo Wu and co-workers [162] designed and synthesized D-A'-π-A type AIE photosensitizers **80**–**85** (AIE PSs) in which methoxy substituted TPE exerts electron-donating property and dicyanovinyl (DC) group as an electron acceptor and benzene as π spacer between D-A substituents (Donor-Acceptor) and benzothiazole as auxiliary acceptor. The benzothiazole group in D-A'-π-A structure serves as π spacer for the facile separation of HOMO and LUMO energy gap between S_1 and T_1 state and favours ROS generation. Due to poor solubility of AIE PSs (**80**–**85**) in water, AIE PS were encapsulated with DSPE-PEG$_{2000}$ to form AIE PS NPs **80**–**85**. The synthesized AIE PS NPs **80**–**85** were explored for $^1O_2$ generation and found that in bright far-red (FR) and NIR emission AIE PS NPs **84** and **85** were effective for $^1O_2$ generation and improving absorption (Fig. 39). Subsequently, both AIE PS NPs **84** & **85** show high level of ROS production against MDA-MB-231 cells with dichlorofluoresceindiacetate (DCFDA) as ROS sensor under white light irradiation (Fig. 39). Further, synthesized AIE PS NPs **84** and **85** showed low IC$_{50}$ (<1.0 µg/mL) confirming that AIE PS NPs display low cytotoxicity and generate more $^1O_2$ species to inhibit MDA-MB-231 cells under PDT treatment. Thus, AIE PS NPs **84** and **85** are promising candidates for image-guided PDT and open new opportunities in clinical applications.

Jianjiao Chen et al. [163] synthesised dimerized TPE derivative BTPE (**86**) as photosensitizer with AIE properties for PDT. The biphenyl TPE dimer BTPE (**86**) was synthesized by Suzuki-coupling reaction which was encapsulated with DSPE-PEG$_{2000}$ to form BTPE NPs (**86**) by nano-precipitation method. The as-synthesized BTPE NPs (**86**) are further investigated for AIE characteristics and found that with enhanced water fraction in THF/water, the fluorescence intensity gradually increased due to the accumulation of aggregates. From the TEM image, it was found that the self-assembled BTPE NPs (**86**) display a mean diameter of approximately 70 nm. The authors have further explored BTPE NPs (**86**) for singlet oxygen generation ability under visible-light illumination using SOSG as a singlet oxygen sensor and confirm that BTPE NPs (**86**) generate more $^1O_2$ than that of monomer TPE ones which are crucial for PDT. Subsequently, authors have explored the generation of ROS using DCF-DA as ROS sensor and found that **86** is capable of generating ROS in a highly efficient manner which were observed under CSLM (Fig. 40). To further evaluate phototoxicity of BTPE NPs (**86**) standard MTT assay were carried out against HeLa cells and found that NPs show IC$_{50}$ of 8.4 µg mL^{-1} which is better than monomer TPE NPs. An *in vivo* experiment suggests that **86** under light irradiation can suppress tumor proliferation. From these results, it was found that BTPE
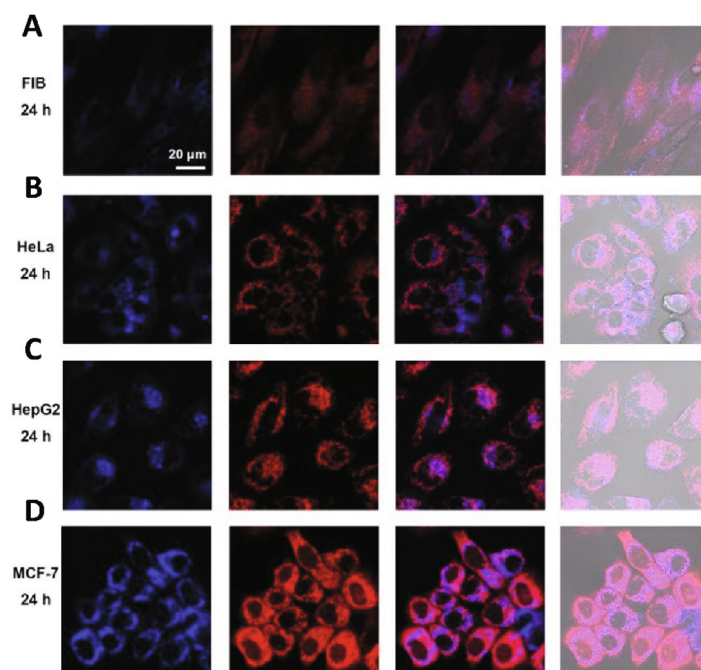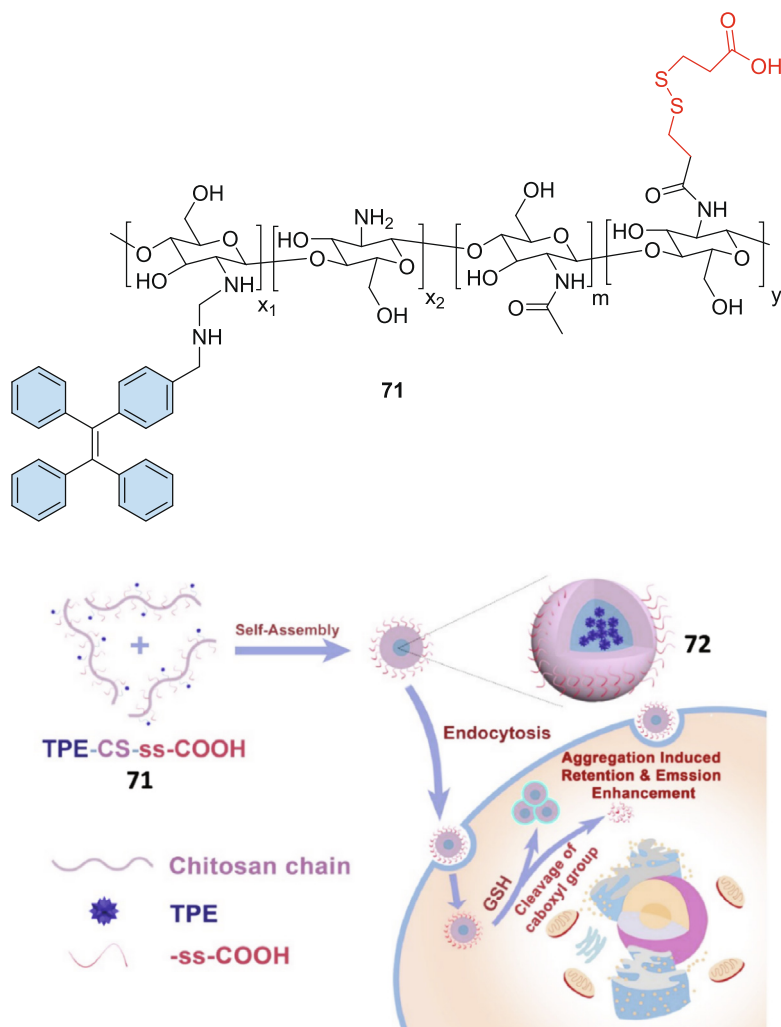
Fig. 35. Structures of **71** and **72**. (A–D) Confocal images of various cells (FIB, HeLa, HepG2, MCF-7) stained by NPs **72** (0.1 mg mL^{-1}) and Mito Tracker Red CMSRos for localization of **72**. Blue first column for **72** particles; Red second column for mitochondria; Third column is merged fluorescent channels; Fourth column corresponds to bright field images. Reproduced with permission from [150]. Copyright 2019 The Royal Society of Chemistry.
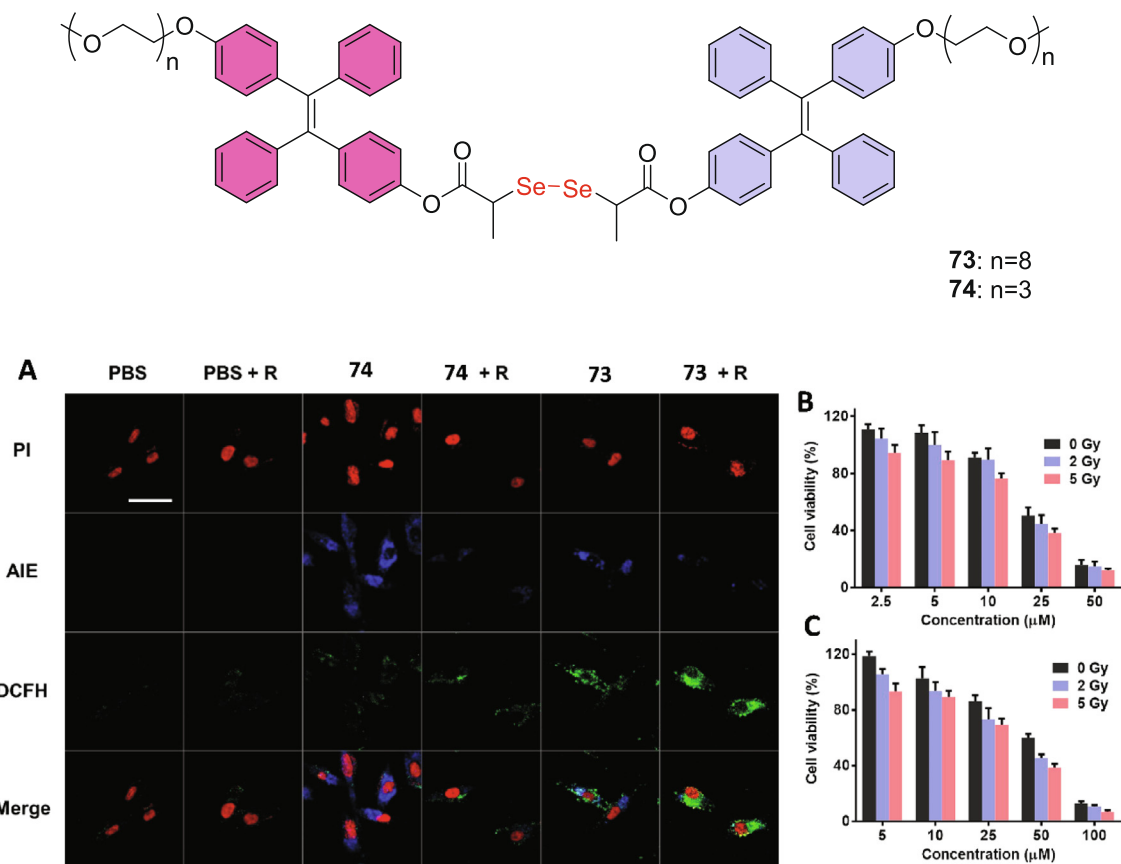
73: n=8
74: n=3

Fig. 36. Structure of polymers **73** and **74**. (A) CLSM pictures exhibiting both AIE fluorescence and ROS levels; (B-C) Anticancer activity of **73** & **74** under gamma-radiation against MDA-MB-231 cells. Reproduced with permission from [151]. Copyright 2020 American Chemical Society.

NPs (**86**) show high phototoxicity, low cytotoxicity and good biocompatibility as superior candidates for *in vivo* applications under PDT effect.

C. Parthiban and co-researchers [164] synthesised a TPE-based visible-light triggered fluorescent nanoparticles (TPE-*p*HP-Cbl NPs) (**87**) using *p*-hydroxy phenacyl chlorambucil (*p*HP-Cbl) for chemo-photodynamic therapy (Fig. 41). The as-synthesized tetraphenylene substituted-*p*-hydroxyphenacyl-chlorambucil (TPE-*p*HP-Cbl) was subsequently synthesized to form TPE-*p*HP-Cbl NPs (**87**) with mean diameter of ~8 nm by reprecipitation method. The *in vitro* study was performed to monitor drug release by **87** in HeLa cells. A yellow fluorescence appeared in the HeLa cells after incubation of **87** for 8 h owing to cellular uptake of **87** (Fig. 41b). Light green fluorescence (Fig. 41c) appeared after irradiation of light for 3 min suggesting the partial decomposition of **87** and complete fluorescence colour change was noticed after 5 min of light irradiation, revealing the release of drug by **87** inside the cells (Fig. 41d). These results suggest that **87** is a promising fluorescent nanoparticle for real time cellular imaging with synergistic effect (combination therapy). The high fluorescent intensity of **87** is attributed to its AIE characteristics. Exposure of **87** to light simultaneously generate singlet oxygen and stimulated drug release. Besides, released photoproduct can enhance production of singlet oxygen. Further, the cytotoxicity studies were carried out for TPE-*p*HP-Cbl NPs (**87**) by standard MTT assay against HeLa cells and normal cell line (HaCaT cell) by irradiating visible light, and cells are found to be viable and nontoxic which are attributed due to PDT and chemotherapeutic effect.

Parthiban and co-researchers [165] have also reported TPE-based light-responsive fluorescent organic nanoparticles (TPE

(Cbl)$_4$ (**88**) for PDT using aggregation-induced-emission process. TPE(Cbl)$_4$ conjugate is synthesized by AlCl$_3$ catalysed acylation of TPE using bromoacetyl bromide followed by the reaction with chlorambucil (Cbl). Different experimental results disclosed that TPE(Cbl)$_4$ NPs are spherical with diameter of approximately 42 nm. Hence, these drug-loaded nanoparticles can efficiently penetrate into tumor cells and due to the decreased lymphatic drainage, they are retained in the tumor bed. This process is called enhanced permeability and retention effect. The drug release capability of TPE(Cbl)$_4$ NPs with visible-light exposure was monitored using HPLC and fluorescence and the obtained data suggested that 96% of the drug release was achieved after 25 min of irradiation. The light and dark experiments revealed that the light is necessary to release drug from the NPs (Fig. 42). In addition, the high-resolution mass spectrometry analysis points that the release of 4 equivalent of the antitumor compound (cbl) from the nanosystem is sequential rather simultaneous in their aggregated state. The cytotoxicity of TPE(Cbl)$_4$ NPs verified by MTT assay on HeLa cell lines exhibit promising antitumor property owing to the drug release and PDT activity.

Sijia Gao et al. [166] have revealed that organoplatinum (II) metallacycle possesses AIE property and acts as a photosensitizer. It self-assembles with tobacco mosaic virus coat protein, which is decorated with a *trans*-acting activator of transduction (TAT) peptide through electrostatic interactions **89–93** (Fig. 43). The transition element platinum helps ISC from a singlet to triplet state to mediate ROS production and this assembly exhibits strong membrane-intercalating ability due to self-assembly of negatively charged protein moiety with the positively charged organoplatinum (II) metallacycle. This ROS generation from the photosensi-
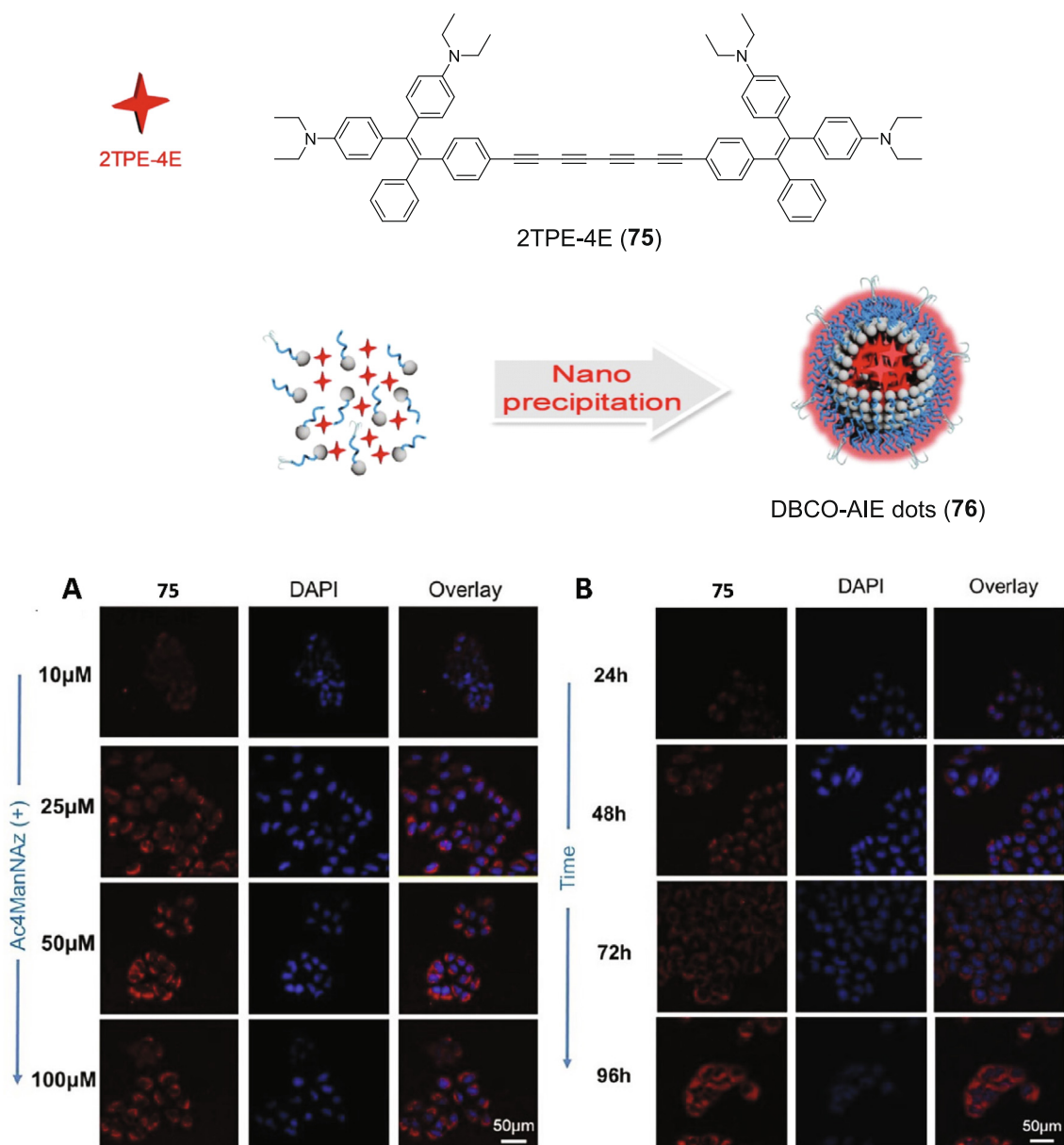
2TPE-4E (**75**)

DBCO-AIE dots (**76**)

Fig. 37. Structures of **75** and DBCO-AIE dots (**76**). (A) Standardization of Ac4ManNAz and CLSM images of Ac4ManNAz treated (3 days) MCF-7 cells with further incubation with **76** (30 min); (B) *in vitro* optimization of Ac4ManNAz incubation time for metabolic labelling of the MCF-7 cells. Reproduced with permission from [152]. Copyright 2019 WILEY-VCH Verlag GmbH & Co.

tizer by the light activation and membrane-intercalation can potentially enhance the photodynamic inactivation (PDI) efficiency against bacteria. The PDI efficiency is found to be much better and selective against Gram-negative bacteria. The morphology examination by SEM and TEM after irradiation reveal that the possible antibacterial mechanism is due to the membrane lysis by ROS. This membrane-intercalation-enhanced PDI behaviour of this assembly can be selectively used as a promising candidate for PDI in Gram-negative bacteria elimination.

Wenbo Wu and co-workers [167] have reported new AIE photosensitizers of TBT (**94**) having aggregation-induced NIR emission centred at 810 nm and under white light irradiation showed high singlet oxygen generation efficiency. Further substitution of two long-chain branched alkyl groups to TBT avoids the strong interactions in the solid state for TBTC8 (**95**) and NPs also show band at

810 nm with good singlet oxygen generation efficiency. The effect of PDT was examined in 4T1 cancer cell *in vitro* incubated with TBTC8 NPs which showed excellent cell imaging ability (Fig. 44). Authors have further explored the capability of TBTC8 NPs in *in vivo* tumor therapy. These results indicate better *in vivo* tumor imaging function of TBTC8 NPs.

AIEgens in aggregated state with efficient emission and ROS production are superior photosensitizers for fluorescence guided photodynamic therapy (FL-PDT) than traditional photosensitizers used in PDT. The tumors demonstrate high viability in hypoxic condition due to enhanced levels of H_2O_2 and lipid droplet (LD) accumulation. Consequently, development of LD-targeted, H_2O_2 activatable AIE-active photosensitizer for FL-PDT is of great interest. AIE active amphiphilic TPECNPB probe **96** (Fig. 45) is fabricated with positively charged pyridinium pendent with boronate ester
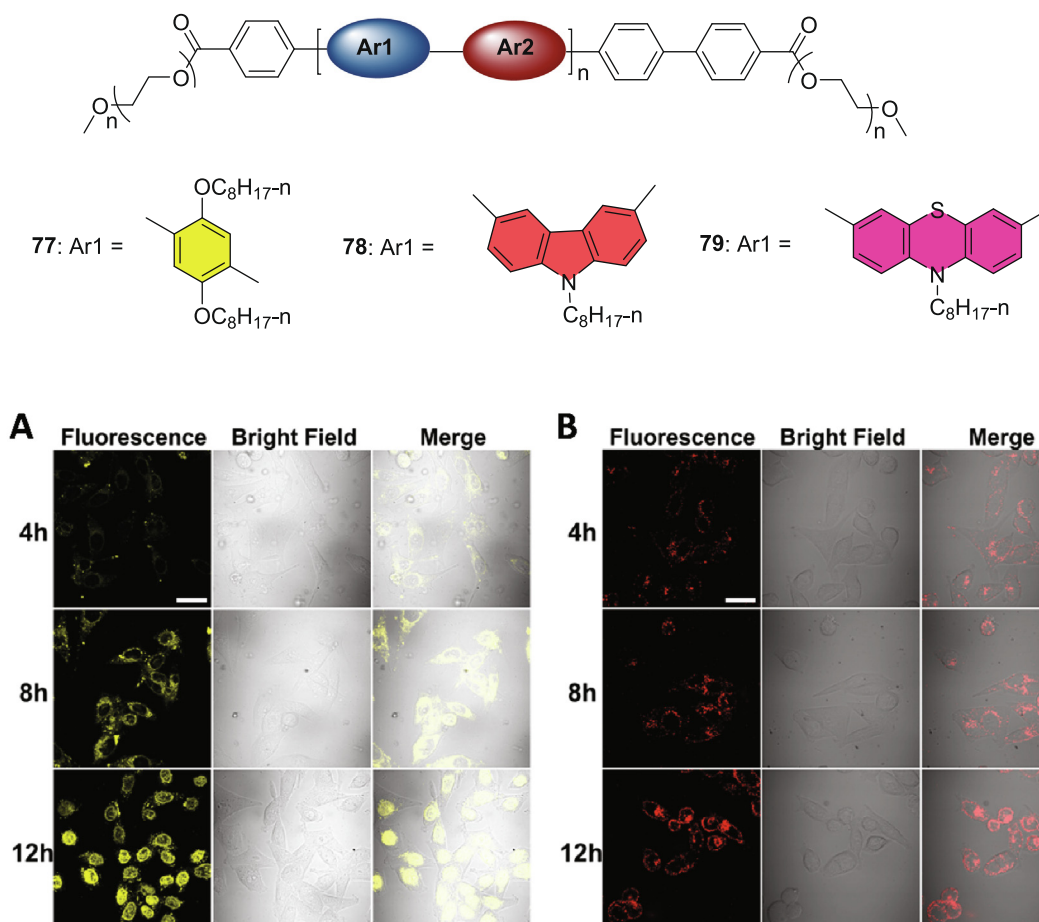
Fig. 38. Structure of polymers 77–79. (A) Cellular imaging of PTX-loaded **77** dots and (B) **78** dots in MCF-7 cells. Reproduced with permission from [153]. Copyright 2020 American Chemical Society.

(H_2O_2 activatable site) to target negatively charged LD *via* electrostatic attraction [168]. Absorption and PL spectra of probe TPECNPB **96** revealed the large stoke shift (175 nm) and exhibited excellent photo stability. Probe **96** can accumulate selectively in LD and undergoes activation by endogenous H_2O_2 for light-up bioimaging in live MCF-7 cells (Fig. 45). PDT induced cell apoptosis of MCF-7 cells was observed after treating with H_2O_2-activated TPECNPB. This probe would be a great addition for both real-time monitoring and PDT of tumors.

8. TPE-based probes for drug and gene delivery

Tumor therapy and diagnostics using smart nanostructures possess various advantages over biomolecules and small molecule drugs [169]. Delivering drugs specifically to tumors is the basic need in cancer therapy and the nanoparticles have this capability *via* EPR effect, that reduces the drug side effects [170,171]. Recently, great interest has been shown to multifunctional nanocarriers due to its progressive effects on cancer therapy [172]. The integration of fluorescent tracing molecule and drugs with theranostic nanoparticles have shown improved efficacy in cancer treatment [173]. The drug-releasing ability of carriers would greatly influence the efficacy of drug that help for developing a drug delivery strategy. As it is known, the fluorescence emission intensity diminishes for most of the organic luminophores due to ACQ effect, which significantly impedes the bioimaging effect as

well [174]. To avoid these undesired ACQ effects, AIE fluorophores have been successfully employed for cancer treatment and imaging-guided drug delivery [175]. The advantage of the AIE nanoaggregates is that they can sustain in the live cells for longer time without losing fluorescence intensity for long term tracing of the cells [176]. Still, it is a demanding task to co-ordinate the interaction of the nano-carriers with biological system for cancer therapy *in vivo*. Therefore, designing a suitable nano-carrier for controllable drug transport and specific delivery targeting the tumor sites demands a lot of attention from researchers.

Fang Hu and co-workers [177] have synthesized dual-prodrug by the reaction of Mitomycin C (MMC) and TPE substituted with mono vinyl pyridine (TPEPY) photosensitizer (PS) *via* a disulfide link that can activate the chemo-prodrug TPEPY-S-MMC (**98**). Aggregated state of TPEPY has high ROS generation efficiency but TPEPY-S-MMC (**98**) has quinine component that exerts a quenching effect in MMC moiety, affecting the ROS generation. 4T1, HeLa cancer cells and 293T normal cells were used to assess the cytotoxicity and for living cell imaging of TPEPY-S-MMC (Fig. 46). These images suggest that the intracellular GSH concentration is highly responsible for activation of TPEPY-S-MMC (**98**) and showed good selectivity to cancer cells over normal cells. Upon white light irradiation, TPEPY-S-MMC (**98**) and DCF-DA (2′,7′-dichlorofluorescein diacetate) treated 4T1 and HeLa cells were highly emissive, while poor green fluorescence was displayed for cells pre-treated with buthionine sulfoximine (BSO, GSH inhibitor) confirming that the intracellular activation was not undertaken by GSH. More interest-
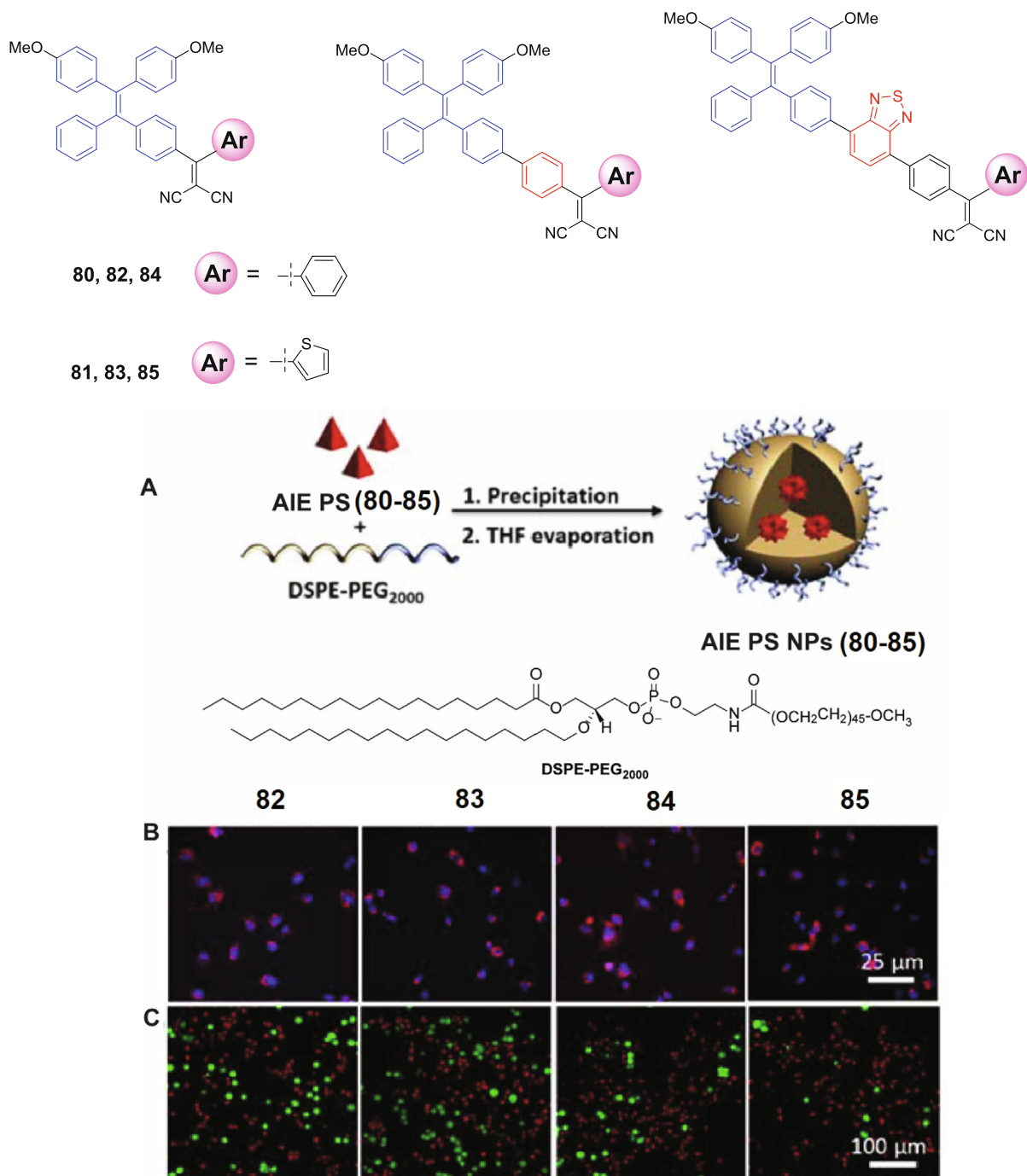
80, 82, 84 Ar = phenyl

81, 83, 85 Ar = thiophene

Fig. 39. Structures of AIE PS (**80–85**). (A) scheme of AIE PS NPs (**80–85**); (B) Confocal images of **80–85** NPs incubated MDA-MB-231 cells with 5 μg/mL concentration; (C) Live/dead staining of **82–85** NPs treated MDA-MB-231 cells. Reproduced with permission from [162]. Copyright 2017 The Royal Society of Chemistry.

ingly, the control probe TPEPY-C-MMC (**99**) after treating with 4T1 and HeLa cells does not show neither red fluorescence from PS nor green fluorescence from emissive DCF due to non-cleavable C–C linker. The C.I analysis confirms that the combined delivery of MMC and TPEPY-SH as a prodrug in TPEPY-S-MMC (**98**) results in an increased tumor killing ability with minimal damage to normal tissues, restoring of red fluorescence indicates the drug releasing from the TPEPY-SH.

Tian-Tian Wang and co-workers [178] prepared doxorubicin-loaded polyethylene glycol-block-peptide (FFKY)-block-tetraphenylethylene (PEG-Pep-TPE/DOX) NP's (**100**) and D-peptide to dynamically detect the drug release as shown in Fig. 47. FRET imaging being useful to study the release of drug molecules from nanoparticle; authors have attempted three different methods for quantitative detection of the release and circulation of the nanomedicine in A549 cells. All the above-mentioned analyses suggest that under *in vitro* laboratory condition, peptide NP's **100** were highly sensitive to recognize drug release in cells. MTT assays of free DOX, PEG-Pep-TPE NPs and **100** against A549 cells suggest that self-assembled peptide with doxorubicin is favoured for the inhibition of cancer cell proliferation with undesired side effects.
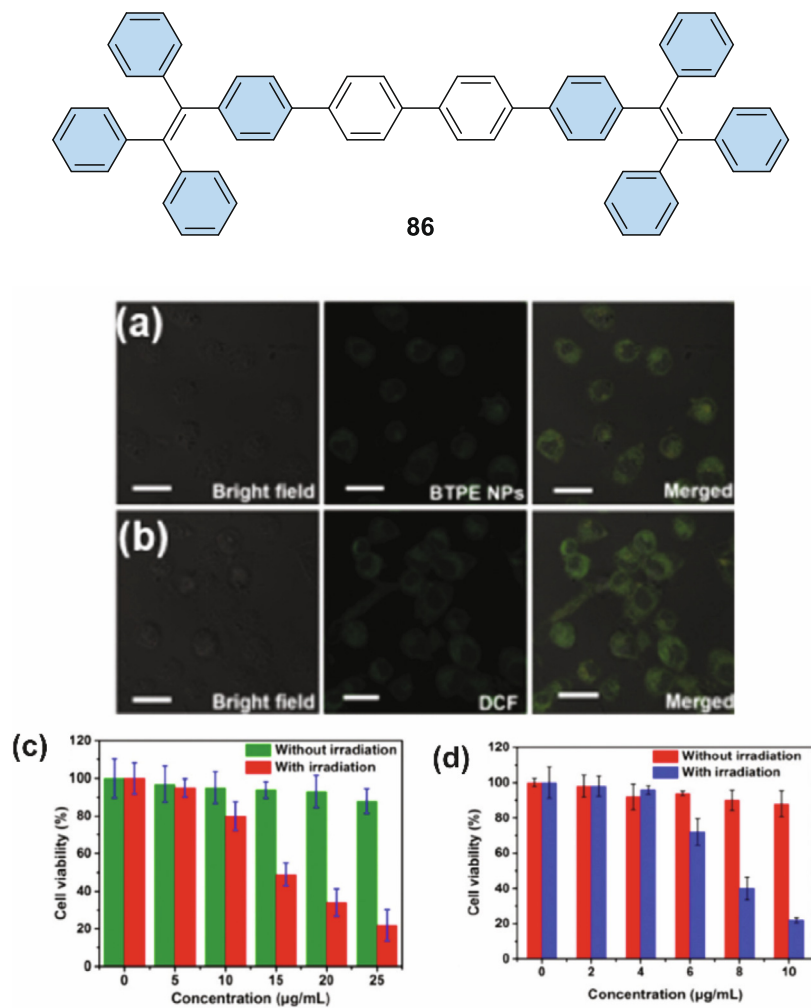
86

Fig. 40. Structure of **86**. (a) Internalization of **86** NPs in HeLa cells; (b) ROS generation of **86** NPs with DCF-DA; (c) MTT assay of TPE NPs on HeLa cells; (d) MTT assay of **86** NPs on HeLa cells. Reproduced with permission from [163]. Copyright 2020 Centre National de la Recherche Scientifique (CNRS) and The Royal Society of Chemistry.
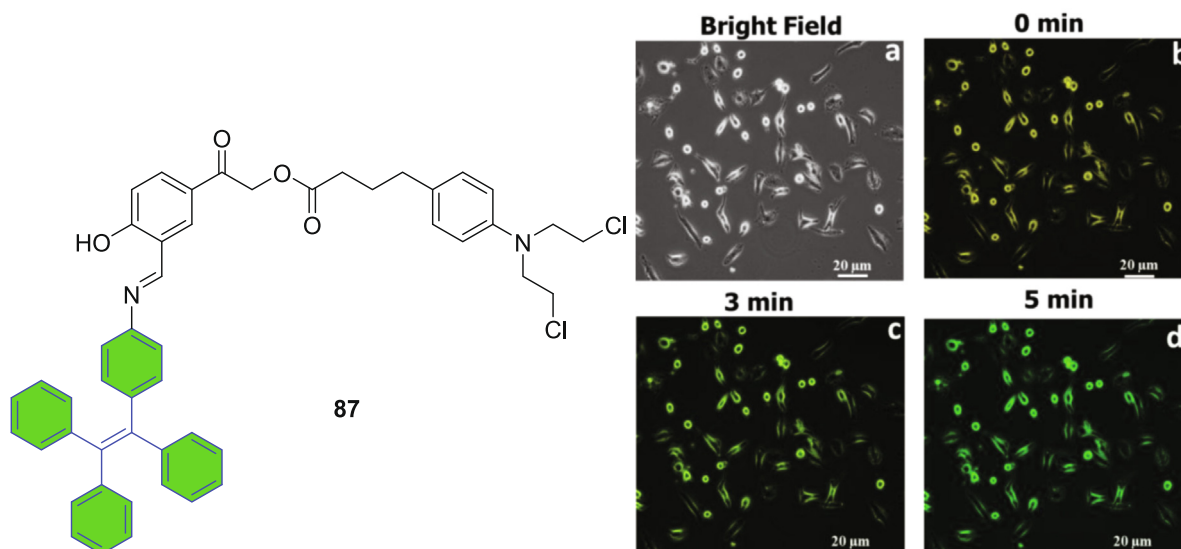

87

Fig. 41. Structure of **87**. (a) Confocal bright-field image of HeLa cells and (b-d) upon light irradiation at various time intervals. Reproduced with permission from [164]. Copyright 2018 American Chemical Society.
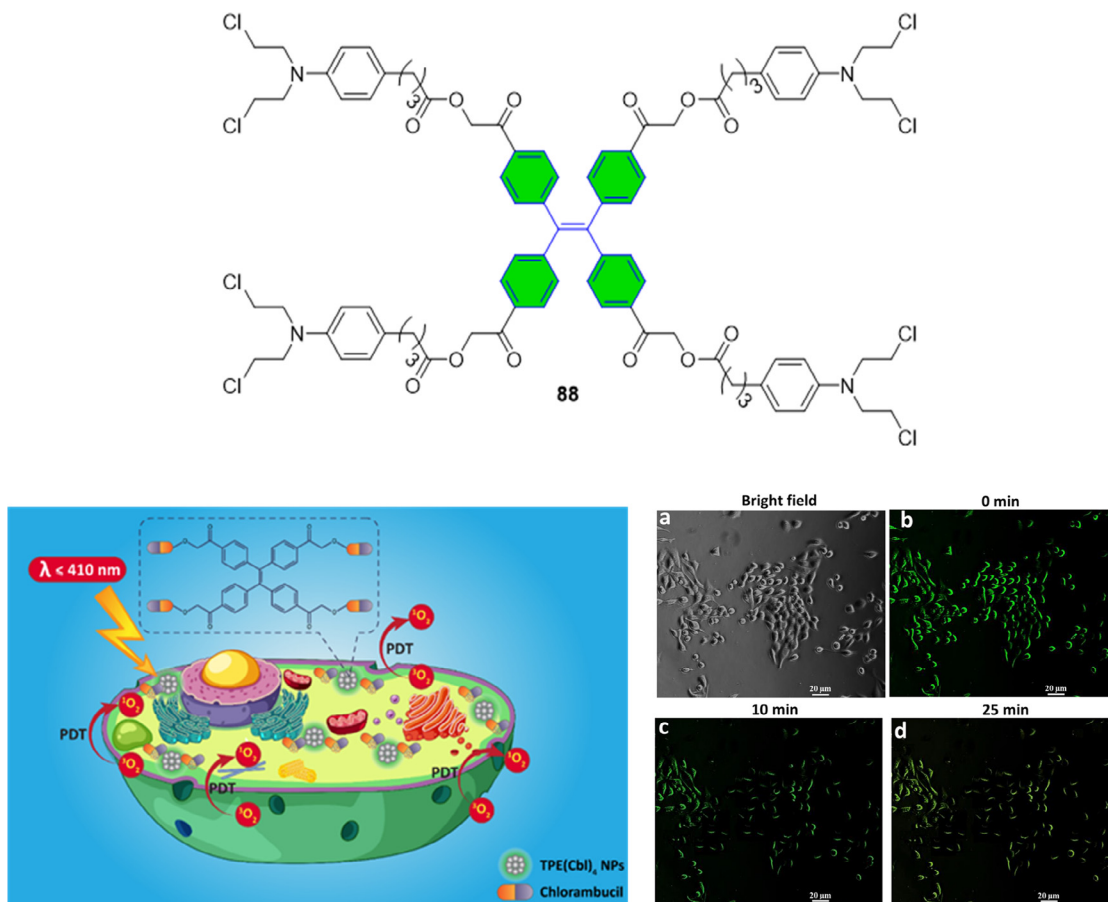
Fig. 42. Structure of **88** and Schematic illustration of fluorescent nanoparticles **88** for chemo-photodynamic therapy under visible light. Formation of reactive oxygen using **88** by HeLa cell stained with DCFDA (a) bright field and (b) 0, (c) 10, and (d) 25 min of light irradiation. Reproduced with permission from [165]. Copyright 2019 American Chemical Society.
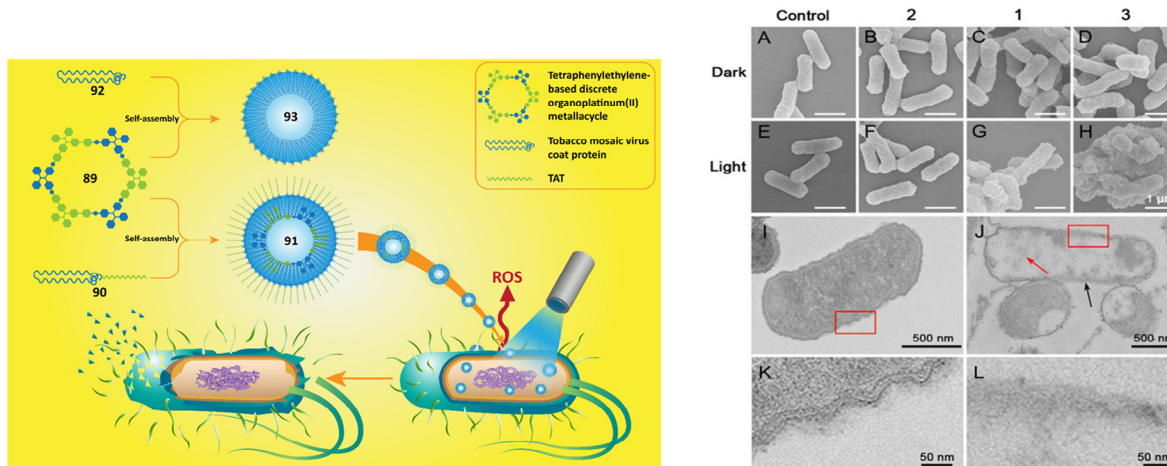

Fig. 43. Representing the self-assembly of metallacycle **89** and protein **90**; Mechanism of action of **91**; Self-assembly of metallacycle **89** and protein **92**. (A–H) SEM images of *E. coli* cells; (I and J) TEM images of *E. coli*; K and L are enlarged images. Reproduced with permission from [166]. Copyright (copyright year) National Academy of Sciences.
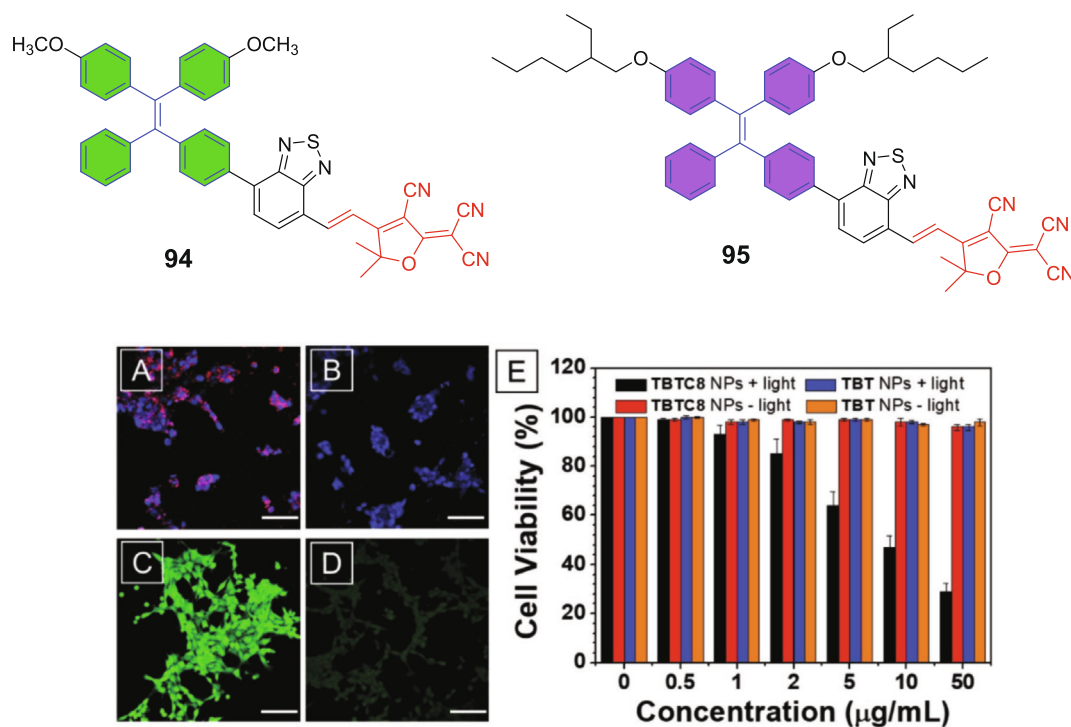
Fig. 44. Structure of photosensitizers **94**–**95**. Confocal fluorescent images of 4T1 cancer cells after incubated with (A) **95** NPs or (B) **94** NPs for 12 h. ROS generation with (C) **95** NPs or (D) **94** NPs loaded 4T1 cells. (E) Cell viability of **95** treated 4T1 cells. Reproduced with permission from [167]. Copyright 2019 WILEY-VCH Verlag GmbH & Co.

Ziyu Wang et al. [179] prepared two new AIE-active conjugated polymers (**101** and **102**) *via* Suzuki coupling polymerization reaction with colour tunable activity by changing their intramolecular FRET pairs. These conjugated polymers have been used to carry drugs for self-indicated therapy for cancer (Fig. 48). The studies reveal that exact location can be detected when using these the two polymers as drug carriers with a model drug paclitaxel (PTX) due to their different AIE characteristics. The biocompatibility of **101** and **102** were assessed on LO2 cells by MTT assay and both the CPNs showed low cytotoxicity and preferable biocompatibility. The *in vitro* anticancer ability was analysed for PTX loaded CPNs and PTX on HeLa and A549 cancer cell lines, where the PTX loaded CPNs show sustained release property with slightly lowered cytotoxicity on both Hela and A549 cells.

Chi Zhang and co-researchers [180] integrated a chimeric peptide comprised doxorubicin (DOX) to overcome tumor MDR (Fig. 49). This transformable chimeric peptide forms packed cell networks *via* morphological changes for cell encapsulation, controlling drug efflux and reversing tumor MDR. The chimeric peptide CTGP (**103**) (C_{16}-K(TPE)-GGGH-GFLGK-PEG$_8$) initially formed nano micelle assemblies to create a peptide-based nanosystem DOX (CTGP@DOX (**104**) by encapsulating the anticancer agent for drug delivery. The release of the drug by the addition of cathepsin B is controlled by the disassociation of CTGP@DOX (**104**), which is further confirmed by fluorescence spectroscopic kinetic studies. Further confocal studies revealed that the weak fluorescence from CTGP and DOX are due to FRET and ACQ effect, whereas CTGP@DOX (**104**) exhibit high intensities of blue and red emission after incubating with cathepsin B. Different biological experiments

have showed that CTGP@DOX (**104**) could be separated by cathepsin B-overexpressed MCF-7S (drug-sensitive) and MCF-7R (drug-resistant) cells (Fig. 49). Further rearrangements to nanofibers on the cell membranes restrict the DOX efflux. The CTGP@DOX (**104**) showed a long-term blood circulation than free DOX, high anti-MDR capacity and better anticancer effects in *in vivo* test.

Yixia Qian et al. [181] have attempted for accurate tumor targeting therapy, *in vivo* imaging and apoptosis monitoring by an advanced micellar delivery system (STD-NM) (**106**). This STD-NM system were functionalised with peptides (ST and TD) and an AIE. The purpose of AIE molecule TPE (**105**) is to show the 'switch on' fluorescence during apoptosis. ST in the peptide is constituted of pH-controlled targeting peptide STP (sequence: SKDEEWHKNNFPLSPG) and TD is a tumor acidity-activated peptide, which is essential for the nanocarrier to keep it in good functionality under normal conditions. Both the peptides enhance the cell permeability and cell penetration of the activated STD-NM (**106**). *In vivo* imaging assays of NIR fluorescent dye 1,1-dioctade cyl-3,3,3,3-tetramethylindotricarbocyanine iodide encapsulated STD-NM (**106**) on HT-29 xenografted mouse model suggests that the nanocarrier STD-NM (**106**) specifically targets and penetrate to deeper tumour site and sense the tumor cell (Fig. 50). *In vivo* therapeutic results indicate that the peptide performs better in combined form than the single function of ST and TD. Furthermore, authors have investigated therapeutic effects on genetic level using RNA-sequencing technique and the supervised Gene Ontology (GO) experiments.

Xiangdong Xue and colleagues [182] have attempted to generate a self-indicating drug delivery system (SIDDS), having ability
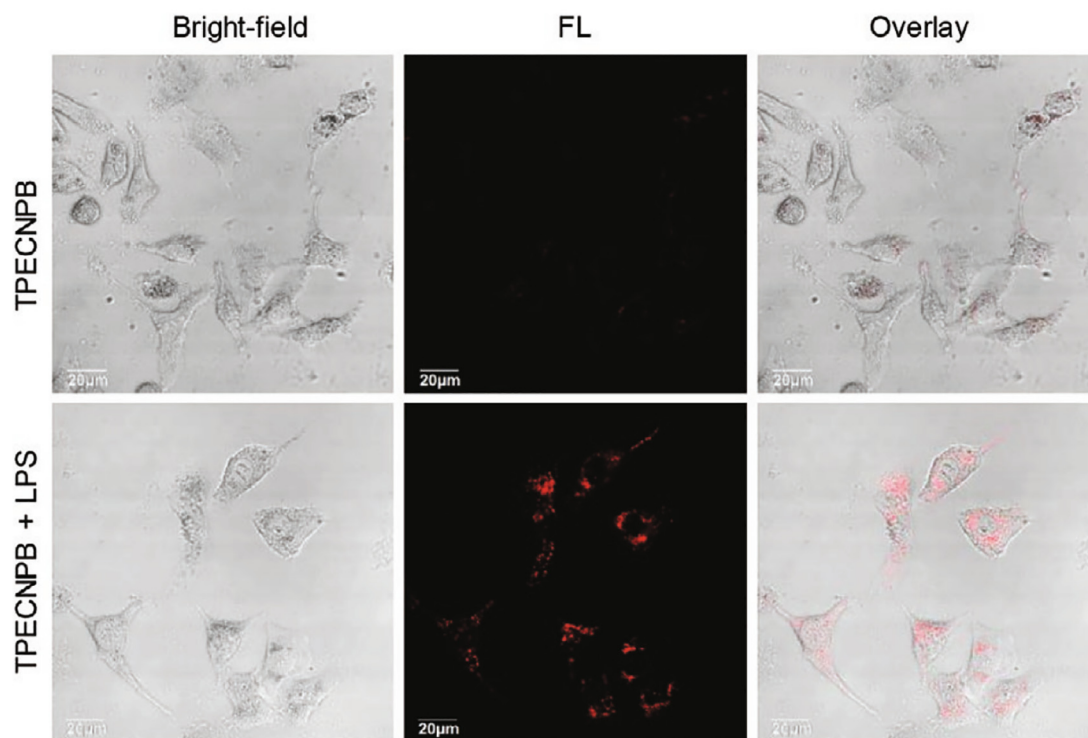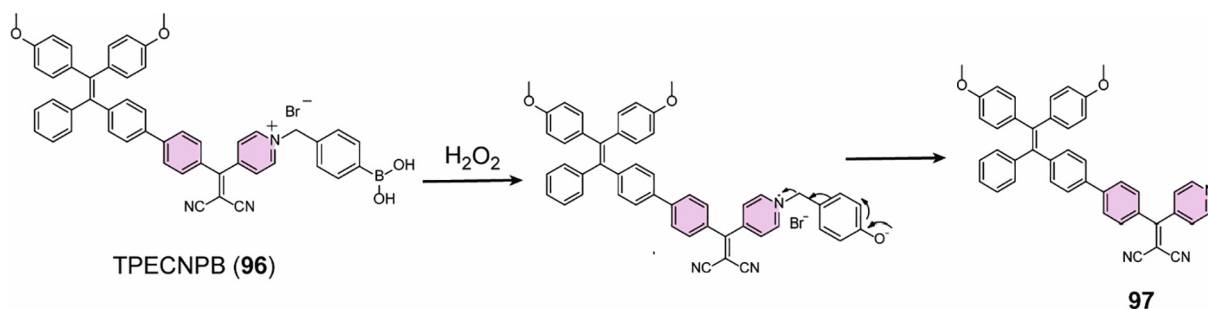
Fig. 45. Structures of fluorescent probe **96 & 97**. Confocal laser scanning microscopy (CLSM) images of MCF-7 cells incubated with **96** with or without lipopolysaccharide. Reproduced with permission from [168]. Copyright 2020 WILEY-VCH Verlag GmbH & Co.

of revealing spatiotemporal drug release (**108**). TPE derivative (**105**) assembled to self-luminescent nanoparticles to show AIE which can be easily tracked inside the cell. The formed TPE NPs (**107**) have superior activity compared to conventional drug delivery system without showing ACQ effect and exhibited low cytotoxicity and good biocompatibility. Further, TPE NPs (**107**), free DOX, and TD NPs (**108**) were incubated with MCF-7 cells to examine at sub-cellular level (Fig. 51). The study reveals that TPE NPs were traceable in the cytoplasm but not in the nucleus, that the fluorescence of TPE (**105**) was weaker than TPE NPs (**107**) due TD NPs (**108**) quenching and co-localization of DOX suggests some of DOX and TPE still aggregates as TD NPs (**108**) when they are taken into cells and further, the sub-cellular level of TPE NPs (**107**) and DOX can be determined when they come in contact together and shows high FL intensity. This suggests SIDDS could be a promising drug delivery system, which determined the subcellular location of the delivery system along with the improved therapeutic effect.

Qing-Lan Li and coresearchers [183] have constructed new multifunctional drug delivery system by modifying per-6-thio-β-

cyclodextrin (CD) entities on copper sulfide (CuS) through ligand exchange to form CD-CuS nanoparticles. In further, the CD-CuS nanoparticles attached onto benzimidazole-grafted fluorescent TPE-functionalized mesoporous silica nanoparticles **110** (FMSN) to integrate FMSN@CuS, a pH stimuli-responsive controlled drug delivery system (CDDS) (Fig. 52). Anticancer drug DOX moieties are loaded into FMSN@CuS, eventually CD-CuS at physiological pH (7.4) displayed zero prerelease of anticancer drug DOX and also on-demand DOX release at an acidic pH attributed to the pH-responsive gate-opening of CD-CuS under acidic pH. In further, DOX-loaded FMSN@CuS **112** enhances the fluorescence intensity upon release of drug, which is useful phenomenon to track the intracellular drug release event depending on the variation of luminescence intensity. Interestingly, DOX-loaded FMSN@CuS demonstrated a very good synergistic effect upon 808 nm laser irradiation against cancer cell line SGC-7901 via enhanced chemotherapy and photothermal therapy (Fig. 52A & B).

Development of safe and efficient vectors is the basic criteria for successful gene therapy [184], and the major challenges for
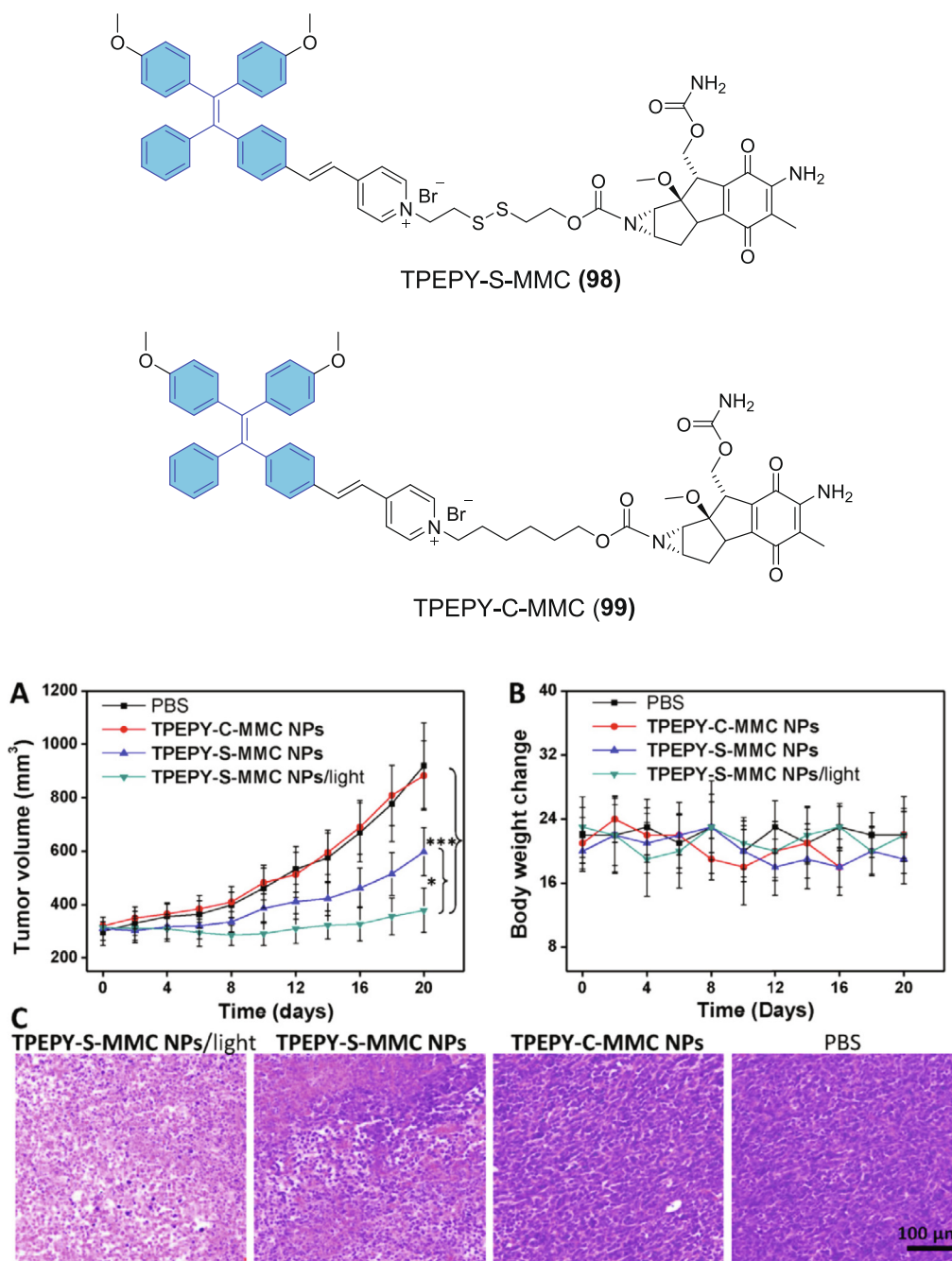
TPEPY-S-MMC (98)

TPEPY-C-MMC (99)

Fig. 46. Structures of 98 and 99. (A) Tumor volume measurement after intratumoral administration with PBS, 99 NPs and 98 NPs along with or without white light irradiation; (B) Body weight change for all mice during the treatment period; (C) H&E staining for tumor at day 5 after treatments. Reproduced with permission from [177]. Copyright 2017 Elsevier.

effectual gene delivery are endo/lysosomal escape of gene vectors and subsequent nucleic acids unpacking in cytosol. To address these issues, Youyong Yuan and coworkers [185] have developed light controlled and ROS-responsive polymeric gene delivery vector (Fig. 53) comprising of TPE based AIE photosensitizers (PSs) coupled with oligoethylenimine (OEI) (800 Da) using aminoacrylate (AA) linker 113 (Fig. 53). Low molecular weight OEIs are advantageous as arms over polyethyleneimine (PEI) due to its

effective DNA binding ability and lower toxicity. The aqueous solubility of the polymer is drastically improved upon grafting with PEG and helps to self-assemble into nanoparticles in water media. The prepared polymer can easily bind to DNA via electrostatic interactions 114 (Fig. 53). The generated ROS upon light irradiation helps vectors to escape through membranes disruption from endo/lysosomes. Parallelly the polymer breaks down to smaller sized components by ROS, leading to unpacking of DNA. This method
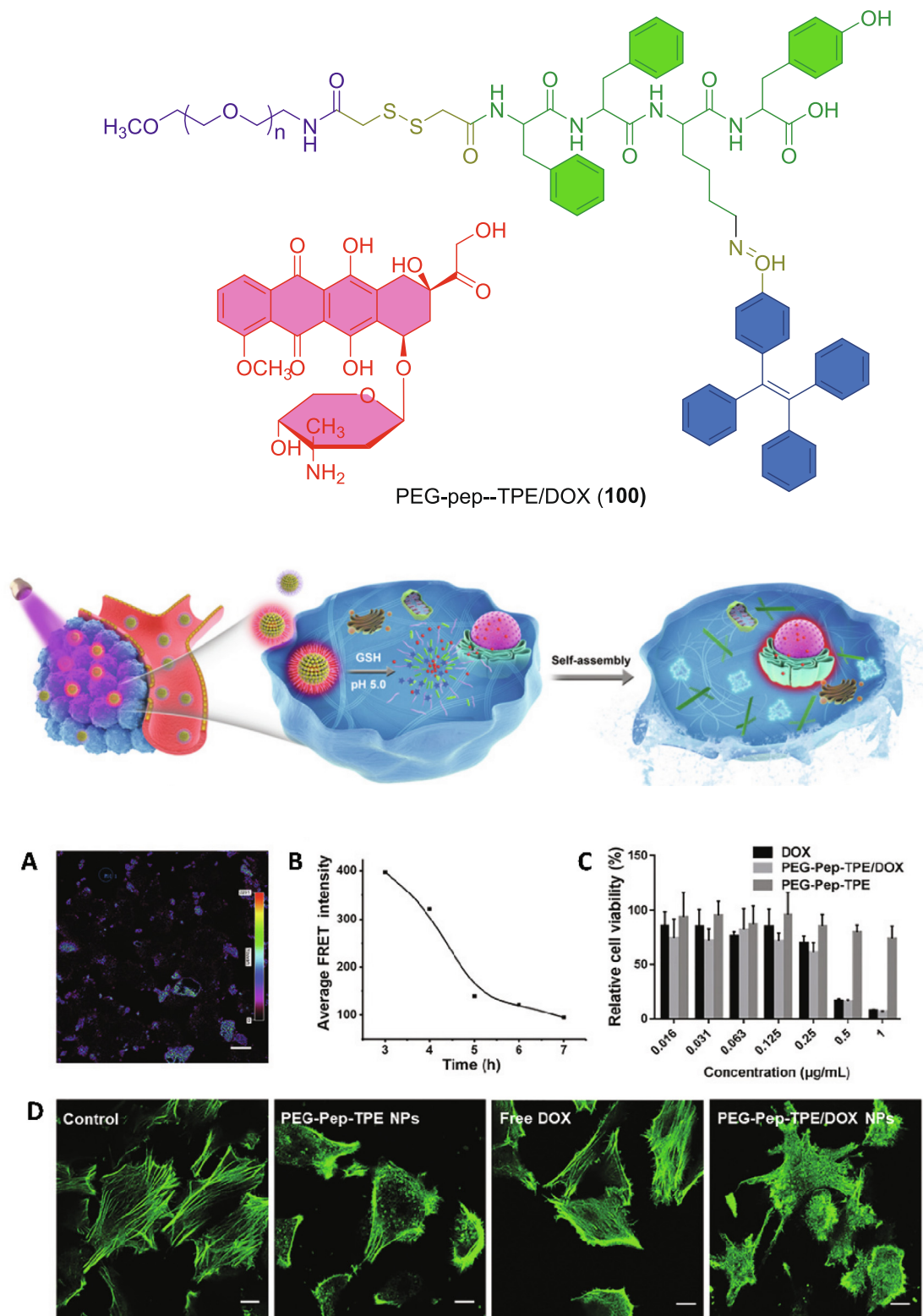
PEG-pep--TPE/DOX (**100**)

Fig. 47. Structure of PEG-Pep-TPE/DOX (**100**) and Schematic representation of drug release behaviour of the self-assembled PEG-Pep-TPE/DOX (**100**) nanoparticles. (A) FRET intensities analysis of the A549 cells with NPs **100** for 3 h; (B) Plot of average FRET intensity versus time of A549 cells with NPs **100** for 3 h; (C) *in vitro* cytotoxicity of free DOX, NPs **100** and PEG-PepTPE NPs against the A549 cells after 72 h; (D) Confocal images of pre-treated cells for 12 h with PBS control, PEG-PepTPE NPs, free DOX and NPs **100**. Reproduced with permission from [178]. Copyright 2020 The Royal Society of Chemistry.
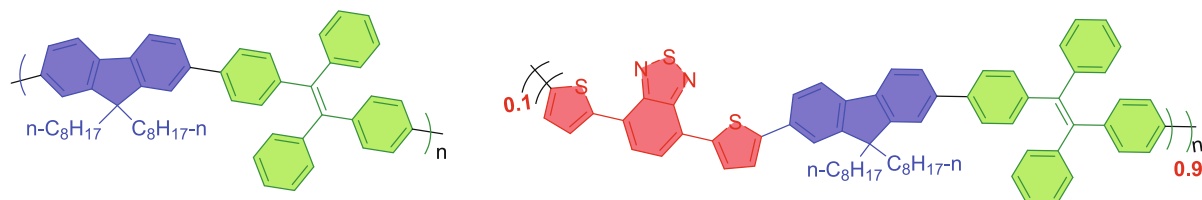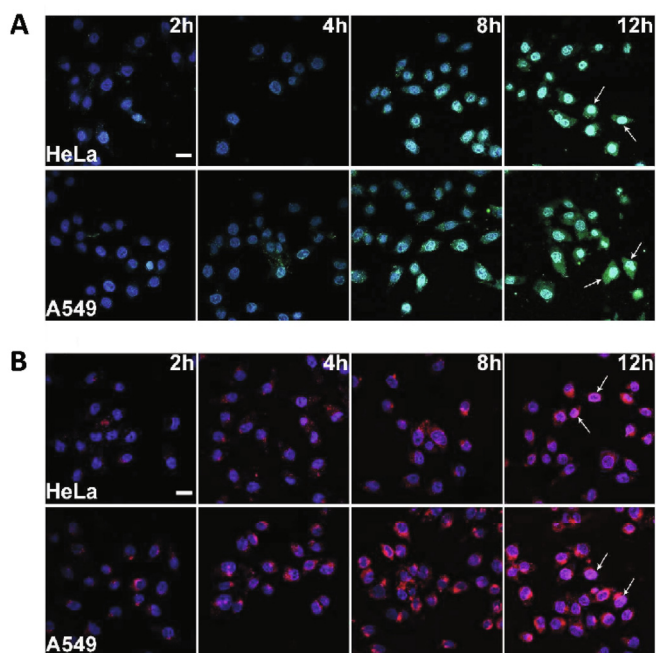
101

102

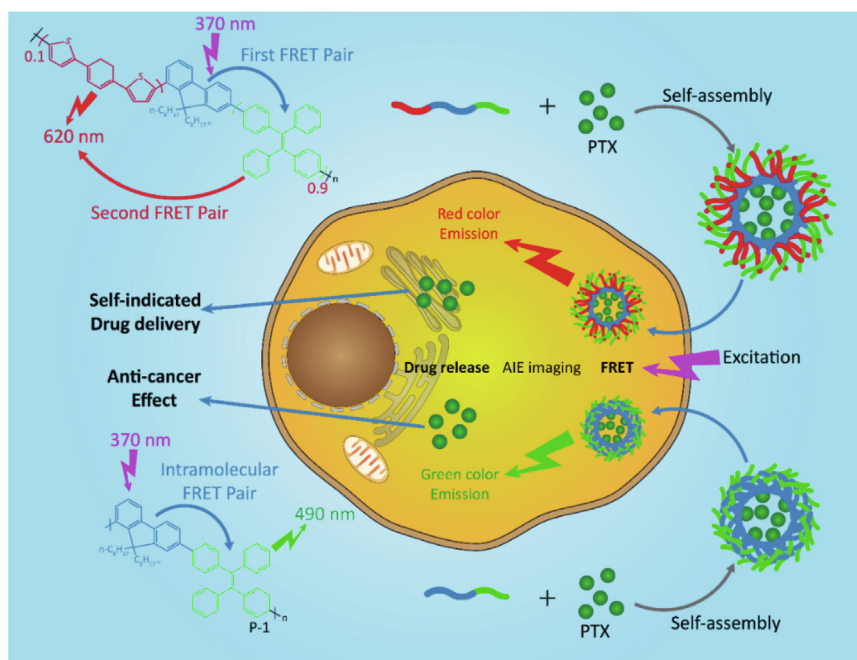**Fig. 48.** Structures of **101** and **102** and representation of the self-indicated tumor treatment using AIE-active CPNs as drug carriers. (A) Cellular imaging of PTX-loaded **CPNs-101** and (B) **CPNs-102** in HeLa and A549 cells [green signal from PTX-loaded **CPNs-101** and red signal from PTX-loaded **CPNs-102**]. Reproduced with permission from [179]. Copyright 2020 The Royal Society of Chemistry.
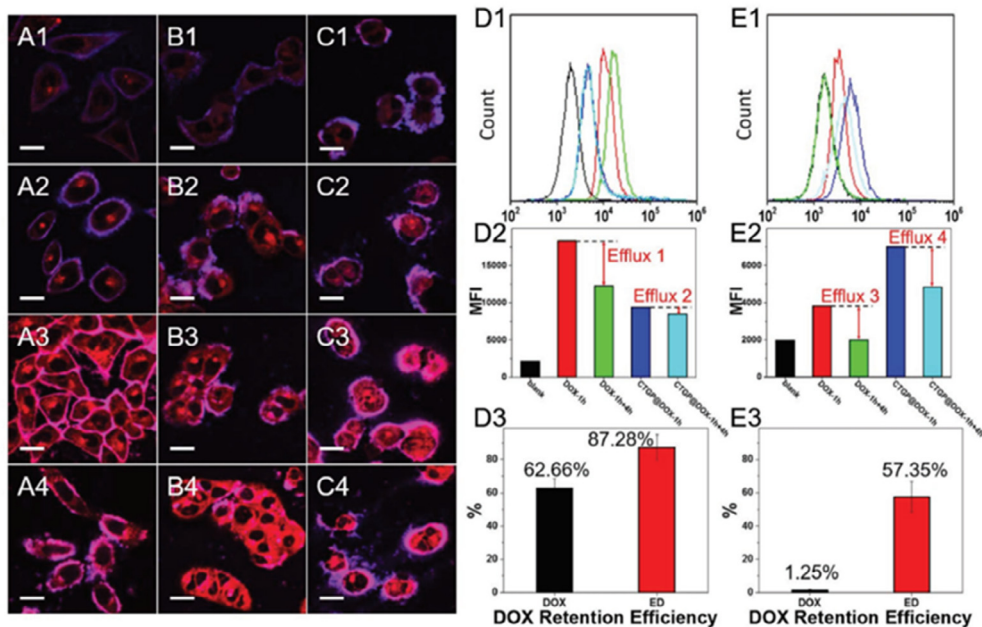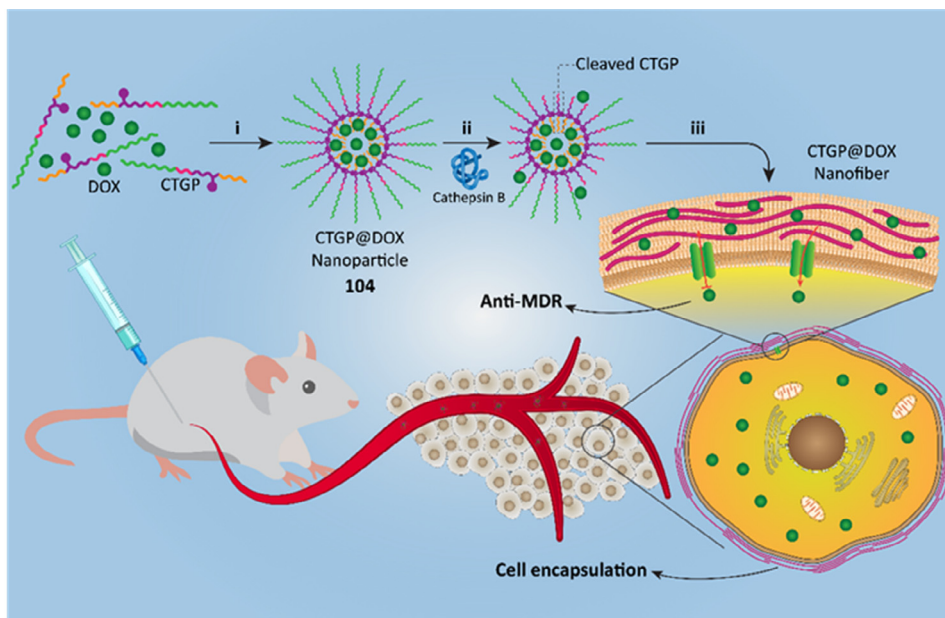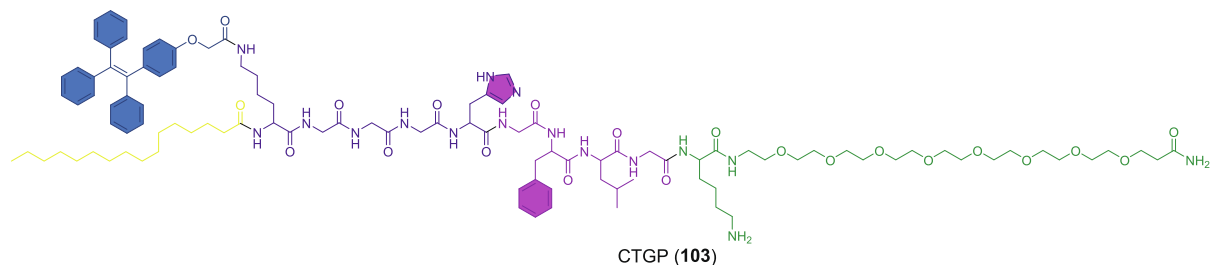
Fig. 49. Structures of CTGP (**103**) and CTGP@DOX (**104**). Suggested mechanisms of i) peptide-DOX self-assembly, ii) cathepsin B-instructed micelles disassociation with DOX release and fluorescence recovery, and iii) CTGP@DOX nanofiber reassembly; CLSM images of (A1–A4) MCF-7S cells; (B1–B4) MCF-7R cells and (C1–C4) MCF-7R cells pretreated with P-gp inhibitor after incubation with **104**; (D1, E1) Flow cytometry analysis of MCF-7S and MCF-7R cells after treated with free DOX and **104**; (D2, E2) The fluorescence intensity of intracellular DOX assessed by flow cytometry; (D3, E3) DOX retention efficiency for MCF-7S and MCF-7R cells. Reproduced with permission from [180]. Copyright 2018 WILEY-VCH Verlag GmbH & Co.

TPE (**105**)

Fig. 50. Structure of **105**; (A) Flow cytometric analyses of the internalization by HUVEC cells at pH 6.5 and (B) by macrophages cells at pH 6.5 of STD-NM_{drug} (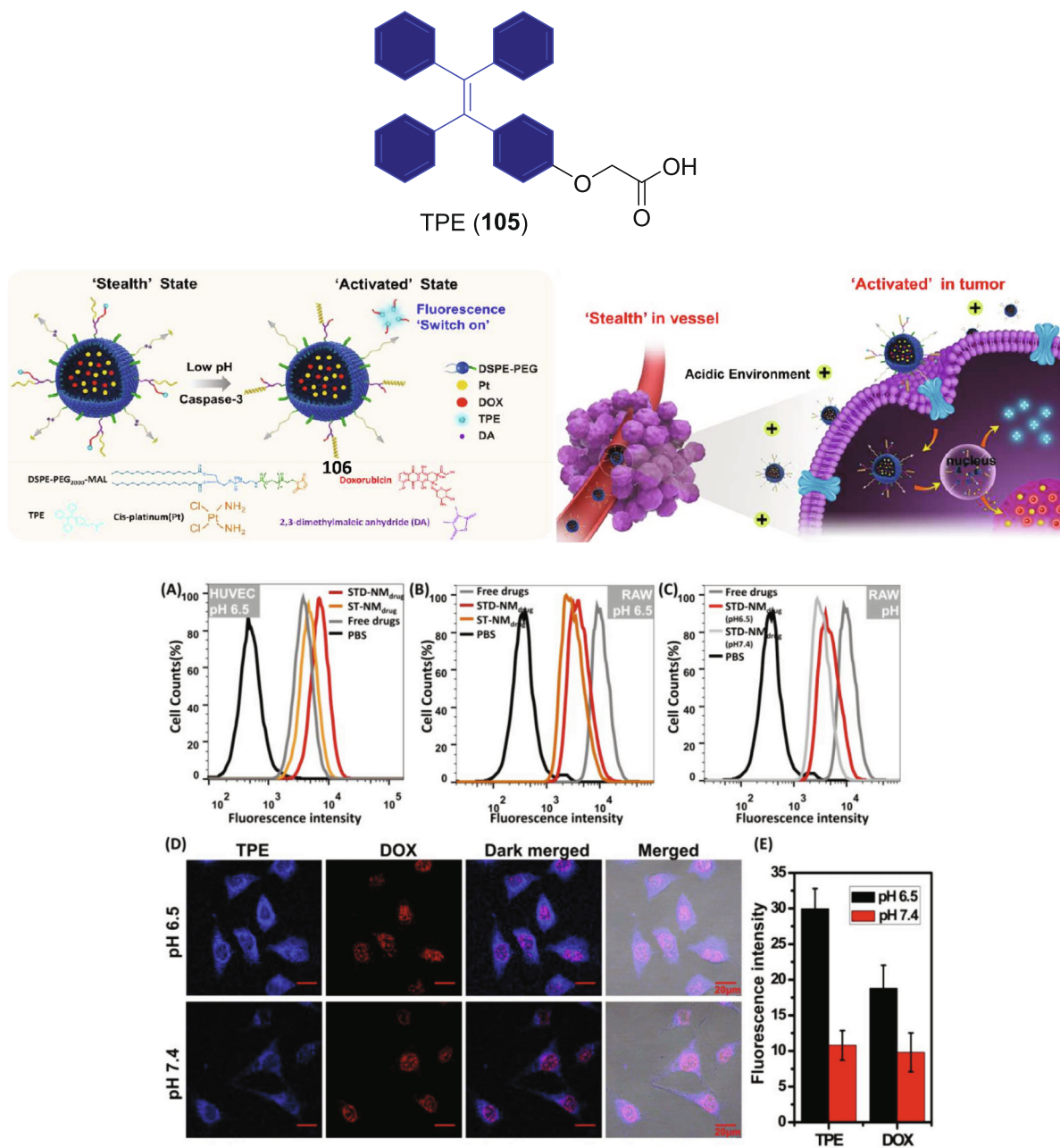**106**), ST-NM_{drug}, Free DOX respectively; (C) Flow cytometric analyses of the internalization of STD-NM_{drug} by macrophages cells at different conditions; (D) CLSM images of **106** toward HUVEC cells at various conditions; (E) The fluorescence intensity of TPE and DOX, respectively. Reproduced with permission from [181]. Copyright **2019** Elsevier.

is very useful tool for successive endo/lysosomal escape and DNA unpacking, which are key events for gene delivery. The intracellular trafficking profile (Fig. 53A–E) of ROS-sensitive nanoparticles (S-NPs)/DNA complexes confirms that the complexes are entrapped in endo/lysosomes (Fig. 53A3 & A4), Fig. 53B1-4 indicates light-induced intracellular DNA release after polymer breakdown (Fig. 53D2).

Nanoscale coordination polymers (NCPs) are organic–inorganic hybrid materials constructed from the metal ion and polydentate bridging organic core, represent a key entity for future nanomaterial application in nanomedicine. A new TPE immobilized zirconium-containing nanoscale coordination polymer **115** (TPE-NCPs) [186] with improved AIE behavior has been prepared by introducing tetrakis(4-carboxyphenyl)ethylene acids **64** into
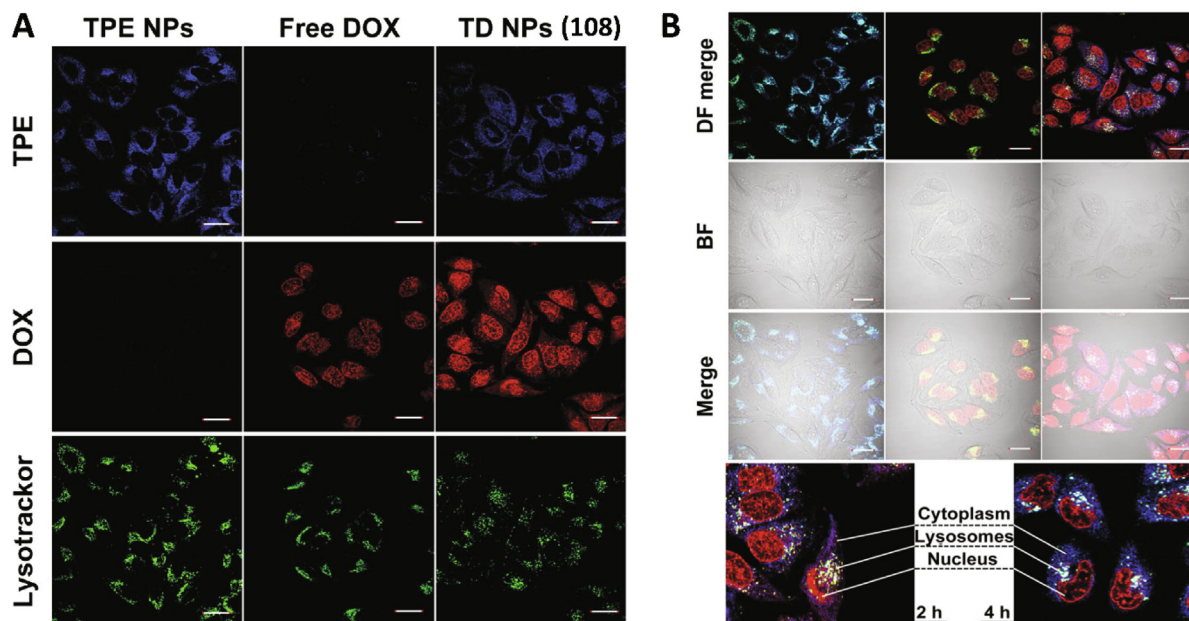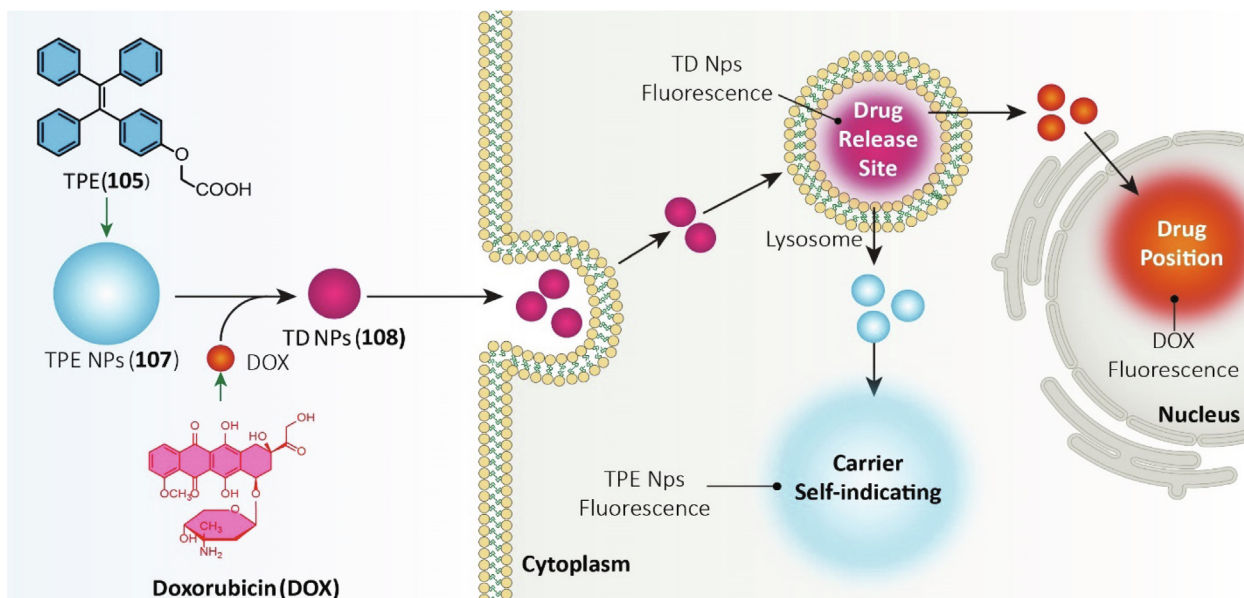
Fig. 51. Structure of **105** and Schematic illustration showing the formation of TD NPs. Spatial distributions of TPE NPs, DOX and TD NPs in MCF-7 s cells. (A) CLSM images of TPE NPs, DOX and TD NPs and lysosomes, indicated by Lysotracker Green. (B) The breast cancer MCF-7 s cells were incubating with TPE NPs, DOX and TD NPs for 2 h. Detailed TD NPs spatiotemporal distributions in MCF-7 s cells. Reproduced with permission from [182]. Copyright **2014** Wiley.

zirconium-based NCPs (Fig. 54). The drug loading and drug delivering ability of NCP-1–150 (150 stands for 150 μL of acetic acid) as drug vehicle has been investigated by choosing Curcumin (Cur) as model anticancer drug. UV–Vis absorption spectra (Fig. 54a) with maximum at 425 nm represent the successful loading of Cur, which is further supplemented with 1010 cm^{-1} in FTIR spectra accounted for stretching frequency of alcohol group from Cur [187]. *In-vitro* drug release of Cur@NCP-1–150 in phosphate-buffer saline (PBS) at 37 °C is monitored at 7.4 and 5.0 pH values

(Fig. 54b). More than 53.7 % and 40.4 % of Cur are released from Cur@NCP-1–150 in acidic and neutral PBS solution respectively in 96 h. Good structural stability of NCP-1–150 is confirmed by PXRD pattern of nanocarrier after drug release indicating the nanoplatform suitability for efficient drug loading.

The significance of mechanically interlocked molecules like rotaxane-based architectures for drug delivery has been well explored by Guocan Yu and coworkers [188]. They have used substituted TPE **116** and triphenylphosphonium (TPP) **117** molecules
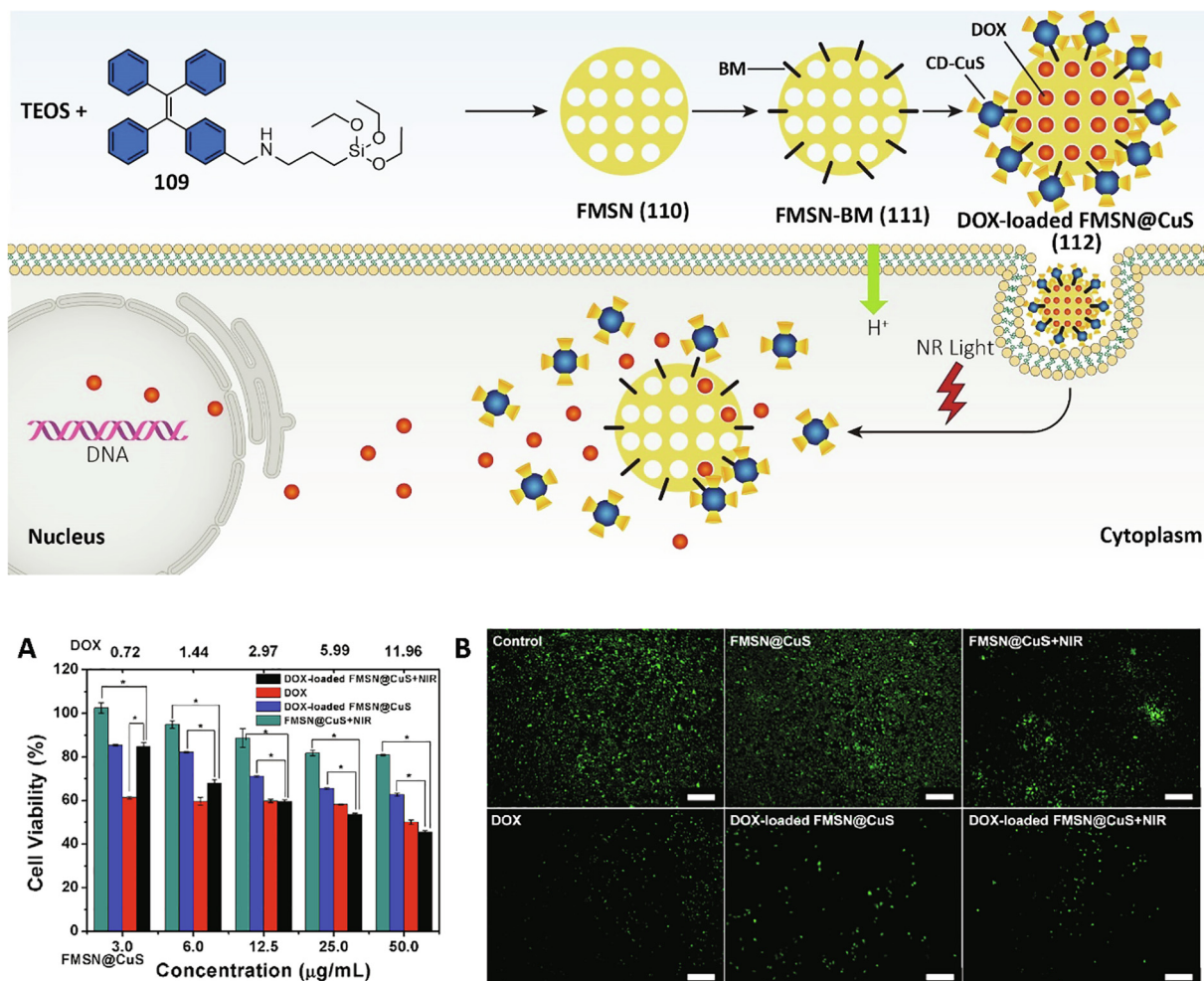
Fig. 52. Structure of **109** and Schematic illustration showing the Preparation Process of the DOX-Loaded FMSN@CuS (**112**). (A) In vitro viabilities of SGC-7901 cells after incubation with different concentrations of free DOX, FMSN@CuS and DOX-loaded FMSN@CuS with or without NIR irradiation. B) Fluorescence microscope images of SGC-7901 cells with various treatments stained with calcium-AM. Reproduced with permission from [183]. Copyright **2018** American Chemical Society.

as stoppers to fabricate a rotaxane (**R1**) (Fig. 55). The TPE moiety behaved as an AIE-active fluorogen in the synthesized rotaxane **R1**, and TPP utilized as a mitochondria-targeting core. The AIE effect of **R1** is significantly better than the free axle, may be due to the RIR of aromatic part of the TPE molecule upon [2]rotaxane structure formation. The resulted rotaxane displayed excellent photostability and specificity to target mitochondria. The prodrug **R2** (Fig. 55) was constructed by incorporating DOX into **R1**. **R2** acted as dual-fluorescence-quenched Forster resonance energy transfer system, in which TPE acted as the donor fluorophore and DOX as acceptor. The fluorescences of the drug (DOX) and the car-rier (**R1**) is recovered upon **R2** hydrolysis in endo/lysosomes, displaying a dual-color fluorogenic process. The escaped DOX and **R1** from endo/lysosomes, goes forward to nucleus and mitochondria via cytoplasm, and crossed the mitochondrial and nuclear membrane respectively. **R1** was further utilized as a carrier to conjugate other amine functional anticancer drug (cytarabine hydrochloride, temozolomide and gemcitabine) through imine formation. The cytotoxic studies indicating the selective accumulation of prodrug **R2** in cancer cells (HeLa cells) over normal cells (HEK293 cells) attributed to higher negative membrane potential of cancer cells vs. normal cells.
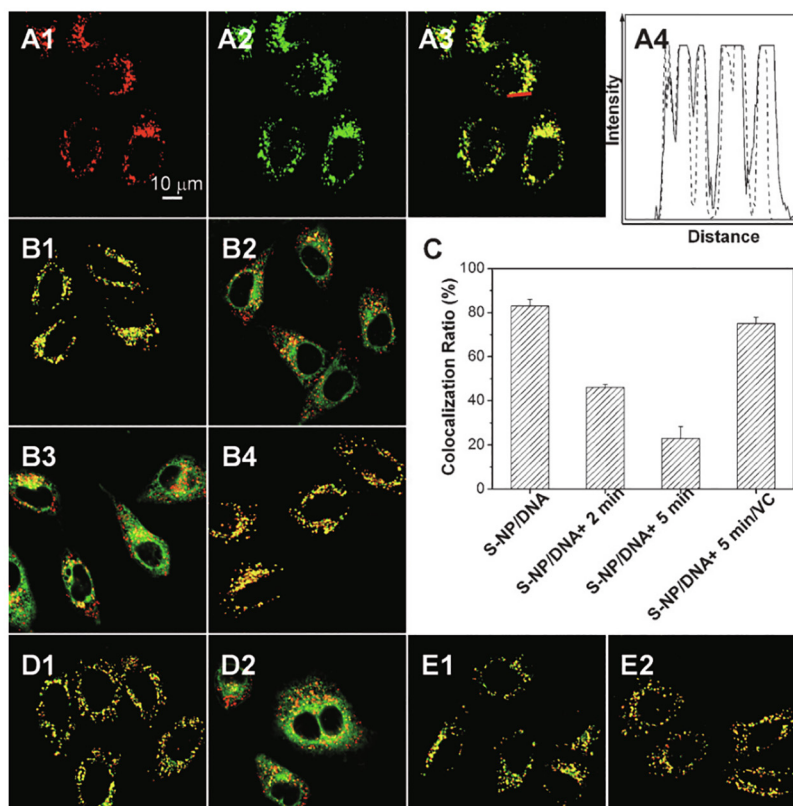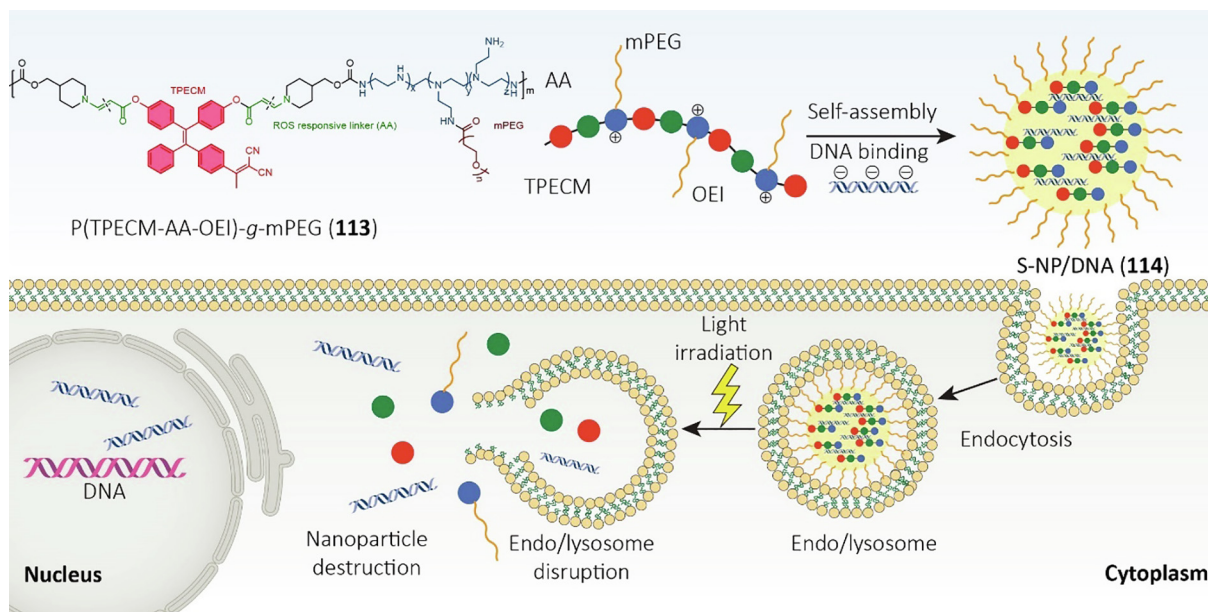
Fig. 53. Structure of **113** and schematic representation of the ROS-sensitive nanoparticles (S-NPs) self-assembled from P(TPECM-AA-OEI)-g-Mpeg. (A) CLSM images of HeLa cells stained with S-NPs/DNA (A1) and LysoTracker green (A2); overlay of the images A1 and A2 (A3); intensity profiles of region of interest (A4). (B) CLSM images of HeLa cells incubated with S-NPs/YOYO-1-DNA complexes in the dark (B1), with light irradiation for 2 min (B2), 5 min (B3), and 5 min in the presence of VC (B4). Green: YOYO-1 fluorescence; Red: S-NPs. Yellow: colocalization of red and green pixels. (C) Changes in colocalization ratios between the fluorescence of YOYO-1 and S-NPs after different treatment. (D,E) CLSM images of HeLa cells after incubation with D) S-NPs/YOYO-1-DNA pretreated with chloroquine (CQ), E) inS-NPs/ YOYO-1-DNA in the dark (D1, E1) or after 5 min light irradiation (D2, E2). Reproduced with permission from [185]. Copyright **2015** Wiley.
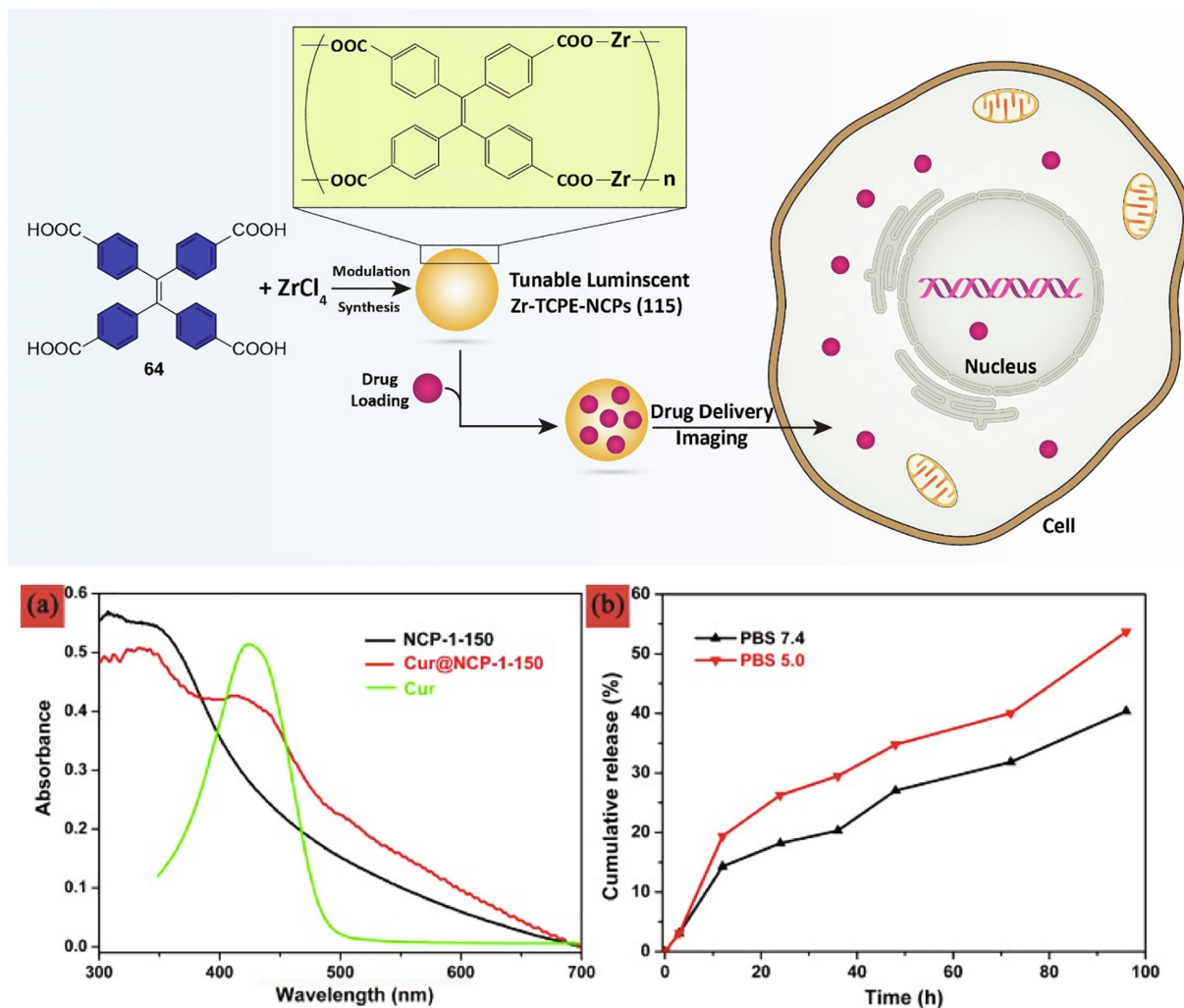
Fig. 54. Structure of **64** and schematic presentation of Zr-TCPE NCPs (**115**) synthesis and its application in drug delivery and cell imaging; Drug encapsulation and delivery of **NCP-1–150** nanoparticles. (a) UV–vis spectra of **NCP-1–150** carriers, **Cur@NCP-1–150** and free Cur molecules. (b) In vitro release profiles of Cur from **Cur@NCP-1–150** nanocarriers at different PBS 7.4 and 5.0 at room temperature. Reproduced with permission from [186]. Copyright **2013** Royal Society of Chemistry.
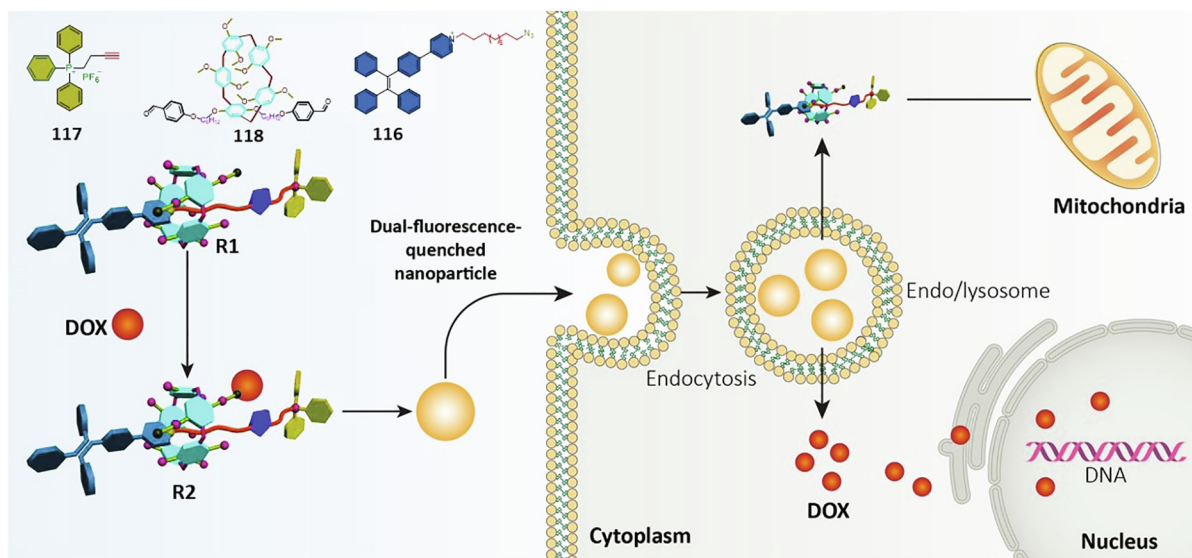
Fig. 55. (Left) Synthetic route to R1 and chemical structures of some compounds. (Right) Schematic illustration of the preparation of a mitochondria-targeting probe-inspired prodrug R2 and possible cellular pathways of the dual-fluorescence-quenched R2 nanoparticles. Reproduced with permission from [188]. Copyright **2016** Royal Society of Chemistry.

9. Conclusion and future perspective

The development of materials with high fluorescent characteristics in the solid and aggregated states has shown academic value as well as the technological interest due to their implications in biomolecular science. AIE is a nonconventional large polymer molecule that emits fluorescence under UV irradiation in the aggregated or solid-state. Such a phenomenon is reverse to conventional fluorophore macromolecules, which quench their luminescence in the aggregation state. Moreover, the resultant of conjugating AIE luminogens with biomolecules *via* covalent linkage without reducing its fluorescence intensity is considered as excellent candidate for various biomedical applications. These bioconjugates have shown all desired properties for biological applications such as biocompatibility, water solubility, specificity to the target cells, and smart responsiveness. TPE is so far the most studied AIE luminogen due to its mechanoluminescent properties and it can quench the notorious ACQ property of the material that is adverse for many applications.

In spite of remarkable advances in application of AIEgens in disease therapy and biosensing, there are some challenges that should be addressed to direct future experiments for finding an effective solution. The first drawback is attributed to preparation route of AIEgens [178]. Designing a novel and easy method for AIE polymer construction, preparation of AIEgens from photochemical and electrochemical reactions as sustainable methods, and finding an easy way for synthesis of NIR-II emissive AIEgens are among them [178]. The next studies can focus on developing a novel strategy for addressing aforementioned challenges. It is also worth mentioning that designing AIEgens with multifunctional application can be achieved via embedding adjustable agents in AIE core that can be the focus of future experiments.

As it was discussed in main text, AIEgens demonstrate luminescence feature when they aggregate [189]. The luminescence characteristic of AIEgens results from their twisted and nonplanar shape, preventing their quenching in aggregation form. However, their nonplanar shape avoids the ordered structure of AIEgens. Besides, a wide variety of experiments have shown that AIEgens can be applied for biosensing, detection of resistant pathogens and tumor cells. Although it has been reported that AIEgens have high biocompatibility and can provide live imaging, the cellular uptake mechanism of AIEgens has not been completely investigated. It has been shown that endocytosis is an important pathway that AIEgens utilize in entering into cells. However, endocytosis has different kinds including clathrin, caveolin, clathrin- and -caveolae-independent endocytosis and phagocytosis. Now there are some questions that come into mind. Which is the main endocytic pathway for internalization of AIEgens? How cellular uptake of AIEgens can be improved? And finally, various sizes of AIEgens use which endocytic pathway for cellular internalization? Finding an answer for these questions can pave the way for developing more effective AIEgens, since these nanostructures have been loaded with drugs that enhance their size and may challenge their cellular uptake. The final issue that can be addressed, is use of AIEgens in bacterial detection. Increasing evidence has revealed potential function of AIEgens in detecting Gram-positive and Gram-negative bacteria due to interacting with surface via electrostatic or hydrophobic/hydrophilic interactions [190]. However, clinical application of such AIEgens is restricted due to lack of selective detection and imaging of certain bacteria (no specificity).

The increasing evidence (*in vitro and in vivo*) reveals high biocompatibility of AIEgens. The intravenous injection of AIEgens leads to partial *in vivo* toxicity in mice, as major organs of body (spleen, liver and kidney) have been examined and blood tests also confirm high biocompatibility of these nanostructures. In terms of clearance, AIEgens are mainly excreted by biliary pathway instead of renal pathway. It has been reported that upon 9 days of AIEgens injection, most of these nanoparticles will be present in feces with partial existence in urine [191]. These features of AIEgens make them appropriate options for clinical application. Furthermore, in order to improve biocompatibility of AIEgens, their functionalization with biomacromolecules including nucleic acids, peptides, lipids and glycans is performed. The covalent bond, electrostatic interaction and hydrophobic effect can mediate AIEgen functionalization with biomacromolecules. In addition to improving biocompatibility, such conjugation with biomacromolecules enhances selectivity of AIEgens towards tumor cells [192].

Although AIEgens demonstrate high efficiency for imaging and disease therapy, there are a number of inherent drawbacks including short-wavelength absorption, broad emission spectrum and nonoptimized emission that limit their biomedical uses. Fortunately, some solutions have been addressed for aforementioned issues. The multiphoton absorption, harmonic generation and upconversion method are nonlinear optics phenomenon and extensively applied in preparation of AIEgens via NIR light to overcome limitations of AIEgens. In order to reduce emission bandwidth of AIEgens and make it narrower, FERT, photonic crystals and harmonic generation are involved in AIE system. The bottom-up method is also suggested for improving brightness of AIEgens and their water disparity [193].

In conclusion, we have focused on various TPE based AIE luminogens and their potential application in biomedical science. Many applications of these luminogens are yet to be exploited. The present review aims to explore more excellent tetraphenyl ethylene-AIE luminogens-based functional materials for the use in biomedical areas such as cancer therapy, apoptosis and inflammation, tumour targeting, microorganism imaging therapy, and gene therapy etc and as well as other research areas.

Declaration of Competing Interest

The authors declare that they have no known competing financial interests or personal relationships that could have appeared to influence the work reported in this paper.

Acknowledgement

References

[1] L. Basabe-Desmonts, D.N. Reinhoudt, M. Crego-Calama, Chem. Soc. Rev. 36 (2007) 993–1017.
[2] N. Elahi, M. Kamali, M.H. Baghersad, B. Amini, Mater. Sci. Eng. C 105 (2019) 110113.
[3] A.B. Chinen, C.M. Guan, J.R. Ferrer, S.N. Barnaby, T.J. Merkel, C.A. Mirkin, Chem. Rev. 115 (2015) 10530–10574.
[4] P. Reineck, B.C. Gibson, Adv. Optical Mater. 5 (2017) 1600446.
[5] J. Yao, M. Yang, Y. Duan, Chem. Rev. 114 (2014) 6130–6178.
[6] P. Reineck, A. Francis, A. Orth, D.W.M. Lau, R.D.V. Nixon-Luke, I.D. Rastogi, W. A.W. Razali, N.M. Cordina, L.M. Parker, V.K.A. Sreenivasan, L.J. Brown, B.C. Gibson, Adv. Optical Mater. 4 (2016) 1549–1557.
[7] J. Liu, M. Evrard, X. Cai, G. Feng, N. Tomczak, L.G. Ng, B. Liu, J. Mater. Chem. B 6 (2018) 2630–2636.
[8] H. Wang, E. Zhao, J.W.Y. Lam, B.Z. Tang, Mater. Today. 18 (2015) 365–377.
[9] J. Chen, C.C.W. Law, J.W.Y. Lam, Y. Dong, S.M.F. Lo, I.D. Williams, D. Zhu, B.Z. Tang, Chem. Mater. 15 (2003) 1535–1546.

[10] X. Fan, J. Sun, F. Wang, Z. Chu, P. Wang, Y. Dong, R. Hu, B.Z. Tang, D. Zou, ChemComm (2008) 2989–2991.
[11] Z. He, C. Ke, B.Z. Tang, ACS Omega 3 (2018) 3267–3277.
[12] J. Luo, Z. Xie, J.W.Y. Lam, L. Cheng, H. Chen, C. Qiu, H.S. Kwok, X. Zhan, Y. Liu, D. Zhu, B.Z. Tang, ChemComm (2001) 1740–1741.
[13] J. Mei, N.L.C. Leung, R.T.K. Kwok, J.W.Y. Lam, B.Z. Tang, Chem. Rev. 115 (2015) (1940) 11718–11721.
[14] B.-K. An, S.-K. Kwon, S.-D. Jung, S.Y. Park, J. Am. Chem. Soc. 124 (2002) 14410–14415.
[15] Y. Hong, J.W.Y. Lam, B.Z. Tang, Chem. Soc. Rev. 40 (2011) 5361–5388.
[16] Y. Hong, J.W.Y. Lam, B.Z. Tang, ChemComm. (2009) 4332–4353.
[17] N.L.C. Leung, N. Xie, W. Yuan, Y. Liu, Q. Wu, Q. Peng, Q. Miao, J.W.Y. Lam, B.Z. Tang, Chem. Eur. J. 20 (2014) 15349–15353.
[18] Z. Zhao, J.W.Y. Lam, B.Z. Tang, J. Mater. Chem. 22 (2012) 23726–23740.
[19] X. Zhang, K. Wang, M. Liu, X. Zhang, L. Tao, Y. Chen, Y. Wei, Nanoscale 7 (2015) 11486–11508.
[20] Z. Zhao, B. He, B.Z. Tang, Chem. Sci. 6 (2015) 5347–5365.
[21] P. Gopikrishna, N. Meher, P.K. Iyer, ACS Appl. Mater. Interfaces 10 (2018) 12081–12111.
[22] Y. Xie, Z. Li, Mater. Chem. Front. 4 (2020) 317–331.
[23] H.-T. Feng, J.W.Y. Lam, B.Z. Tang, Coord. Chem. Rev. 406 (2020) 213142.
[24] S.K. Mellerup, S. Wang, Chem. Soc. Rev. 48 (2019) 3537–3549.
[25] H.-T. Feng, Y.-X. Yuan, J.-B. Xiong, Y.-S. Zheng, B.Z. Tang, Chem. Soc. Rev. 47 (2018) 7452–7476.
[26] C.W.T. Leung, Y. Hong, S. Chen, E. Zhao, J.W.Y. Lam, B.Z. Tang, J. Am. Chem. Soc. 135 (2013) 62–65.
[27] Z. Yang, W. Qin, N.L.C. Leung, M. Arseneault, J.W.Y. Lam, G. Liang, H.H.Y. Sung, I.D. Williams, B.Z. Tang, J. Mater. Chem. C 4 (2016) 99–107.
[28] X. Feng, C. Qi, H.-T. Feng, Z. Zhao, H.H.Y. Sung, I.D. Williams, R.T.K. Kwok, J.W. Y. Lam, A. Qin, B.Z. Tang, Chem. Sci. 9 (2018) 5679–5687.
[29] Y. Ooyama, R. Sagisaka, T. Enoki, N. Tsunoji, J. Ohshita, New J. Chem. 42 (2018) 13339–13350.
[30] W. Dong, Z. Ma, P. Chen, Q. Duan, Mater. Lett. 236 (2019) 480–482.
[31] N. Sun, K. Su, Z. Zhou, X. Tian, Z. Jianhua, D. Chao, D. Wang, F. Lissel, X. Zhao, C. Chen, Macromolecules 52 (2019) 5131–5139.
[32] Q. Zhao, X.A. Zhang, Q. Wei, J. Wang, X.Y. Shen, A. Qin, J.Z. Sun, B.Z. Tang, ChemComm. 48 (2012) 11671–11673.
[33] T. Jadhav, B. Dhokale, Y. patil, R. Misra, RSC Adv. 5 (2015) 68187-68191.
[34] Y. Zhao, S. He, J. Yang, H. Sun, X. Shen, X. Han, Z. Ni, Opt. Mater. 81 (2018) 102–108.
[35] J. Wang, C. Li, Q. Chen, H. Li, L. Zhou, X. Jiang, M. Shi, P. Zhang, G. Jiang, B.Z. Tang, Anal. Chem. 91 (2019) 9388–9392.
[36] M.Z. Chen, N.S. Moily, J.L. Bridgford, R.J. Wood, M. Radwan, T.A. Smith, Z. Song, B.Z. Tang, L. Tilley, X. Xu, G.E. Reid, M.A. Pouladi, Y. Hong, D.M. Hatters, Nat. Commun. 8 (2017) 474.
[37] P. Boissieu, Bull. Soc. Chim. 49, 681–682.
[38] W. Wang, T. Lin, M. Wang, T.-X. Liu, L. Ren, D. Chen, S. Huang, J. Phys. Chem. B 114 (2010) 5983–5988.
[39] A. Schreivogel, J. Maurer, R. Winter, A. Baro, S. Laschat, Eur. J. Org. Chem. (2006) 3395–3404.
[40] G. Hua, Y. Li, A.M.Z. Slawin, J.D. Woollins, Dalton Trans. (2007) 1477–1480.
[41] L. Zhang, X. Yu, L. Zhang, X. Zhou, Y. Lin, Org. Chem. Front. 1 (2014) 929–935.
[42] S. Nadri, M. Joshaghani, E. Rafiee, Organometallics 28 (2009) 6281–6287.
[43] K. Okuma, K. Kojima, K. Oyama, K. Kubo, K. Shioji, Eur. J. Org. Chem. 2004 (2004) 820–825.
[44] Y. Tezuka, A. Hashimoto, K. Ushizaka, K. Imai, J. Org. Chem. 55 (1990) 329–333.
[45] K. Sajna, V. Srinivas, K.C. Kumara Swamy, Adv. Synth. Catal. 352 (2010) 3069–3081.
[46] Z. Yang, Z. Chi, Z. Mao, Y. Zhang, S. Liu, J. Zhao, M.P. Aldred, Z. Chi, Mater. Chem. Front. 2 (2018) 861–890.
[47] Y. Wang, Y. Liao, C.P. Cabry, D. Zhou, G. Xie, Z. Qu, D.W. Bruce, W. Zhu, J. Mater. Chem. C. 5 (2017) 3999–4008.
[48] M. Hu, H.-T. Feng, Y.-X. Yuan, Y.-S. Zheng, B.Z. Tang, Coord. Chem. Rev. 416 (2020) 213329.
[49] F. Zhang, J. Fan, H. Yu, Z. Ke, C. Nie, D. Kuang, G. Shao, C. Su, J. Org. Chem. 80 (2015) 9034–9040.
[50] F. Hu, B. Liu, Org. Biomol. Chem. 14 (2016) 9931–9944.
[51] Z. Song, Y. Hong, R.T.K. Kwok, J.W.Y. Lam, B. Liu, B.Z. Tang, J. Mater. Chem. B 2 (2014) 1717–1723.
[52] W. Chen, C. Zhang, X. Han, S.H. Liu, Y. Tan, J. Yin, J. Org. Chem. 84 (2019) 14498–14507.
[53] G. Yu, T.R. Cook, Y. Li, X. Yan, D. Wu, L. Shao, J. Shen, G. Tang, F. Huang, X. Chen, P.J. Stang, Proc. Natl. Acad. Sci. U.S.A. 113 (2016) 13720–13725.
[54] X. Cai, B. Liu, Angew. Chem. Int. Ed. 59 (2020) 9868–9886.
[55] S. Seshadri, A. Beiser, J. Selhub, P.F. Jacques, I.H. Rosenberg, R.B. D'Agostino, P. W.F. Wilson, P.A. Wolf, N. *Engl. J. Med.* 346 (2002) 476–483.
[56] P. Colombatto, A. Randone, G. Civitico, J.M. Gorin, L. Dolci, N. Medaina, F. Oliveri, G. Verme, G. Marchiaro, R. Pagni, P. Karayiannis, H.C. Thomas, G. Hess, F. Bonino, M.R. Brunetto, J. Viral Hepat. 3 (1996) 301–306.
[57] C.J. Rosen, J.E. Compston, J.B. Lian, John Wiley & Sons (2009).
[58] O. Jacobson, Y. Bechor, A. Icar, N. Novak, A. Birman, H. Marom, L. Fadeeva, E. Golan, I. Leibovitch, M. Gutman, E. Even-Sapir, R. Chisin, M. Gozin, E. Mishani, Bioorg. Med. Chem. 13 (2005) 6195–6205.
[59] B. Cai, S. Guo, Y. Li, Anal. Methods 10 (2018) 230–236.
[60] D. Bruen, C. Delaney, L. Florea, D. Diamond, Sensors (Basel) 17 (2017) 1866.
[61] W. Liu, W. Yu, X. Li, X. Zhao, Y. Zhang, P. Song, Y. Yin, R. Xi, M. Meng, Sens. Actuators B Chem. 266 (2018) 170–177.
[62] X.-M. Hu, Q. Chen, J.-X. Wang, Q.-Y. Cheng, C.-G. Yan, J. Cao, Y.-J. He, B.-H. Han, Chem. Asian J. 6 (2011) 2376–2381.
[63] G. Jiang, X. Liu, Q. Chen, G. Zeng, Y. Wu, X. Dong, G. Zhang, Y. Li, X. Fan, J. Wang, Sens. Actuators B Chem. 252 (2017) 712–716.
[64] G. Jiang, G. Zeng, W. Zhu, Y. Li, X. Dong, G. Zhang, X. Fan, J. Wang, Y. Wu, B.Z. Tang, ChemComm 53 (2017) 4505–4508.
[65] J. Shi, S. Zhang, M. Zheng, Q. Deng, C. Zheng, J. Li, F. Huang, Sens. Actuators B Chem. 238 (2017) 765–771.
[66] B.A. Rader, Front. Immunol. 8 (2017).
[67] J.E. Coleman, Annu. Rev. Biophys. Biomol. Struct. 21 (1992) 441–483.
[68] C. Wang, J. Gao, Y. Cao, H. Tan, Anal. Chim. Acta 1004 (2018) 74–81.
[69] X. Chen, Y. He, Y. Zhang, M. Liu, Y. Liu, J. Li, Nanoscale 6 (2014) 11196–11203.
[70] Y. Zhu, G. Wang, H. Jiang, L. Chen, X. Zhang, ChemComm. 51 (2015) 948–951.
[71] Y. Zeng, J.-Q. Ren, S.-K. Wang, J.-M. Mai, B. Qu, Y. Zhang, A.-G. Shen, J.-M. Hu, ACS Appl. Mater. Interfaces 9 (2017) 29547–29553.
[72] B.D. Gill, H.E. Indyk, Int. Dairy J. 17 (2007) 596–605.
[73] A.-X. Ding, Y.-D. Shi, K.-X. Zhang, W. Sun, Z.-L. Tan, Z.-L. Lu, L. He, Sens. Actuators B Chem. 255 (2018) 440–447.
[74] X. Chen, Y. Zhou, X. Peng, J. Yoon, Chem. Soc. Rev. 39 (2010) 2120–2135.
[75] S.-P. Wang, W.-J. Deng, D. Sun, M. Yan, H. Zheng, J.-G. Xu, Org. Biomol. Chem. 7 (2009) 4017–4020.
[76] M.M. Mohamed, B.F. Sloane, Nat. Rev. Cancer. 6 (2006) 764–775.
[77] J. Lin, I.-M. Lee, Y. Song, N.R. Cook, J. Selhub, J.E. Manson, J.E. Buring, S.M. Zhang, Cancer Res. 70 (2010) 2397–2405.
[78] J. Wang, Y.F. Li, C.Z. Huang, T. Wu, Anal. Chim. Acta 626 (2008) 37–43.
[79] Y.V. Tcherkas, A.D. Denisenko, J. Chromatogr. A 913 (2001) 309–313.
[80] O. Rusin, N.N. St, R.A. Luce, J.O. Agbaria, S. Escobedo, I.M. Jiang, F.B. Warner, K. Dawan, R.M.S. Lian, J. Am. Chem. Soc. 126 (2004) 438–439.
[81] G. Chen, L. Zhang, J. Wang, Talanta. 64 (2004) 1018–1023.
[82] X. Gao, X. Li, L. Li, J. Zhou, H. Ma, ChemComm 51 (2015) 9388–9390.
[83] S. Huang, Y. Wu, F. Zeng, J. Chen, S. Wu, Anal. Chim. Acta 1031 (2018) 169–177.
[84] J. Shi, Q. Deng, C. Wan, M. Zheng, F. Huang, B. Tang, Chem. Sci. 8 (2017) 6188–6195.
[85] G. Jiang, W. Zhu, Q. Chen, X. Li, G. Zhang, Y. Li, X. Fan, J. Wang, Sens. Actuators B Chem. 261 (2018) 602–607.
[86] Y.-X. Yuan, H.-C. Zhang, M. Hu, Q. Zhou, B.-X. Wu, F.-L. Wang, M.-H. Liu, Y.-S. Zheng, Org. Lett. 22 (2020) 1836–1840.
[87] X. Qian, Z. Xu, Chem. Soc. Rev. 44 (2015) 4487–4493.
[88] J.F. Zhang, Y. Zhou, J. Yoon, J.S. Kim, Chem. Soc. Rev. 40 (2011) 3416–3429.
[89] M. Shyamal, P. Mazumdar, S. Maity, S. Samanta, G.P. Sahoo, A. Misra, ACS Sens. 1 (2016) 739–747.
[90] M.K. Rai, S.D. Deshmukh, A.P. Ingle, A.K. Gade, J. Appl. Microbiol. 112 (2012) 841–852.
[91] Y. Chen, W. Zhang, Y. Cai, R.T.K. Kwok, Y. Hu, J.W.Y. Lam, X. Gu, Z. He, Z. Zhao, X. Zheng, B. Chen, C. Gui, B.Z. Tang, Chem. Sci. 8 (2017) 2047–2055.
[92] R. Hu, N.L.C. Leung, B.Z. Tang, Chem. Soc. Rev. 43 (2014) 4494–4562.
[93] Y. Zhao, W. Zhu, L. Ren, K. Zhang, Polym. Chem. 7 (2016) 5386–5395.
[94] Z. Zhou, X. Li, Y. Zhang, C.C. Zhang, Y. Tang, J. Gao, L. Ma, Q. Wang, Mater. Sci. Eng. C 99 (2019) 1092–1098.
[95] M.J. Chang, M.H. Lee, Dyes Pigm. 149 (2018) 915–920.
[96] K. Li, Z. Li, D. Liu, M. Chen, S.-C. Wang, Y.-T. Chan, P. Wang, Inorg. Chem. 59 (2020) 6640–6645.
[97] X. Feng, Y. Li, X. He, H. Liu, Z. Zhao, R.T.K. Kwok, M.R.J. Elsegood, J.W.Y. Lam, B. Z. Tang, Adv. Funct. Mater. 28 (2018) 1802833.
[98] Y. Zheng, H. Wang, J. Jiang, Dyes Pigm. 173 (2020) 107929.
[99] J. Xiu, N. Zhang, C. Li, A. Salah, G. Wang, Microporous Mesoporous Mater. 316 (2021) 110979.
[100] T.D. Ashton, K.A. Jolliffe, F.M. Pfeffer, Chem. Soc. Rev. 44 (2015) 4547–4595.
[101] X. Chen, Nanoplatform-based Molecular Imaging, John Wiley & Sons, 2011.
[102] N. Adonai, K.N. Nguyen, J. Walsh, M. Iyer, T. Toyokuni, M.E. Phelps, T. McCarthy, D.W. McCarthy, S.S. Gambhir, Proc. Natl. Acad. Sci. U.S.A. 99 (2002) 3030–3035.
[103] D.-E. Lee, H. Koo, I.-C. Sun, J.H. Ryu, K. Kim, I.C. Kwon, Chem. Soc. Rev. 41 (2012) 2656–2672.
[104] C. Koros, A. Simitsi, A. Prentakis, I. Beratis, D. Papadimitriou, D. Kontaxopoulou, S. Fragkiadaki, N. Papagiannakis, J. Seibyl, K. Marek, S.G. Papageorgiou, X.G. Trapali, M. Stamelou, L. Stefanis, Mov. Disord. 33 (2018) 1734–1739.
[105] R.M. Clauson, M. Chen, L.M. Scheetz, B. Berg, B. Chertok, ACS Appl. Mater. Interfaces. 10 (2018) 20281–20295.
[106] J. Zhang, M. Zheng, F. Zhang, B. Xu, W. Tian, Z. Xie, Chem. Mater. 28 (2016) 8825–8833.
[107] Y.-H. Chan, P.-J. Wu, Part Part Syst. Charact. 32 (2015) 11–28.
[108] H.-B. Cheng, Y. Li, B.Z. Tang, J. Yoon, Chem. Soc. Rev. 49 (2020) 21–31.
[109] L. Zhang, E. Wang, Nano Today 9 (2014) 132–157.
[110] T. Kowada, H. Maeda, K. Kikuchi, Chem. Soc. Rev. 44 (2015) 4953–4972.
[111] X. Gao, Y. Cui, R.M. Levenson, L.W.K. Chung, S. Nie, Nat. Biotechnol. 22 (2004) 969–976.
[112] B. Situ, S. Chen, E. Zhao, C.W.T. Leung, Y. Chen, Y. Hong, J.W.Y. Lam, Z. Wen, W. Liu, W. Zhang, L. Zheng, B.Z. Tang, Adv. Funct. Mater. 26 (2016) 7132–7138.
[113] Y. Yu, C. Feng, Y. Hong, J. Liu, S. Chen, K.M. Ng, K.Q. Luo, B.Z. Tang, Adv. Mater. 23 (2011) 3298–3302.

[114] H. Zhu, J. Fan, J. Du, X. Peng, Acc. Chem. Res. 49 (2016) 2115–2126.
[115] X. Zhang, X. Zhang, L. Tao, Z. Chi, J. Xu, Y. Wei, J. Mater. Chem. B 2 (2014) 4398.
[116] H. Kobayashi, M. Ogawa, R. Alford, P.L. Choyke, Y. Urano, Chem. Rev. 110 (2010) 2620–2640.
[117] R.H. Newman, M.D. Fosbrink, J. Zhang, Chem. Rev. 111 (2011) 3614–3666.
[118] K.P. Carter, A.M. Young, A.E. Palmer, Chem. Rev. 114 (2014) 4564–4601.
[119] S. Doose, H. Neuweiler, M. Sauer, ChemPhysChem. 10 (2009) 1389–1398.
[120] S. Chen, Y. Hong, Y. Liu, J. Liu, C.W.T. Leung, M. Li, R.T.K. Kwok, E. Zhao, J.W.Y. Lam, Y. Yu, B.Z. Tang, J. Am. Chem. Soc. 135 (2013) 4926–4929.
[121] F. Hu, Y. Huang, G. Zhang, R. Zhao, H. Yang, D. Zhang, Anal. Chem. 86 (2014) 7987–7995.
[122] X. Zhao, Y. Chen, G. Niu, D. Gu, J. Wang, Y. Cao, Y. Yin, X. Li, D. Ding, R. Xi, M. Meng, ACS Appl. Mater. Interfaces 11 (2019) 13134–13139.
[123] X. Yang, Q. Wang, P. Hu, C. Xu, W. Guo, Z. Wang, Z. Mao, Z. Yang, C. Liu, G. Shi, L. Chen, B. Xu, Z. Chi, Mater. Chem. Front. 4 (2020) 941–949.
[124] Q. Wang, C. Li, Q. Chen, P. Zhang, D. Wang, M. Kang, G. Jiang, J. Wang, Anal. Chem. 91 (2019) 12611–12614.
[125] Y. Zhang, Y. Yan, S. Xia, S. Wan, T.E. Steenwinkel, J. Medford, E. Durocher, R.L. Luck, T. Werner, H. Liu, ACS Appl. Mater. Interfaces 12 (2020) 20172–20179.
[126] Y. Cai, C. Gui, K. Samedov, H. Su, X. Gu, S. Li, W. Luo, H.H.Y. Sung, J.W.Y. Lam, R.T.K. Kwok, I.D. Williams, A. Qin, B.Z. Tang, Chem. Sci. 8 (2017) 7593–7603.
[127] L. Zhu, B.J.C. Wong, Y. Li, H. Xin, B. Liu, J. Lei, Chem. Eur. J. 25 (2019) 4665–4669.
[128] A.-X. Ding, H.-J. Hao, Y.-G. Gao, Y.-D. Shi, Q. Tang, Z.-L. Lu, J. Mater. Chem. C 4 (2016) 5379–5389.
[129] N.-T. Chu, R.D. Chakravarthy, N.-C. Shih, Y.-H. Lin, Y.-C. Liu, J.-H. Lin, H.-C. Lin, RSC Adv. 8 (2018) 20922–20927.
[130] S. Dineshkumar, A. Raj, A. Srivastava, S. Mukherjee, S.S. Pasha, V. Kachwal, L. Fageria, R. Chowdhury, I.R. Laskar, ACS Appl. Mater. Interfaces 11 (2019) 31270–31282.
[131] L. Wang, Q. Xia, Z. Zhang, J. Qu, R. Liu, Mater. Sci. Eng. C 93 (2018) 399–406.
[132] J. Dong, Y. Pan, H. Wang, K. Yang, L. Liu, Z. Qiao, Y.D. Yuan, S.B. Peh, J. Zhang, L. Shi, H. Liang, Y. Han, X. Li, J. Jiang, B. Liu, D. Zhao, Angew. Chem. Int. Ed. 59 (2020) 10151–10159.
[133] Q.L. Guan, C. Han, F.Y. Bai, J. Liu, Y.H. Xing, Z. Shi, L.X. Sun, Sens. Actuators B Chem. 325 (2020) 128767.
[134] A. Casadevall, L.-A. Pirofski, Nature News 516 (2014) 165.
[135] R.M. Anderson, R.M. May, Nature 280 (1979) 361–367.
[136] N.D. Wolfe, C.P. Dunavan, J. Diamond, Nature 447 (2007) 279–283.
[137] S.K. Verma, R. Verma, K.S.S. Kumar, L. Banjare, A.B. Shaik, R.R. Bhandare, K.P. Rakesh, K.S. Rangappa, Eur. J. Med. Chem. 219 (2021) 113442.
[138] R. Verma, S.K. Verma, K.P. Rakesh, Y.R. Girish, M. Ashrafizadeh, K.S. Sharath Kumar, K.S. Rangappa, Eur. J. Med. Chem. 212 (2021) 113134.
[139] C. Zhou, W. Xu, P. Zhang, M. Jiang, Y. Chen, R.T.K. Kwok, M.M.S. Lee, G. Shan, R. Qi, X. Zhou, J.W.Y. Lam, S. Wang, B.Z. Tang, Adv. Funct. Mater. 29 (2019) 1805986.
[140] Q. Li, Y. Wu, H. Lu, X. Wu, S. Chen, N. Song, Y.-W. Yang, H. Gao, ACS. Appl. Mater. Interfaces 9 (2017) 10180–10189.
[141] V.G. Naik, S.D. Hiremath, A. Das, D. Banwari, R.U. Gawas, M. Biswas, M. Banerjee, A. Chatterjee, Mater. Chem. Front. 2 (2018) 2091–2097.
[142] J. Aw, F. Widjaja, Y. Ding, J. Mu, Y. Liang, B. Xing, ChemComm. 53 (2017) 3330–3333.
[143] F. Hu, G. Qi, D. Kenry, S. Mao, M. Zhou, W. Wu, B. Liu Wu, Angew. Chem. Int. Ed. 59 (2020) 9288.
[144] R.L. Siegel, K.D. Miller, A. Jemal, CA: Cancer J. Clin. 66 (2016) 7–30.
[145] H. Ananda, K.S. Sharath Kumar, M. Nishana, M. Hegde, M. Srivastava, R. Byregowda, B. Choudhary, S.C. Raghavan, K.S. Rangappa, Mol. Cell. Biochem. 426 (2017) 149–160.
[146] S. Jagadish, N. Rajeev, S.K. NaveenKumar, K.S. Sharath Kumar, M. Paul, M. Hegde, Basappa, M.P. Sadashiva, K.S. Rangappa, K.S. Girish, Mol. Cell. Biochem. 414 (2016) 137–151.
[147] M.W. Tibbitt, J.E. Dahlman, R. Langer, J. Am. Chem. Soc. 138 (2016) 704–717.
[148] Z. Wang, S. Chen, J.W.Y. Lam, W. Qin, R.T.K. Kwok, N. Xie, Q. Hu, B.Z. Tang, J. Am. Chem. Soc. 135 (2013) 8238–8245.
[149] M. Gao, B.Z. Tang, Coord. Chem. Rev. 402 (2020) 213076.
[150] L. Yang, W. Fang, Y. Ye, Z. Wang, Q. Hu, B.Z. Tang, Mater. Chem. Front. 3 (2019) 1335–1340.
[151] T. Li, S. Pan, H. Zhuang, S. Gao, H. Xu, ACS Appl. Biol. Mater. 3 (2020) 1283–1292.
[152] P. Zhang, T. Jiang, Y. Li, Z. Zhao, P. Gong, L. Cai, R.T.K. Kwok, J.W.Y. Lam, X. Gu, B.Z. Tang, Chem. Asian J. 14 (2019) 770–774.
[153] Z. Wang, C. Wang, Q. Gan, Y. Cao, H. Yuan, D. Hua, ACS Appl. Mater. Interfaces 11 (2019) (1861) 41853–41854.
[154] W. Fan, P. Huang, X. Chen, Chem. Soc. Rev. 45 (2016) 6488–6519.
[155] R. Zhang, Y. Duan, B. Liu, Nanoscale 11 (2019) 19241–19250.
[156] J. Zhang, C. Jiang, J.P. Figueiró Longo, R.B. Azevedo, H. Zhang, L.A. Muehlmann, Acta Pharm. Sin. B. 8 (2018) 137-146.
[157] S.G. Awuah, Y. You, RSC Adv. 2 (2012) 11169–11183.
[158] J. Du, X. Zheng, Y. Yong, J. Yu, X. Dong, C. Zhang, R. Zhou, B. Li, L. Yan, C. Chen, Z. Gu, Y. Zhao, Nanoscale 9 (2017) 8229–8239.
[159] F. Hu, S. Xu, B. Liu, Adv. Mater. 30 (2018) 1801350.
[160] J.M. Dąbrowski, Adv. Inorg. Chem. 70 (2017) 343–394.
[161] B. Yang, Y. Chen, J. Shi, Chem. Rev. 119 (2019) 4881–4985.
[162] W. Wu, D. Mao, S. Xu, S. Ji, F. Hu, D. Ding, D. Kong, B. Liu, Mater. Horiz. 4 (2017) 1110–1114.
[163] J. Chen, Z. Zou, Z. Ke, X. Zhang, J. Feng, Y. Jing, L. Peng, J. Yang, Y. Dai, D. Zou, New J. Chem. (2020).
[164] C. Parthiban, P.M.L. Vinod Kumar Reddy, D. Sen, M.S. S, N.D.P. Singh, ACS Appl. Nano Mater. 1 (2018) 6281.
[165] C. Parthiban, P.M.L. Vinod Kumar Reddy, D. Sen, N.D.P. Singh, ACS Appl. Nano Mater. 2 (2019) 3728–3734.
[166] S. Gao, X. Yan, G. Xie, M. Zhu, X. Ju, P.J. Stang, Y. Tian, Z. Niu, Proc. Natl. Acad. Sci. U.S.A. 116 (2019) 23437–23443.
[167] W. Wu, D. Mao, S. Xu, M. Panahandeh-Fard, Y. Duan, F. Hu, D. Kong, B. Liu, Adv. Funct. Mater. 29 (2019) 1901791.
[168] G. Jiang, C. Li, X. Liu, Q. Chen, X. Li, X. Gu, P. Zhang, Q. Lai, J. Wang, Adv. Optical Mater. 8 (2020) 2001119.
[169] S. Wang, P. Huang, X. Chen, Adv. Mater. 28 (2016) 7340–7364.
[170] R. Ngoune, A. Peters, D. von Elverfeldt, K. Winkler, G. Pütz, J. Control. Release 238 (2016) 58–70.
[171] Q. Chen, Y. Yang, X. Lin, W. Ma, G. Chen, W. Li, X. Wang, Z. Yu, ChemComm 54 (2018) 5369–5372.
[172] X. Tan, X. Pang, M. Lei, M. Ma, F. Guo, J. Wang, M. Yu, F. Tan, N. Li, Int. J. Pharm. 503 (2016) 220–228.
[173] S. Biswas, R. Menji, S. Barman, V. Vangala, A. Jana, N.D. Pradeep Singh, ChemComm. 54 (2018) 168–171.
[174] B. Guo, X. Cai, S. Wu, S.M.A. Fateminia, J. Liu, J. Liang, G. Feng, W. Wu, B. Liu, J. Mater. Chem. B 4 (2016) 4690–4695.
[175] G. Yu, M. Zhang, M.L. Saha, Z. Mao, J. Chen, Y. Yao, Z. Zhou, Y. Liu, C. Gao, F. Huang, J. Am. Chem. Soc. 139 (2017) 15940–15949.
[176] S.S. Liow, Q. Dou, D. Kai, Z. Li, S. Sugiarto, C.Y.Y. Yu, R.T.K. Kwok, X. Chen, Y.L. Wu, S.T. Ong, Small 13 (2017) 1603404.
[177] F. Hu, Y. Yuan, D. Mao, W. Wu, B. Liu, Biomaterials 144 (2017) 53–59.
[178] T.-T. Wang, Q.-C. Wei, Z.-T. Zhang, M.-T. Lin, J.-J. Chen, Y. Zhou, N.-N. Guo, X.-C. Zhong, W.-H. Xu, Z.-X. Liu, M. Han, J.-Q. Gao, Biomater. Sci. 8 (2020) 118–124.
[179] Z. Wang, C. Wang, Y. Fang, H. Yuan, Y. Quan, Y. Cheng, Polym. Chem. 9 (2018) 3205–3214.
[180] C. Zhang, L.-H. Liu, W.-X. Qiu, Y.-H. Zhang, W. Song, L. Zhang, S.-B. Wang, X.-Z. Zhang, Small 14 (2018) 1703321.
[181] Y. Qian, Y. Wang, F. Jia, Z. Wang, C. Yue, W. Zhang, Z. Hu, W. Wang, Biomaterials 188 (2019) 96–106.
[182] X. Xue, Y. Zhao, L. Dai, X. Zhang, X. Hao, C. Zhang, S. Huo, J. Liu, C. Liu, A. Kumar, W.-Q. Chen, G. Zou, X.-J. Liang, Adv. Mater. 26 (2014) 712–717.
[183] Q.-L. Li, D. Wang, Y. Cui, Z. Fan, L. Ren, D. Li, J. Yu, ACS Appl. Mater. Interfaces 10 (2018) 12155.
[184] M.A. Kay, Nat. Rev. Genet. 12 (2011) 316.
[185] Y. Yuan, C.-J. Zhang, B. Liu, Angew. Chem. Int. Ed. 54 (2015) 11419–11423.
[186] L. Wang, W. Wang, Z. Xie, J. Mater. Chem. B 2 (2014) 4398.
[187] N.S. Rejinolda, M. Muthunarayanana, V.V. Divyarania, P.R. Sreerekhaa, K.P. Chennazhia, S.V. Naira, H. Tamurab, R. Jayakumara, J. Colloid Interface Sci. 360 (2011) 39–51.
[188] G. Yu, D. Wu, Y. Li, Z. Zhang, L. Shao, J. Zhaou, Q. Hu, G. Tang, F. Huang, Chem. Sci. 7 (2016) 3017.
[189] J. Li, J. Wang, H. Li, N. Song, D. Wang, B.Z. Tang, Chem. Soc. Rev. 49 (2020) 1144–1172.
[190] X. Feng, B. Tong, J. Shi, C. Zhao, Z. Cai, Y. Dong, Mater. Chem. Front. 5 (2021) 1164–1184.
[191] H. Gao, X. Zhang, C. Chen, K. Li, D. Ding, Adv. Biosyst. 2 (2018) 1800074.
[192] F. Wu, X. Wu, Z. Duan, Y. Huang, X. Lou, F. Xia, Small 15 (2019) 1804839.
[193] B. Gu, K.-T. Yong, B. Liu, Small Methods 2 (2018) 1700392.